

Study on High-Frequency Permeability
in Ferrite Ceramics
and Ferrite Composite Materials

Tatsuya Nakamura

Contents

Abstract	1
Acknowledgments	4
1. Introduction	5
2. Crystal structure and magnetic properties of spinel ferrite	
2.1 Crystal structure	8
2.2 Magnetic properties	9
3. Synthesis technique	
3.1 Solid state reaction	14
3.2 Hydrothermal precipitation	17
4. Frequency dispersion of complex permeability	20
4.1 Spin rotational permeability	22
4.2 Domain wall motion contribution	24
4.3 Inverse cole-cole plot technique	26

5. Permeability dispersion of Ni-Zn ferrite composite materials	29
5.1 Complex permeability spectra	31
5.2 Magnetic circuit model	33
5.3 Extended Snoek's law	36
5.4 Temperature variation of permeability spectra	39
6. Complex permeability in low-temperature sintered Ni-Zn-Cu ferrite	43
6.1 Sintering ability and permeability	46
6.2 Permeability variation	47
7. Electromagnetic properties and power loss in Mn-Zn ferrite ceramics	50
7.1 Microstructure and electromagnetic properties	52
7.2 Power loss	56
8. Concluding remarks	58
References	60

Abstract

The complex permeability spectra of Ni-Zn sintered ferrite and the ferrite composite materials were studied. The complex permeability spectra in the ferrite composite materials depend not on the ferrite particle size but on the volume loading of the ferrite particles. The real part of the complex permeability in low-frequency region decreases as the ferrite volume loading is reduced. The shoulder frequency of the real permeability shifts toward higher frequency with a decrease in the ferrite volume loading, hence the real permeability in high-frequency region does not always decrease with a decrease in the ferrite volume loading : it becomes larger in the ferrite composite materials than in the sintered ferrite. The imaginary part of the complex permeability in low-frequency region also decreases as the ferrite volume loading is reduced. The peak frequency of the imaginary part also shifts toward higher frequency with a decrease in the ferrite volume loading. These experimental facts cannot be expected using the semi-empirical logarithmic law.

In order to establish the physical picture on the complex permeability variation, we separate the complex permeability spectra into two contributions : the spin rotational and the domain wall motion components, using the numerical fitting called the inverse cole-cole technique. First, in the sintered ferrite, the domain wall component, the frequency dependence of which is resonance-like, contributes the complex permeability only below 100MHz region. The spin rotational permeability, the frequency dependence of which is relaxation-type, remains even at higher frequency such as 1GHz region. Next, from the experimental results on the ferrite composite materials, the spin permeability

strongly depends on the ferrite loading : the static spin susceptibility decreases and the spin resonance frequency shifts toward higher frequency when the ferrite loading is reduced. The domain wall component depends not only on the ferrite loading and but also on the ferrite grain size : the static susceptibility of the domain wall motion decreases and the domain wall resonance frequency shifts toward higher frequency, as the ferrite loading is decreased. While, in low frequency region, the permeability of the ferrite composite materials is lower than that of the sintered ferrite, the permeability of the ferrite composite materials is greater than that of the sintered ferrite at high frequency such as 100MHz region.

These features can be explained by the magnetic circuit model calculation. In the model calculation, the parameters, such as static susceptibilities and resonance frequencies, are transformed using the gap parameter, which is a simple index for the averaged structure of the composite materials. In other word, we can estimate the complex permeability spectra for the ferrite composite materials using the magnetic circuit model combined with the spin rotation and the domain wall motion formulations. The magnetic circuit model provides changes in the magnetic connection with the ferrite loading. The introduction of the magnetic inert component causes not only the magnetic dilution but also a cut-off of the magnetic circuit in the materials. Thus, the permeability becomes lower than that expected from the semi-empirical logarithmic law. The feature is attributed to the demagnetizing field generated by the magnetic poles on the interface of the ferrite particle. Simultaneously, the addition of the demagnetizing field on the magnetocrystalline anisotropy field leads to a shift of the resonance frequency toward higher frequency.

Additionally, using this model calculation, we obtain the extended Snoek's law for the composite materials, and we can explain the temperature variation of the complex permeability in the ferrite composite materials. Furthermore, this magnetic circuit model can be applied to other phenomena such as the complex permeability variation in low-

temperature sintered Ni-Zn-Cu ferrite ceramics and the electromagnetic properties and power losses in Mn-Zn ferrite sintered ceramics. This model calculation is thought to be a useful tool for the development in many high-frequency electromagnetic devices through the evaluation of the complex permeability in the materials.

Acknowledgments

I would like to thank the special thanks to Professor I. Ishikawa of Hiroshima University for his kind invitation and appropriate facilities during this work.

I want to express my appreciation to Professor K. Yoshikawa of Hiroshima University for his continuous advice and encouragement during this work and for usually giving the nature of it.

I would like to acknowledge to Dr. Y. Teraoka (Faculty of School Education, Hiroshima University) and Dr. K. Matsukawa (Research & Development Promotion Research Laboratory, NEC Corporation) for their kind discussion and helpful suggestion in this work.

I want to thank to Mr. K. Hoshino (President of Hiroshima Tokai Sangyo Corporation), Dr. T. Yamaguchi (Director of R&D Division, Tokai Sangyo Corporation) and Mr. F. Yamamoto (Sales Manager of R&D Division, Tokai Sangyo Corporation) for giving me a chance to study this work.

Finally, I want to thank to my wife for her continual support and encouragement in this work.

Acknowledgments

The author owes special thanks to Professor T. Takabatake of Hiroshima University for his kind discussion and appropriate direction during this work.

I want to express my appreciation to Professor K. Nishikawa of Hiroshima University for his continuous advice and encouragement during this work and for critically reading the manuscript.

I should wish to acknowledge to Dr. T. Tsutaoka (Faculty of School Education, Hiroshima University) and Dr. K. Hatakeyama (Resource & Environment Protection Research Laboratories, NEC Corporation) for their kind discussion and helpful suggestion in this work.

I wish to thank to Mr. N. Horiishi (Executive Director, Toda Kogyo Corporation), Mr. Y. Yamaguchi (Director of R&D division, Toda Kogyo Corporation) and Mr. S. Yamamoto (Section manager of R&D division, Toda Kogyo Corporation) for giving me a chance to study this work.

Finally, I wish to thank to my wife for her continuous supports and understanding to this work.

Chapter 1

Introduction

Ferrite magnets have been used extensively in many electronic devices, because they have high permeability and electric resistivity in high frequency region, mechanical hardness and environmental stability. The initial permeability is an important factor in the application to some electronic devices. In particular, the frequency dispersion of the complex permeability determines high-frequency characteristics of these devices. In polycrystalline ferrites, the permittivity is generally attributed to the space charges in the grain boundary, and the permeability is related to the magnetizing mechanisms, i.e., the spin rotation and the domain wall motion. There have been many studies on the permittivity and permeability of polycrystalline ferrites[1-5].

Ferrite composite materials, prepared by mixing ferrite particles with an appropriate amount of non-magnetic resin, have also been studied in recent years from the view point of their preparation and characterization. The permeability and their frequency dispersion can be controlled by the fabrication process of the ferrite composite materials, such as the volume loading of ferrite particle, the particle size of ferrite and so on. The permeability in ferrite composite materials has been estimated using the semi-empirical logarithmic law[6]. However, this law is inadequate to explain the frequency dispersion, which is important for the practical device designs, since it can describe only the absolute value of the permeability or permittivity. In addition, the values of the permeability in the composite materials are smaller than those expected from the logarithmic law.

Recently, C.A. Grimes and D.M. Grimes calculated the effective permeability and permittivity spectra of the composite and/or polycrystalline materials using the Clausius-Mossotti equation [7-9]. They treated a regular or random array of identical spherical particles and calculated the inter-particle interactions with the multi-polar field expansion. This effective medium theory is thought to be a useful method for the estimation of the permeability spectra. However, some parameters applied in their calculation model are complicated and it is difficult to make relations between their parameters and the practical material characters such as volume loading and characters of dispersed particles.

W.T. Doyle and I.S. Jacobs considered the permittivity of the metal-insulator composites, in which the conducting particles are dispersed in the insulating matrix[10,11]. They indicated that a large enhancement of the permittivity occurred at high volume loading of the conducting particle and that the permittivity became higher than that predicted from the Clausius-Mossotti approximation, since their metal insulator composite model was started from that with low volume loading. This dielectric anomaly is attributed to the percolation problem and the formation of the conducting path with the contact of the particles. On the other hand, we consider that the ferrite composite material is a kinds of the sintered ferrite which has many magnetic gaps. The magnetic gaps, introduced into the sintered ferrite, play an important role in reducing the permeability below that expected from the empirical logarithmic law.

M.T. Johnson and E.C. Visser proposed a simple model for the magnetic gaps in polycrystalline ferrite [12]. They considered that the ferrite grains are surrounded by non-magnetic grain boundary layers with large magnetic resistivity. They called this model the 'coherent model'. From the analysis of the static permeability using this model, they estimated the thickness of the non-magnetic grain boundary layer as approximately 1nm, and that this thickness remains constant when the ferrite grain size changes.

In this thesis, a model is proposed, which provides a clear statement for the

physical meaning, for the frequency dispersion of the complex permeability in the ferrite composite materials. This model is based on the magnetic circuit theory combined with the formulation of the domain wall motion and the spin rotational permeability.

The remaining part of this thesis is subdivided into seven chapters. In chapter 2, we first review the magnetic properties, especially magnetic structure and the magnetic anisotropy, of spinel ferrite in view of the crystal structure and the electronic state of the transition metal ions. In chapter 3, various preparation techniques for polycrystalline ferrite are explained. The detail of the co-precipitation with oxalate precursor is presented. In chapter 4, two contributions to the complex permeability, the spin rotational and the domain wall motion components, are described. In addition, their separation technique, called the inverse cole-cole plot, is shown. These formulations are the basis of our numerical analysis on the frequency dispersion of the complex permeability. In chapter 5, the experimental results on the frequency dispersion of the complex permeability are shown. They are separated into the spin rotational and the domain wall motion components and analyzed numerically using the magnetic circuit model. From the magnetic circuit model calculation, the extended Snoek's limit for the ferrite composite materials is proposed. Furthermore, we discuss the temperature variation of the complex permeability from the view point of our magnetic circuit model. In chapter 6, we present the experimental results about the low-temperature sintered ferrite. We clarify the relationship between the complex permeability and the microstructure of the sintered ferrite ceramics, according to the basic idea of our magnetic circuit model. In chapter 7, the experimental results on the electromagnetic properties of Mn-Zn ferrite sintered ceramics, which are applied to power devices, are also analyzed using an extended model called the non-magnetic insulating grain boundary layer model. Finally, in chapter 8, the concluding remarks are given.

Chapter 2

Crystal structure and magnetic properties of spinel ferrite

2.1 Crystal structure

The spinel structure, named for the mineral spinel $MgAl_2O_4$, consists of face-centered cubic array of oxygen ions with large ionic radius (0.13nm), in the interstitial positions of which the transition metal ions with small ionic radius (0.06 to 0.08nm) are located. Two types of interstices are available, one formed by four oxygen ions at the vertices of a tetrahedron and the other by six oxygen ions at the vertices of an octahedron (see Fig. 2-1) : these interstices are commonly called the tetrahedral or A sites and the octahedral or B sites, respectively. Each unit cell contains eight formula unit (32 oxygen ions), in which 64 tetrahedral and 32 octahedral interstices are present, but only 8 tetrahedral and 16 octahedral sites are occupied by metal ions[1].

In reality, the oxygen positions are variable and deviate from the ideal positions, while the positions of the metal ions are fixed by the symmetry of the structure. The tetrahedral sites are too small to contain a metal ion. Therefore, tetrahedral interstices are expanded by an equal amount of outward displacement of the four oxygen ions, so that the surrounding of metal ions retains cubic symmetry. As a consequence, the oxygen surrounding of the octahedral sites no longer has cubic symmetry. This deformation of the oxygen array is specified by the u-parameter, which is defined in Fig. 2-2. The value $u=3/8=0.375$ corresponds to perfect close-packing oxygen ions, and the observed values

of u range from 0.38 to 0.39.

If the tetrahedral sites are occupied by divalent cations and the octahedral sites by trivalent cations, the structure is called the normal spinel structure. If the tetrahedral sites are occupied by trivalent cations and the octahedral sites by a random arrangement of divalent and trivalent cations, the structure is called the inverse spinel structure. In general spinel oxides, intermediate arrangements are also possible, and the cation distribution depends on some conditions, namely, the equilibrium factor being attributed to the Madelung energy which is related to the ionic radius and the valence state of the cation, and the non-equilibrium factor which is reflected in sample preparation route and thermal history. The following trends are usually known ; Zn^{2+} and Cd^{2+} have a strong preference for the tetrahedral site, and the other cations such as Fe^{2+} , Co^{2+} and Ni^{2+} have the octahedral site preference.

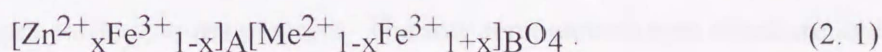
2.2 Magnetic properties

First, we consider the exchange interaction between the spins, localized at the cations, in the spinel ferrite. According to the crystal structure, oxygen ions are located between the cations, so that the interatomic distance between the cations is expanded. Therefore, the direct exchange interaction between the cations is very weak, if it exists, and the superexchange interaction, which acts through oxygen ions ($Me-O-Me'$), is important. In general, the superexchange interaction depends on the distances of $Me-O$ and $Me'-O$ and on the $Me-O-Me'$ bonding angle. It is known that the magnitude of the interaction decreases very rapidly with an increase of the bonding distance and that an bonding angle of π gives rise to the greatest exchange interaction[2,3,4].

In spinel ferrite, the superexchange interaction is negative and antiferromagnetic coupling is dominant[5,6]. The antiferromagnetic exchange interactions, which are thought to exist in the spinel ferrite, are shown in Fig. 2-3. The bonding angles of $A-O-A$ and $B-O-B$ interaction paths are fairly smaller than π and about $(\pi/2)$, and they

consequently provide weak antiferromagnetic couplings. The A-O-B interaction is strongly antiferromagnetic, since it has the bonding angle about $(3\pi/4)$. Therefore, the spins are ferromagnetically aligned within the B-sublattice, and the spin at A-sublattice is anti-parallel to those at B-sublattice. It yields ferrimagnetic spin structure, and the resultant magnetization is thus the difference between the sublattice magnetization of the octahedral B-site and that of the tetrahedral A-site. However, in the case that non-magnetic cations such as Zn^{2+} and Cd^{2+} are located at A-sublattice, the spins are antiferromagnetically aligned within the B-sublattice, which results in the sublattice separation to B' and B''-sublattices. Thus, Zn-ferrite and Cd-ferrite are antiferromagnetic materials with remarkably low Neel temperature.

Apart from the simple ferrites, an interesting aspect is exhibited in the mixed ferrite containing Zn^{2+} with a strong preference for tetrahedral coordination and Me^{2+} with a strong octahedral preference, in which the cation distribution is written as



In the case of small x value, the A-O-B exchange interaction is strong enough to lead to a collinear spin structure that the spins are ferromagnetically aligned within the B-sublattice and the spin at A-sublattice is anti-parallel to those at B-sublattice. The net magnetization M is given by

$$M = (1-x) m(Me^{2+}) + 2x m(Fe^{3+}) \quad (2. 2)$$

where $m(Me^{2+})$ and $m(Fe^{3+})$ are the ionic magnetization of Me^{2+} and Fe^{3+} , respectively. Therefore, the net magnetization increases with an increase in x, that is, with an increase of Zn^{2+} content. On the other hand, when x approaches to unity, the A-O-B exchange path is diluted, so that the B-O-B antiferromagnetic interaction leads to another collinear spin structure that the spins are antiferromagnetically aligned within the B-sublattice. It results in the net magnetization of

$$M = (1-x) m(Fe^{3+}) \quad (2. 3)$$

It implies that the net magnetization decreases with an increase in x. The tendency of the

magnetization variation is reversed to that in the region of small x . Combining equation (2. 3) with (2. 2), the net magnetization has a maximum at an intermediate value of x . In the intermediate region, the spin structure is transformed from a collinear one to another, and there exists a strong competition between the A-O-B exchange interaction and that of B-O-B. This exchange competition provides non-collinear spin structure. In a simple description, the magnetization at B'-sublattice makes an average angle (2θ) with that at B''-sublattice, as shown in Fig. 2-4. It is called the Yafet-Kittel configuration[7], and the angle increases gradually with an increase of x . Thus, the net magnetization is,

$$M = [(1-x)m(\text{Me}^{2+})+(1+x)m(\text{Fe}^{3+})] \cos\theta - (1-x)m(\text{Fe}^{3+}). \quad (2. 4)$$

In the following discussions, the distribution of the canting angle is important. The longitudinal spin component shows a normal order-disorder transition and the transverse components are randomly frozen. They produce the situation in which the spin-glass phase of the transverse component coexists with the ferromagnetic ordering of the longitudinal component at low temperature. The low-temperature spin structure and its re-entrant spin-glass transition have been recently investigated using the neutron diffraction and the Moessbauer spectroscopic technique[8,9,10].

Figure 2-5 shows the experimental results of the magnetization variation at room temperature in Ni-Zn mixed spinel ferrites. They were synthesized through the thermal decomposition of co-precipitated Fe-Ni-Zn oxalate precursors, detailed technique of which is described in the next chapter. It is noted that the tendency contains an effect of the variation in the Curie temperature (the Curie temperature decreases with an increase in the Zn^{2+} content). As expected from the above discussion, the magnetization increases with an increase in the Zn^{2+} content, takes a maximum of 80emu/g at around $x=0.4$, then decreases as x becomes larger than 0.5.

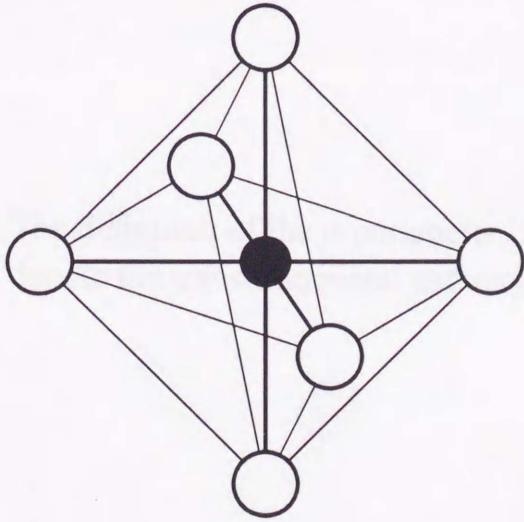
Next, we consider the magnetocrystalline anisotropy in the spinel ferrite. It is known that the magnetocrystalline anisotropy is a single-ion anisotropy, which is attributed to the interaction between spin and orbital angular momentums[11]. In order

to consider the orbital angular momentum, we need the information about the 3d electronic states. The 3d electronic states of the transition metal ions, which are degenerated in free ion state, are split by the crystal field originated from the coordinated oxygen ions. The splitting of the energy levels depends on the coordinating configuration of the oxygen ions. The oxygen coordination with cubic symmetry causes a splitting of the five-degenerated levels into a double-degenerated one ($d_{3z^2-r^2}$, $d_{x^2-y^2}$) and a triple-degenerated one (d_{xy} , d_{yz} , d_{zx}). The lowering in the coordination symmetry causes further splitting of the levels, which is shown in Fig. 2-6, namely, the splitting of the triple-degenerate one (d_{xy} , d_{yz} , d_{zx}) into a double one (d_{yz} , d_{zx}) and a single one (d_{xy}) under trigonal symmetry, that of the double-degenerated one ($d_{3z^2-r^2}$, $d_{x^2-y^2}$) into two single ones under tetragonal symmetry, and finally that of the double-degenerated one (d_{yz} , d_{zx}) into two single ones under orthorhombic symmetry. It is noted that the order of the energy levels in octahedral site is reversed to that in tetrahedral site, which is attributed to the geometry of the 3d wave functions. According to Hund's rule, the electrons occupy these energy levels. We note that, in oxides, the intra-atomic Coulomb interaction is usually larger than the crystal field energy. Thus, the electron configuration is in a high spin state. The low spin state of the electron configuration is stable, if the intra-atomic Coulomb interaction is smaller than the crystal field energy. In the case that the number of the electrons located at the degenerated states is less than the degenerated degree (for example, a cation with d^1 , d^2 , d^4 , d^6 , d^7 or d^9 electronic state is located in the octahedral site with cubic symmetry), it is possible that the spontaneous distortion of the oxygen coordination into lower symmetry leads to a splitting of the degenerated levels in order to reduce the total energy. It is called the Jahn-Teller effect[12], which can be observed in $\text{Cu}^{2+}(d^9)$ or $\text{Mn}^{3+}(d^4)$ -containing spinels.

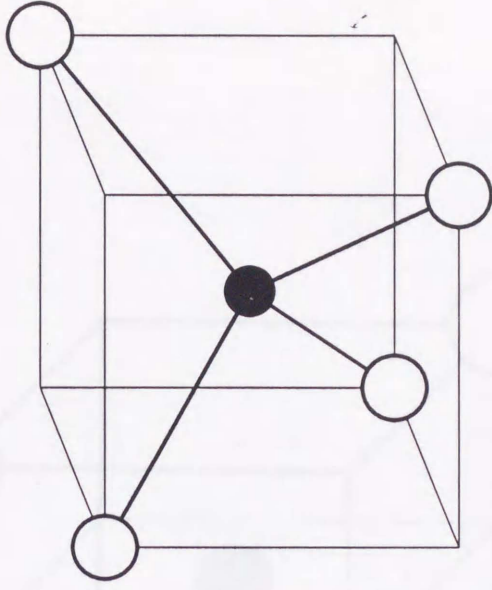
It is known that the electron configuration in the non-degenerated states has no orbital angular momentum, which is the quenching of the orbital angular momentum[11]. This is an important fact for the consideration on the magnetocrystalline anisotropy. All

the transition metal ions preferentially located in the tetrahedral site have filled or half-filled 3d band, so that they have little contribution to the magnetocrystalline anisotropy. Consequently, we consider mainly the transition metal ions located in the octahedral site. It is expected that the transition metal ion with the electronic configuration of d^1 , d^2 , d^4 , d^6 , d^7 or d^9 has non-quenched angular momentum in the cubic-symmetric octahedral site and gives a great contribution to the magnetocrystalline anisotropy. In the real spinel lattice, the octahedral coordination is distorted trigonally, which has been already shown in Fig. 2-2. For example, d^6 and d^7 have a ground state with singlet and doublet, respectively, in the crystal field with the trigonal symmetry[11]. Therefore, a strong magnetocrystalline anisotropy can be observed only for $d^7(\text{Co}^{2+})$. It has been found that Co^{2+} has a large magnetocrystalline anisotropy with the easy axis along (100)-direction, and that the other transition metal ions have small magnetocrystalline anisotropy, the easy axis of which is along (111)-direction. The large magnetocrystalline anisotropy of Co^{2+} has been applied to the coercivity enhancement of iron oxide acicular particles, which are utilized in the magnetic recording devices[13].





(a)



(b)

Figure 2-1 : Two type of the interstices in the spinel structure. (a) octahedral coordination and (b) tetrahedral coordination. The solid and open circles denote the transition metal and oxygen ions, respectively.

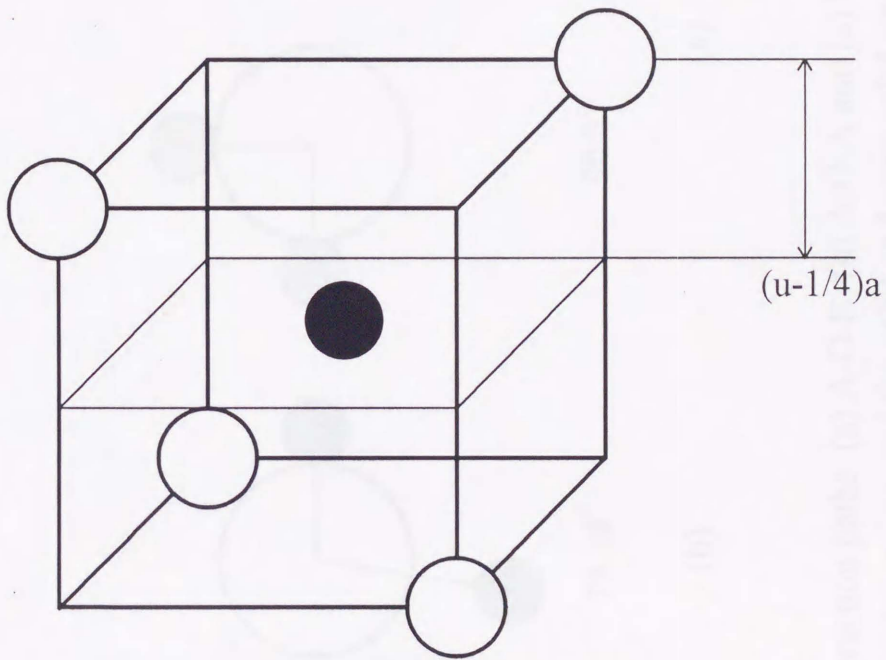


Figure 2-2 : The definition of the u-parameter. The solid and open circles denote the transition metal and oxygen ions, respectively.

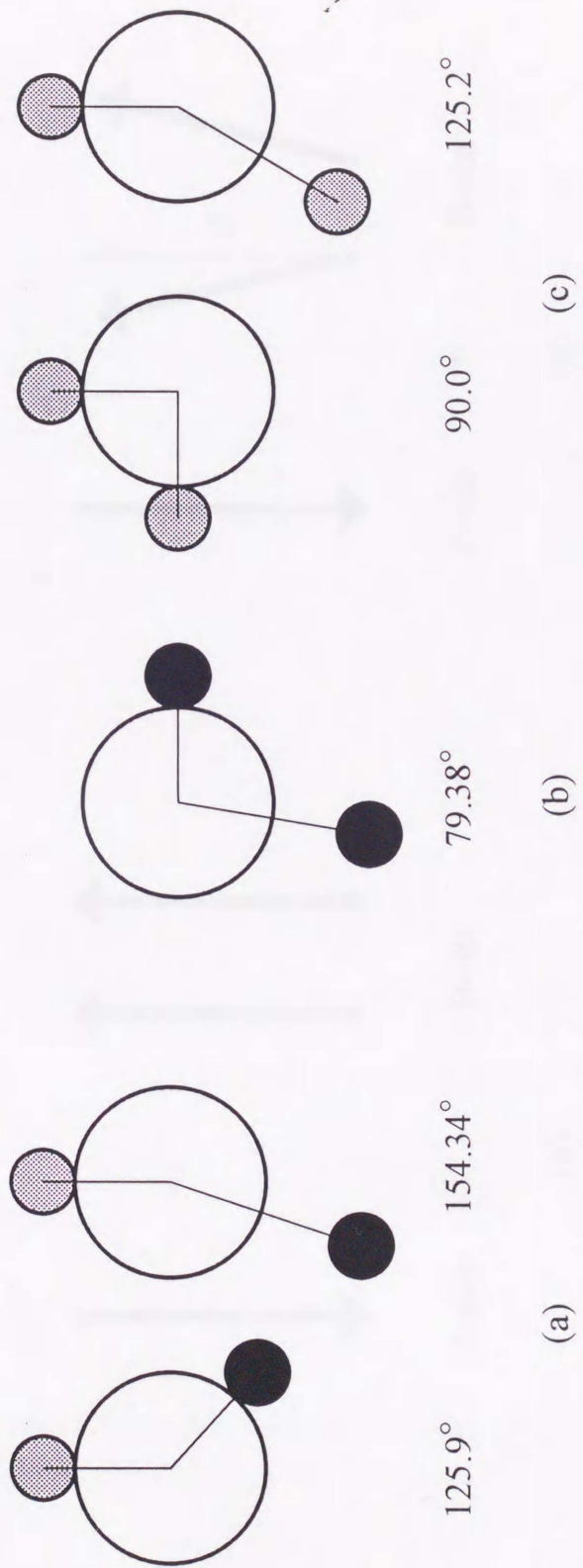


Figure 2-3 : The superexchange interaction paths. (a) A-O-B, (b) A-O-A and (c) B-O-B. The open circle denotes oxygen ion, and the solid and semi-solid circles denote the transition metal ions at A (tetrahedral) and B (octahedral) sites, respectively.

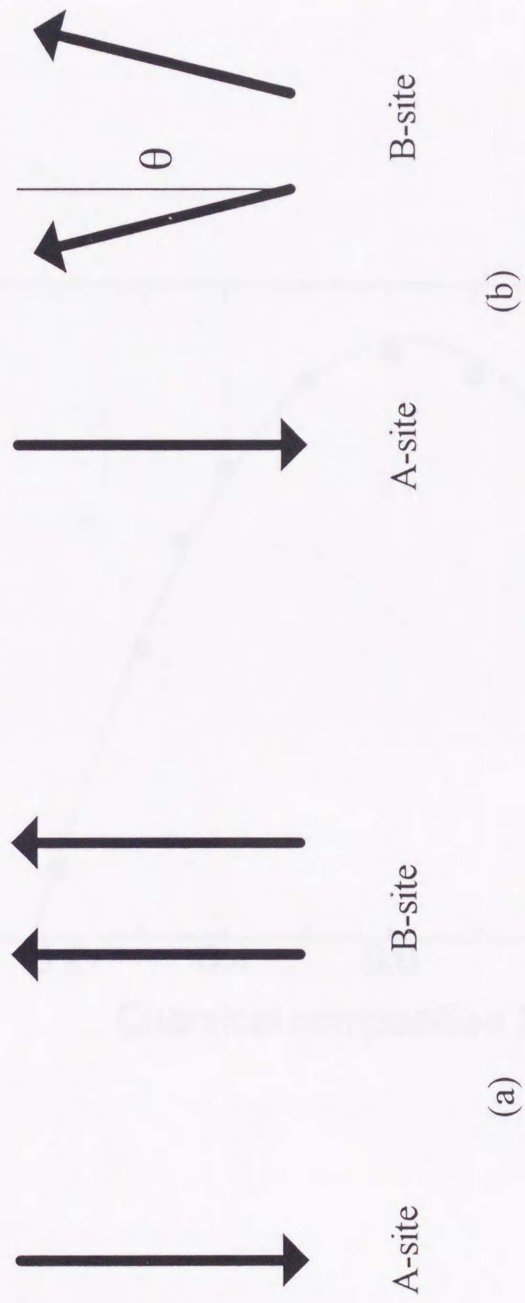


Figure 2-4 : The spin structure in spinel ferrite. (a) collinear Neel model and (b) Yafet-Kittel canted model. The canting angle of the B-site spins is represented by θ .

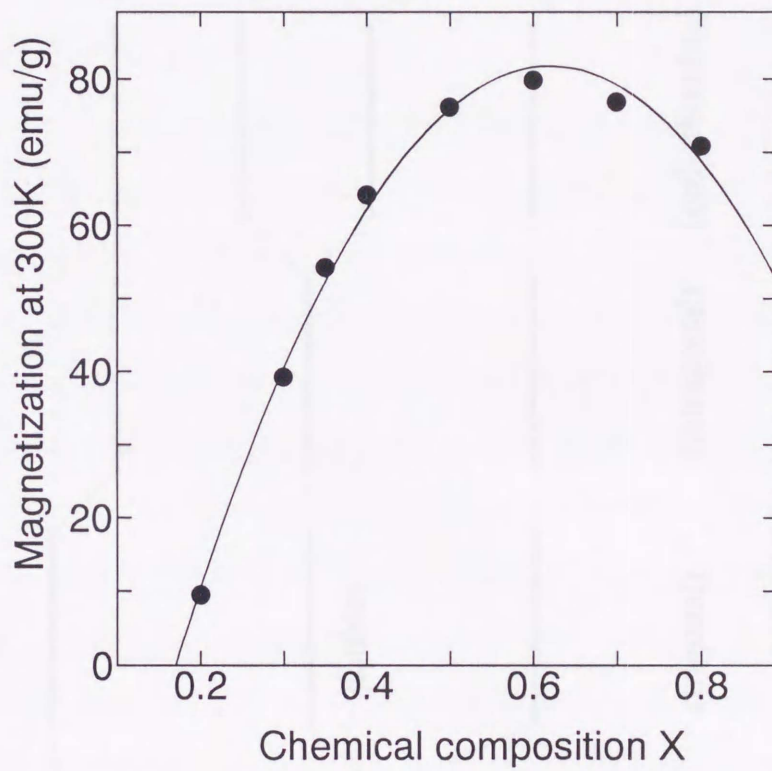


Figure 2-5 : The magnetization variation with the composition in Ni-Zn ferrite $Ni_{1-X}Zn_XFe_2O_4$.

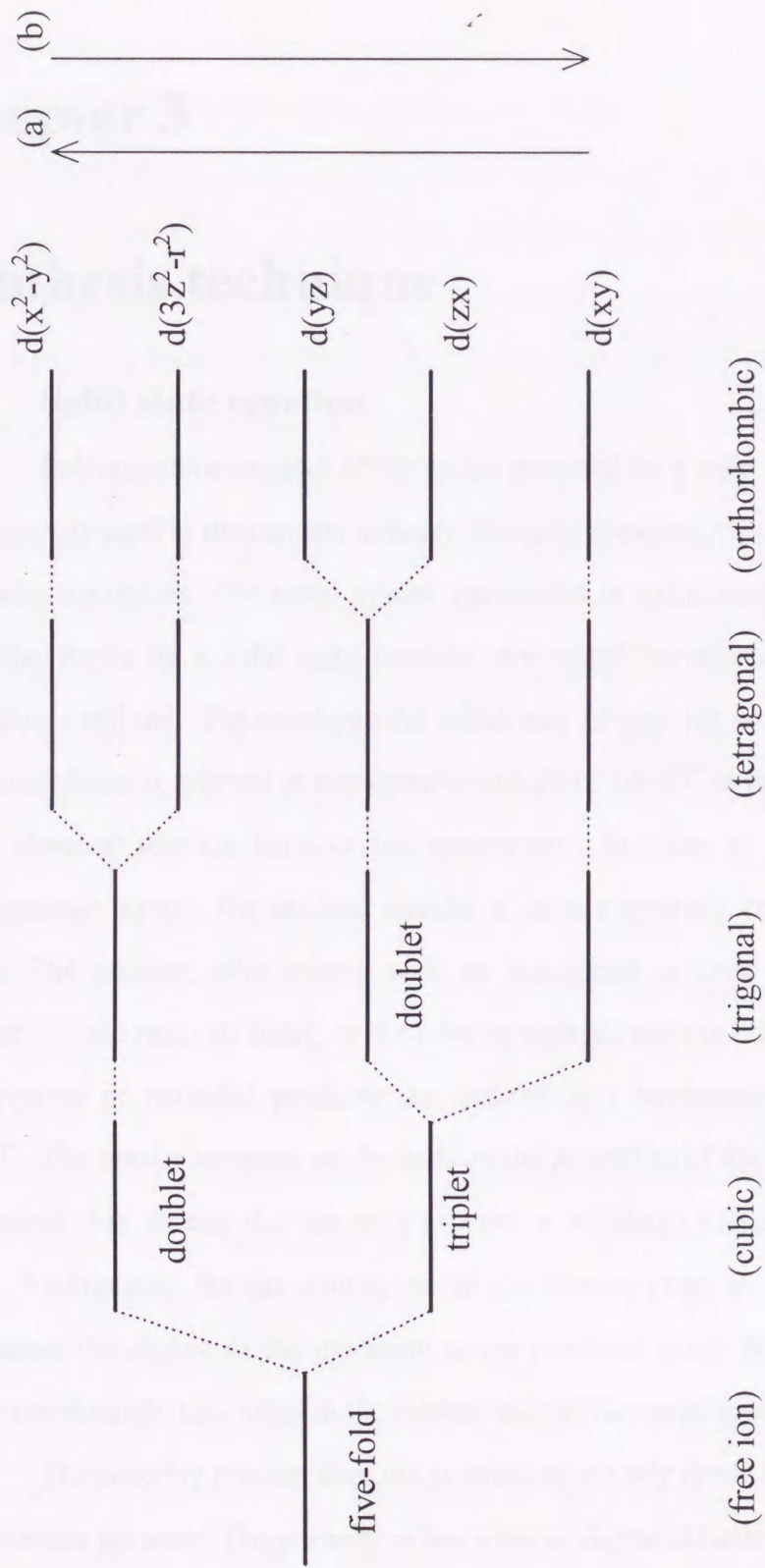


Figure 2-6 : Energy diagram for 3d electronic states in octahedral coordinating transition metal ions (a) and in tetrahedral coordinating transition metal ions (b).

Chapter 3

Synthesis technique

3.1 Solid state reaction

Polycrystalline samples of ferrite are prepared by a solid state sintering process as commonly used in the ceramic industry. Roughly speaking, this process comprises the following operations. The metal oxides, carbonates or other compounds, which are to form the ferrite by a solid state reaction, are mixed homogeneously and wet-milled usually in a ball mill. The dried powder which may or may not have been pressed into a particular shape, is calcined at a temperature of about 1000°C in order to bring about the initial chemical reaction between the constituents. In order to produce a chemically homogeneous sample, the calcined powder is again intensively crushed, wet-milled and mixed. The powder, after mixing with an appropriate amount of organic binder, is pressed into the required shape, or extruded as a plastic mass in the form of tubes or rods. The pressed or extruded products are sintered at a temperature between 1000 and 1400°C . The precise temperature depends on the properties of the ferrite that are wanted. It is noted that, during this sintering process, a shrinkage of approximately 20% can occur. Additionally, the gas atmosphere in the furnace plays an essential role, since it determines the degree of the oxidation in the products which dominates the magnetic properties through the control in the valence state of the metal ions.

The sintering process does not produce an entirely dense material, but a product has a certain porosity. The porosity of the sintered ferrite ceramic is the relative volume of the pores, and it is estimated from the comparison of the X-ray density with the

apparent density of the ferrite. The sintering temperature necessary to obtain a dense product depends on the chemical composition of the ferrite. It is related to the melting point of the ferrite. It is well known that the addition of Zn^{2+} or Cu^{2+} lowers the sintering temperature and that Ni^{2+} does not diffuse easily into ferrite. The temperature, at which good sintering takes place, also depends strongly on the grain size and grain shape of the starting material. A very fine-grained powder gives dense products at a lower sintering temperature. For this reason, long-time milling of the compounds or the calcined ferrite is often carried out.

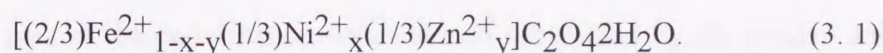
It is thought that low-temperature synthesis is suitable for the production of fine-grained ferrite powder, since the grain growth is thermally promoted. Moreover, at low temperature, the cation diffusion is also limited. Therefore, homogeneous mixing of the constituents is a critical problem for low-temperature synthesis of ferrite phase. In the wet-milling of the metal oxides, carbonates or other compounds in a ball mill, inhomogeneity in their particle scale cannot be avoided. In order to improve the homogeneity of the mixture, there are many techniques, such as, chemical coprecipitation, spray-drying[1,2] and sol-gel preparation[3,4], etc. In the spray-drying method, the mixed aqueous solution of the constituents is sprayed in a fine droplet form. They are carried with an inert gas flow, then put into the dryer. The aqueous droplet particles are dried immediately, and transformed to the mixed salt particles of the constituents. In the sol-gel technique, a polymer with gel formation ability (for example, poly-ethylene glycol) and a chelating agent (citric acid, tartaric acid or malonic acid) are first added to the mixed aqueous solution of the constituents, and then the solution is heated and kept at about the boiling temperature. The gel condensation proceeds with the dehydration, and thus the clusters of the mixed metal chelate compound are dispersed and fixed in the polymer matrix, which is identified as being amorphous by the powder X-ray diffraction analysis. Additionally, the incomplete dehydration provides homogeneous solution with appropriate viscosity, which is suitable for the preparation of

the films through the spin-coating technique. In these two methods, the atomic level homogeneity in the aqueous solution remains in the mixed precursors, and the homogeneous mixing of the constituents can easily be obtained.

In the chemical co-precipitation method, the chemical composition in the co-precipitated phase is different from that in the mixed aqueous solution, because of the differences in the solubility of the constituent elements. This is one of the technical problems in the co-precipitation method, which cannot be presented in the spray-drying and the sol-gel methods. In order to suppress the compositional deviation, we need to select the precipitating reagent, the pH value of the solution, and the solution temperature. Generally, hydroxides have been used as the precipitated phase, but they are too fine colloidal particles to be separated from the mother solution by filtration.

We have utilized oxalate as the precipitating reagent, the experimental results of which are described below. It was found that Ni^{2+} , Zn^{2+} and Fe^{2+} are precipitated as β -oxalate dihydrate ($\beta\text{-MeC}_2\text{O}_4\text{2H}_2\text{O}$), while Mn^{2+} precipitates in α -form. It is possible to prepare homogeneous co-precipitation of Ni^{2+} - Zn^{2+} - Fe^{2+} system using oxalate. First, the solubility of the individual oxalate was investigated at various pH values and a fixed temperature of 50°C , where the concentration of the metal ions was selected in the range from 0.2 to 0.6M and the molar ratio of oxalic acid to metal salt was fixed at 1.5. The solubility of the individual component versus the pH value of the aqueous suspension is shown in Fig. 3-1. The solubility of Fe^{2+} -oxalate increases with an increase in the pH value and remarkably increases at $\text{pH}>6.0$. It takes a minimum at around $\text{pH}=2.0$. The solubility of Zn^{2+} -oxalate has the same trend as that of Fe^{2+} -oxalate. For Ni^{2+} -oxalate, a similar behavior is observed and the solubility anomalously increases at $\text{pH}>5.0$. All of them have the minimum solubility at around $\text{pH}=2.0$, the value of which is 0.4%, 2.0% and 0.3% for Fe^{2+} -oxalate, Ni^{2+} -oxalate and Zn^{2+} -oxalate, respectively. Next, at the co-precipitation pH value of 2.0, the chemical composition deviation of the co-precipitated oxalate from the composition in the starting aqueous solution was

investigated, the results of which are shown in Table 3-1. We adjusted the composition of the starting aqueous solution to that of the stoichiometric ferrite, so we can write the oxalate composition as follow,



The chemical composition in the oxalate precursor coincides well with that in the starting aqueous solution. We have examined the compositional homogeneity within the co-precipitated oxalate particle by the electron microprobe analysis. The compositional inhomogeneity such as the clustering of the individual element cannot be observed within the oxalate particle, the scanning electron microphotograph of which is shown in Fig. 3-2. The particles have orthorhombic shape and the average dimension of approximately $4\mu\text{m}$, so that they are easily separated from the mother solution. Thus, the oxalate is thought to be a solid solution of the corresponding oxalates and a good candidate for the homogeneous precursor of ferrite.

3. 2 Hydrothermal precipitation

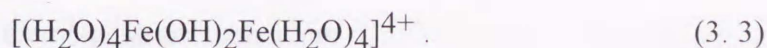
In hydrothermal precipitation, the crystal structure of the spinel ferrite can be established as well as the chemical composition. That is, the as-precipitated particles are single or polycrystalline spinel ferrites. Therefore, the homogeneous fine particles of ferrite can be obtained without after-annealing. They are thought to be precursors more suitable for the synthesis of the polycrystalline ferrite ceramics.

Hydrothermal precipitation is based on the hydrolysis of metal ions and the polymerization of the hydrolyzed low-molecular-weight complexes[5]. We first describe the hydrolysis process of ferric ions. Ferric ions are octahedrally coordinated with six water molecules (aqua-complex) and stabilized by the configuration energy.

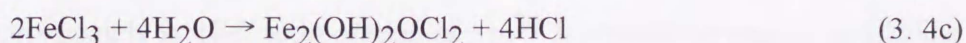
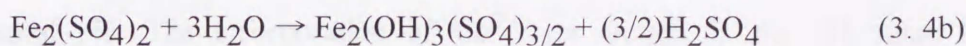
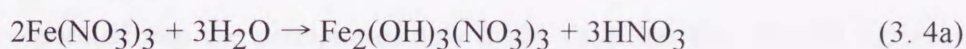


A part of the coordination water is replaced by the counter anion such as Cl^- and SO_4^{2-} . As the pH value or the temperature of the aqueous solution is raised, the monomers are

antiferromagnetically coupled through bidentate hydroxy-bridging and form the edge-sharing octahedral dimers :



Here, a part of the coordination water is also substituted by the present anions, so that their structures depend on the kind of the present counter anions. On further rising in the pH value, the dimers are connected by edge-sharing to form the polynuclear complexes[6] ;



where the coordination waters are omitted. Figure 3-3 shows the structure of these polynuclear complexes. In the case that the counter anion is SO_4^{2-} or NO_3^- , the edge-sharing octahedral dimers are antiferromagnetically bound together by monodentate hydroxy-bridging to give a zigzag chain of the polynuclear cation. In the case of Cl^- , the edge-sharing octahedral dimers are antiferromagnetically bound together by oxo-bridging to give a ring-like structure of the polynuclear cation. The structure of the polynuclear complexes has an important role for the determination of the precipitate phase. On heating, the polynuclear complexes are further hydrolyzed and transformed into various precipitates. The $\text{Fe}_2(\text{OH})_3(\text{NO}_3)_3$ and $\text{Fe}_2(\text{OH})_3(\text{SO}_4)_{3/2}$ complexes form the precipitate of $\alpha\text{-FeO}(\text{OH})$, and the $\text{Fe}_2(\text{OH})_2\text{OCl}_2$ complex forms the $\beta\text{-FeO}(\text{OH})$ precipitate. When the temperature is raised above approximately 90°C , the structure of the polynuclear complexes varies, which results in the precipitation of $\alpha\text{-Fe}_2\text{O}_3$ [7].

In the case that ferric ion coexists with divalent cation, which can form the corresponding spinel ferrite, the divalent cation can be incorporated into the ferric polymerized clusters and the clusters are thermally transformed into spinel ferrite at above 60°C . At the precipitation temperature lower than 100°C , the particle size of the precipitated spinel phase is less than 10nm, since the particle size of the hydroxide-like

cluster almost remains unchanged. In order to obtain larger particles, higher precipitation temperature is required. The use of the autoclave apparatus provides the ferrite particles with the average diameter larger than 50nm.

It should be noted that the chemical composition in the precipitated phase may be different from that in the aqueous solution, because of the differences in the solubility and the hydrolysis degree of the metal ions. Therefore, we have to carefully select the pH value or the temperature of the aqueous solution. For example, Zn^{2+} ions can be incorporated into the precipitates only in the case that the aqueous suspension has the neutral pH. The incorporation of Co^{2+} ion occurs at the pH value larger than approximately 9. The incorporation of Mn^{2+} is possible in neutral or alkaline suspension. However, we note that Mn ions have various valence states, especially high valence state. Ni^{2+} ion almost remains in the hydroxide state and can hardly be incorporated into the spinel lattice.

Ferric ions can also be supplied by the oxidation of ferrous ions. In the industrial process, the Fe^{2+} - M^{2+} aqueous solutions were mixed with alkaline NaOH or KOH solution, then the gel suspensions were oxidized by air bubbling or addition of NO_3^- oxidant to prepare the spinel ferrite. In this reaction, the concentration of ferric ions depends on the oxidation velocity of ferrous ions, and the super-saturation degree of ferric ions are suppressed to produce larger particles, since the dependence of the nucleation rate on the super-saturation degree is larger than that of the growth rate.

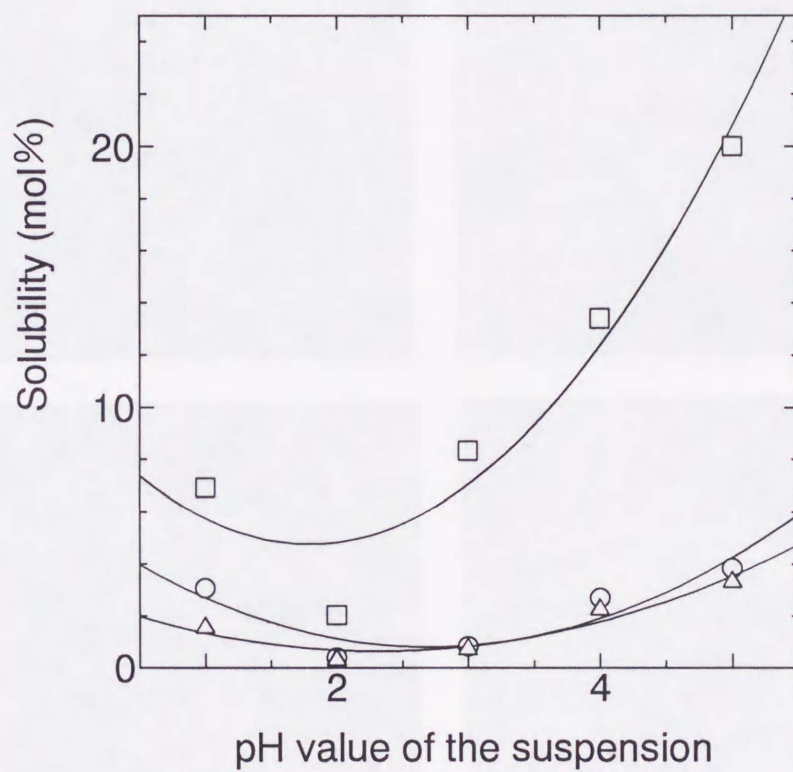
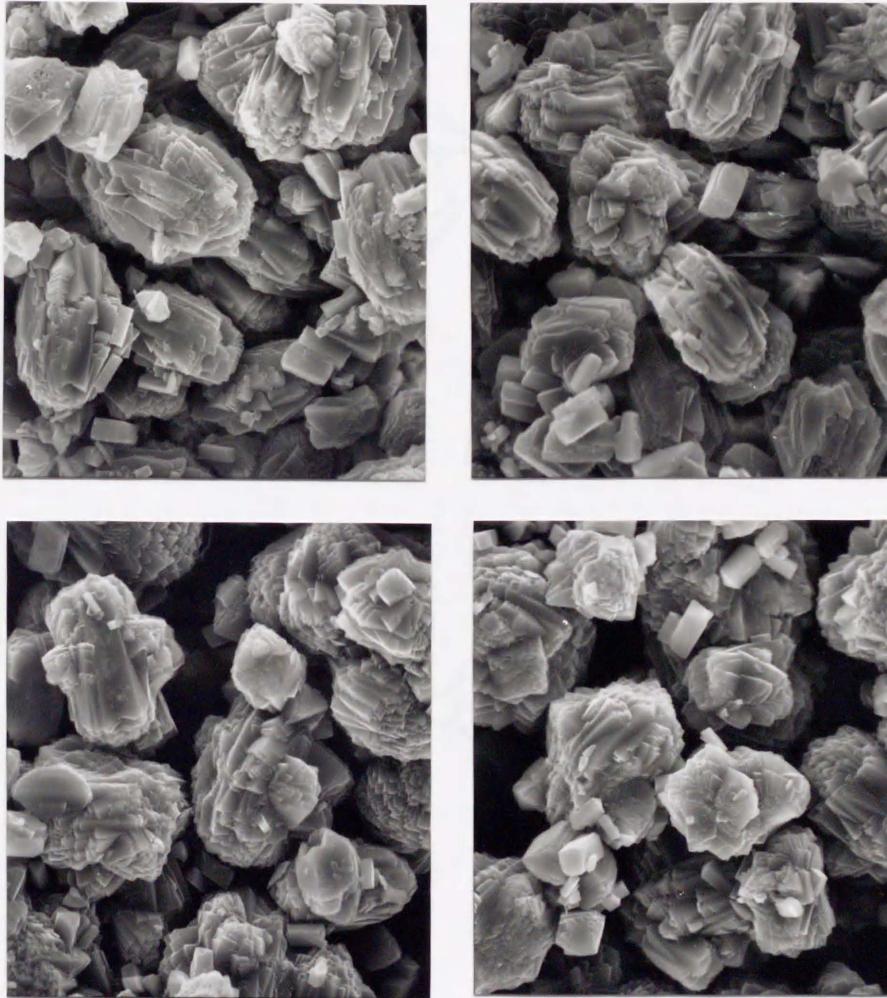
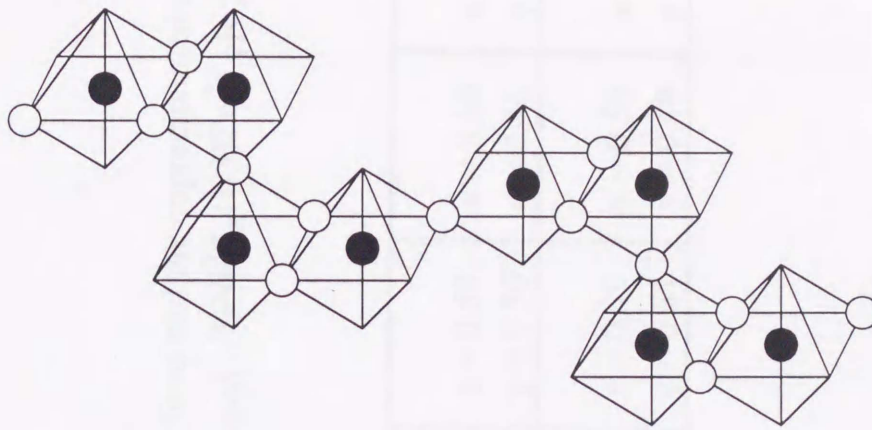


Figure 3-1 : The solubility of Fe²⁺(○), Ni²⁺(□) and Zn²⁺(△) in the oxalate solution at various pH values.

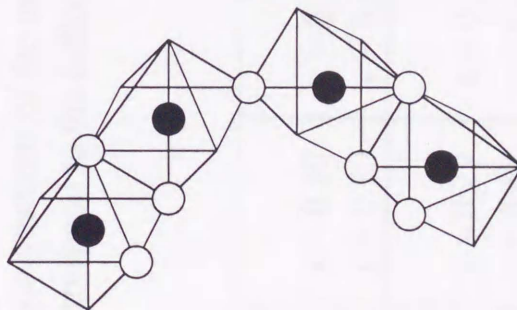


10 μ m

Figure 3-2 : SEM photographs of the coprecipitated (Ni,Zn,Fe)-oxalate precursor particles



(a)



(b)

Figure 3-3 : Structure of the polynuclear complex in the case of the counter anion SO_4^{2-} or NO_3^- (a), and in the case of the counter anion Cl^- (b). The solid and open circles denote ferric and oxygen ions, respectively.

Table 3-1 : Chemical compositions of the mixed aqueous solutions and the coprecipitated oxalates.
 x and y correspond to the indices in $[(2/3)Fe^{2+}_{1-x-y}(1/3)Ni^{2+}_x(1/3)Zn^{2+}_y]C_2O_4 \cdot 2H_2O$.

Composition in the solutions	$x = 0.20$	$x = 0.30$	$x = 0.35$	$x = 0.40$	$x = 0.50$	$x = 0.60$	$x = 0.70$	$x = 0.80$
	$y = 0.80$	$y = 0.70$	$y = 0.65$	$y = 0.60$	$y = 0.50$	$y = 0.40$	$y = 0.30$	$y = 0.20$
Composition in the precipitates	$x = 0.19$	$x = 0.29$	$x = 0.33$	$x = 0.39$	$x = 0.49$	$x = 0.55$	$x = 0.67$	$x = 0.78$
	$y = 0.78$	$y = 0.68$	$y = 0.64$	$y = 0.59$	$y = 0.51$	$y = 0.40$	$y = 0.30$	$y = 0.21$

Chapter 4

Frequency dispersion of complex permeability

The complex permeability and its frequency dispersion of the materials determine the characteristics of high frequency devices. Their control is important for the industrial device, and the clarification of the controlling factor is a useful study on the magnetizing mechanisms in high frequency region. In general, when the AC magnetic field $H_0 \exp(-j\omega t)$ is applied to the magnet, a magnetization is induced. For low-frequency field, the magnetization evolves concurrently with the applied field, since the AC field varies so slowly. However, as the frequency of AC field becomes higher, the time evolution of the magnetization cannot follow that of the AC field resulting in a phase delay (δ). The permeability is given by their ratio,

$$\begin{aligned} \mu(\omega) &= (B(\omega)/H(\omega)) = B_0 \exp(-j\omega t + j\delta) / H_0 \exp(-j\omega t) \\ &= (B_0/H_0) \exp(j\delta) \end{aligned} \quad (4.1)$$

Therefore,

$$\operatorname{Re}[\mu(\omega)] = (B_0/H_0) \cos\delta \quad (4.2a)$$

$$\operatorname{Im}[\mu(\omega)] = (B_0/H_0) \sin\delta \quad (4.2b)$$

The phase shift (δ) is closely related to the energy loss in the materials. The permeability is attributed to the magnetizing mechanisms, and there are both coherent and incoherent mechanisms. The former is attributed to the spin rotation and the origin of the latter is in the domain wall motion. Therefore, the phase shift is also related to the dissipation terms

in both the spin rotation and the domain wall motion.

Before discussing on the magnetizing mechanisms, the measurement techniques for the complex permeability are briefly described. In low frequency region, the complex permeability is evaluated from the toroidal core impedance. Considering the toroidal core of the magnet (a , b and r are the thickness, the width and the radius of the toroidal core, respectively) in Fig. 4-1, the complex impedance Z is given as,

$$Z(\omega) = j\omega ab\mu(\omega)N^2/2\pi r \quad (4.3)$$

with N the turn number of the coil and $\mu(\omega)$ the permeability of the magnet. The substitution of $\mu(\omega) = \mu'(\omega) + j\mu''(\omega)$ into (4.3) provides the equation

$$Z(\omega) = j\omega(abN^2/2\pi r) [\mu'(\omega) + j\mu''(\omega)] . \quad (4.4)$$

We measure the complex impedance with the impedance analyzer as the summation of the resistivity $R(\omega)$ and the inductance $L(\omega)$,

$$Z(\omega) = R(\omega) + j\omega L(\omega) . \quad (4.5)$$

Therefore, we obtain the complex permeability as follows :

$$\mu'(\omega) = (2\pi r/abN^2) L(\omega) \quad (4.6a)$$

$$\mu''(\omega) = (2\pi r/abN^2) (R(\omega)/\omega) . \quad (4.6b)$$

However, the capacitance between the wound wires cannot be neglected in high frequency region, hence this impedance method is limited to the frequency region less than about 10MHz.

In high frequency regions, the complex impedance can be evaluated with the equivalent circuit calculation using the network analyzer. Considering two parallel transport lines, shown in Fig. 4-2, the voltages and currents on both sides of the element (the complex permeability of $\mu(\omega)$ and the complex permittivity of $\epsilon(\omega)$) are connected with the transfer matrix T as follows.

$$\begin{pmatrix} V_1 \\ I_1 \end{pmatrix} = T \begin{pmatrix} V_2 \\ I_2 \end{pmatrix} \quad (4.7a)$$

$$\text{and } T = \begin{pmatrix} \cosh(\beta d) & Z_w \sinh(\beta d) \\ (1/Z_w) \sinh(\beta d) & \cosh(\beta d) \end{pmatrix} \quad (4.7b)$$

with $Z_w = Z_0[\mu(\omega)/\epsilon(\omega)]^{1/2}$, $\beta = j(\omega/c)[\epsilon(\omega)\mu(\omega)]^{1/2}$ and Z_0 being the characteristic impedance ($=120\pi\text{ohm}$) in the free space. Now, the thickness of the element (d) is sufficiently small as compared with the wave length of the electromagnetic wave corresponding to the frequency, so we can approximately write $\sinh(\beta d) \sim \beta d$ and $\cosh(\beta d) \sim 1$. Furthermore, locating the element onto the metal plate, which is equivalent to $V_2=0$, leads to the equations

$$V_1 = Z_0(j\omega/c)\mu(\omega)d I_1 \quad \text{and} \quad I_1 = I_2 \quad (4.8)$$

Therefore, the complex impedance $Z(\omega)$ is obtained as the ratio of (V_1/I_1) , from which the complex permeability is obtained as,

$$\mu'(\omega) = \text{Im}[Z(\omega)] / [Z_0(\omega/c)d] \quad (4.9a)$$

$$\mu''(\omega) = \text{Re}[Z(\omega)] / [Z_0(\omega/c)d] \quad (4.9b)$$

It is noted that this evaluation method is also limited by the condition of $\beta d \ll 1$. For example, if the sample thickness is about 5mm, the threshold frequency is about 1GHz (the wave length of 30cm).

4.1 Spin rotational permeability

First, we consider the spin rotational magnetizing mechanism. It is considered that the magnetic material with magnetic moment \mathbf{M} is located in a uniform and static magnetic field \mathbf{H} . The magnetostatic energy is represented by the summation of the anisotropy energy and the Zeeman energy as,

$$E = -K_u(\sin\theta)^2 + HM_0\cos(\theta-\theta_0) \quad (4.10)$$

where K_u denotes the uniaxial magnetic anisotropy constant, and θ is the angles between the magnetic moment and the applied field and θ_0 is that between the magnetic easy axis and the applied field, respectively (See Fig. 4-3). In the equilibrium state, $(dE/d\theta)=0$ gives the solution,

$$\theta = HM_0 \sin \theta_0 / 2K_u \quad (4. 11)$$

under the condition that the applied field is low enough to satisfy the inequality $HM_0 \ll K_u$. Since the magnetization induced by the applied field is given as $M_0 \cos(\theta - \theta_0)$, the magnetic susceptibility is,

$$\begin{aligned} \chi &= d[M_0 \cos(\theta - \theta_0)]/dH = -M_0 \sin(\theta - \theta_0) (d\theta/dH) \\ &= (M_0 \sin \theta_0)^2 / 2K_u . \end{aligned} \quad (4. 12)$$

Assuming the random orientation of the magnetic easy axis (as in polycrystalline material and particulate materials), the average value of $(\sin \theta_0)^2 = 2/3$ leads to the expression,

$$\chi = M_0^2 / 3K_u . \quad (4. 13)$$

From this equation, it is found that the susceptibility is proportional to the square of the magnetization and inversely proportional to the magnetic anisotropy constant.

Now, considering AC applied field, the magnetic moment is characterized by the precession motion around the direction of the total magnetic field because of the gyroscopic properties of the magnetic moment, and has an interaction with the AC applied field. The equation of motion is given by the Landau-Lifshitz-Gilbert equation[1,2,3],

$$(d\mathbf{M}/dt) = \gamma (\mathbf{M} \times \mathbf{H}) - (\alpha/H) [\mathbf{M} \times (d\mathbf{M}/dt)] \quad (4. 14)$$

where γ is the gyromagnetic constant, α is the damping coefficient of the precession motion, and the magnetic field \mathbf{H} consists of the exchange interaction field ($=\eta\mathbf{M}$, η being the molecular field coefficient), magnetocrystalline anisotropy field \mathbf{H}_a , the demagnetizing field ($=-N\mathbf{M}$, N being the demagnetizing factor), and the applied AC field \mathbf{H}^{rf} . Assuming the configuration that the AC applied field is perpendicular to the anisotropy field and the anisotropy field is directed along the z-axis, each component of the magnetic field is given by

$$H_x = (\eta - N_x)M + H_x^{rf} \quad (4. 15a)$$

$$H_y = (\eta - N_y)M + H_y^{rf} \quad (4. 15b)$$

$$H_z = (\eta - N_z)M + H_a . \quad (4. 15c)$$

If we use the relations $\mathbf{M}=(m_x \exp(j\omega t), m_y \exp(j\omega t), M_0)$ and $\mathbf{H}^f=(H_x^f \exp(j\omega t), H_y^f \exp(j\omega t), 0)$, these equations are re-written up to the first-order perturbed terms of m and H^f ,

$$\begin{pmatrix} m_x \\ m_y \end{pmatrix} = \frac{\gamma M_0}{(\omega_{sp} + j\alpha\omega)^2 - \omega^2} \begin{pmatrix} \omega_{sp} + j\alpha\omega & j\omega \\ j\omega & \omega_{sp} + j\alpha\omega \end{pmatrix} \begin{pmatrix} H_x^f \\ H_y^f \end{pmatrix} \quad (4. 16)$$

with the resonance frequency of the spin rotation ω_{sp} ,

$$\omega_{sp}^2 = \gamma^2 [H_a + (N_y - N_z)M_0] [H_a + (N_x - N_z)M_0] . \quad (4. 17)$$

Therefore, the spin rotational susceptibility is obtained by the following equation,

$$\chi_{sp}(\omega) = \gamma M_0 (\omega_{sp} + j\alpha\omega) / [(\omega_{sp} + j\alpha\omega)^2 - \omega^2] . \quad (4. 18)$$

In the ferrite materials, the damping factor is large enough ($\alpha\omega \gg \omega_{sp}$), so that equation (4. 18) is of a relaxation-type rather than resonance-type,

$$\chi_{sp}(\omega) = \gamma M_0 / [1 + j(\alpha\omega/2\omega_{sp})] . \quad (4. 19)$$

From equations (4. 13) and (4. 17), we get the relations

$$\chi_{sp}(0) = M_0^2 / 3K_u \quad \text{and} \quad \omega_{sp} = \gamma H_a = \gamma (K_u / M_0) . \quad (4. 20)$$

Therefore, the product of the static susceptibility and the spin rotational resonance frequency is given by

$$\chi_{sp}(0)\omega_{sp} = (2/3) \gamma M_0 . \quad (4. 21)$$

This implies that the resonance frequency shifts toward a lower value as the static permeability increases, which is called the Snoek's law. In the ferrite materials, it is known that the upper limit of the Snoek's product is about 5.6GHz[4].

4. 2 Domain wall motion contribution

Next, we consider the contribution from the domain wall motion. The domain wall motion is promoted the magnetic stress induced by applied field. It is assumed that the magnetic material with magnetic moment \mathbf{M} is located in uniform magnetic field \mathbf{H}

and that there are only 180° domain walls in the materials (Fig. 4-4). The equation of the domain wall motion is,

$$m(d^2X/dt^2) + \beta(dX/dt) + \alpha X = 2MH\cos\phi \quad (4. 22)$$

where X denotes the displacement of the domain wall, and ϕ is the angle between the magnetic moment and the applied field, m is the effective mass of the domain wall, α is the elastic constant for the wall motion, and β is the damping coefficient for the wall motion. In the case of the static field, the wall displacement is independent of time, so that the equation (4. 22) is converted to

$$X = 2(MH/\alpha)\cos\phi . \quad (4. 23)$$

The wall displacement leads to the net magnetization ΔM given by

$$\Delta M = X \times 2M\cos\phi = (4M^2H/\alpha)\cos^2\phi . \quad (4. 24)$$

Therefore, we get the domain wall susceptibility as follow :

$$\chi_{dw} = (2M\cos\phi)^2/\alpha . \quad (4. 25)$$

Assuming that the domain wall configuration is random in the materials, the average value of $(\cos\phi)^2$ is $1/3$ and the equation (4. 25) is re-written as

$$\chi_{dw} = (2M)^2/3\alpha . \quad (4. 26)$$

From this equation, it is found that the domain susceptibility is proportional to the square of the magnetization as well as the spin susceptibility (see equation (4. 13)).

In the case of the AC field, the vibration of the domain wall interacts with the AC field and the interaction produces a frequency-dependent susceptibility. For the net magnetization $\Delta M = X \times 2M\cos\phi$, the equation of motion is,

$$m(d^2\Delta M/dt^2) + \beta(d\Delta M/dt) + \alpha\Delta M = 4M^2H\cos\phi . \quad (4. 27)$$

Setting $H(t)=H_0\exp(j\omega t)$ and $\Delta M(t)=\Delta M_0\exp(j\omega t)$, this equation is transformed to

$$\Delta M_0 = 4M^2H_0\cos\phi / (-m\omega^2 + j\beta\omega + \alpha) , \quad (4. 28)$$

therefore, the domain wall susceptibility is given by

$$\chi_{dw}(\omega) = (\Delta M_0/H_0) = 4M^2\cos\phi / (-m\omega^2 + j\beta\omega + \alpha) . \quad (4. 29)$$

This indicates that the resonance occurs at the frequency $\omega_{dw}=(\alpha/m)^{1/2}$. Using equation

(4. 26) for the static susceptibility, we get the Snoek's product for the domain wall motion,

$$[\chi_{dw}(0)]^{1/2}\omega_{dw} = 2M/(3\alpha)^{1/2} . \quad (4. 30)$$

As in the case of the expression of the spin susceptibility (4. 21), this implies that the resonance frequency shifts to lower frequency as the static permeability increases. In the ferrite materials, it is known that the upper limit of the Snoek's product is about 95MHz[4].

4. 3 Inverse cole-cole plot technique

In this section, the decomposition technique of the complex permeability spectra into spin rotational and domain wall contributions, known as the inverse cole-cole plot[4], is described. The total complex permeability is expressed as

$$\mu(\omega) = 1 + \chi_{sp}(\omega) + \chi_{dw}(\omega) . \quad (4. 31)$$

From equations (4. 19) and (4. 29), the spin rotational component $\chi_{sp}(\omega)$ is of relaxation-type and its dispersion is inversely proportional to the frequency, but the domain wall component $\chi_{dw}(\omega)$ is of resonance type and depends on the square of the frequency. They are written as follows.

$$\chi_{sp}(\omega) = K_{sp} / [1+j(\omega/\omega_{sp})] \quad (4. 32a)$$

$$\chi_{dw}(\omega) = K_{dw}\omega_{dw}^2 / (\omega_{dw}^2 - \omega^2 + j\beta\omega) . \quad (4. 32b)$$

Considering the difference in the frequency dependence, only the spin rotational component remains in high frequency region such as 100MHz band. Therefore, at high frequency region, the inverse value of the permeability is given as,

$$[1/\chi(\omega)] = g_1 + jh_1 = (1/K_{sp})[1+j(\omega/\omega_{sp})] . \quad (4. 33)$$

In the g-h plane, shown in Fig. 4-5, equation (4. 33) indicates a straight line with the intercept of $(1/K_{sp}, 0)$. That is, K_{sp} is determined from the intercept value, and the point on the straight line at an appropriate frequency provides the ω_{sp} value. Using these parameters, we can get the spin component (χ_{sp}) numerically.

In low frequency region, the domain wall contribution cannot be neglected and two contributions of spin rotation and domain wall motion are superimposed. Since the spin contribution can be numerically estimated from the high frequency permeability, we can calculate the domain contribution by the numerical subtraction of the spin contribution from total permeability.

$$\chi_{dw}(\omega) = \chi(\omega) - \chi_{sp}(\omega) = g_2 + jh_2 \quad (4.34)$$

Therefore, the g-h plot, shown in Fig. 4-6, provides the parabolic curve with the use of (4.32b),

$$g_2 = (1/K_{dw}) - (K_{dw}\omega_{dw}^2/\beta^2) h_2^2 \quad (4.35)$$

It has intercepts at $(1/K_{dw}, 0)$ and $(0, \beta/K_{dw}\omega_{dw})$. From these intercept values and the point on the parabolic line at an appropriate frequency, we can get the parameters for the domain wall component and can evaluate the domain wall contribution numerically.

For example, the permeability spectra of Ni-Zn ferrite sintered ceramics are decomposed by following the above procedures. The characteristics of the specimen are as follows :

chemical composition $Ni_{0.26}Zn_{0.67}Cu_{0.07}Fe_{2.0}O_4$

sintering density 5.20 g/cm^2

lattice constant $a=0.840\text{nm}$

magnetization at 300K $M_s=46\text{emu/g}$

Curie temperature $T_c=380\text{K}$

Figure 4-7 shows the measured complex permeability spectra. The real part of the permeability $\mu'(\omega)$ is about 1400 in the low frequency region and it begins to decrease at about 1MHz. The imaginary part of the permeability $\mu''(\omega)$ takes a peak of about 800 at around 1MHz. The inverse values of the permeability in the frequency region larger than 10MHz are plotted in Fig. 4-8(a). The experimental values in the region of 30 to 100MHz make a trace of straight line, and it is fitted to equation (4.33). Therefore, the parameters of the spin rotational contribution are obtained as :

$$K_{sp} = 840 \quad \text{and} \quad \omega_{sp} = 9.17\text{MHz} . \quad (4. 36)$$

Next, the subtraction of the spin components, which calculated from equation (4. 33) and the values (4. 36), from the total permeability produce the domain wall contribution. The inverse values of the domain wall contribution are also plotted in Fig. 4-8(b). The values in the region of 2 to 6MHz make a trace of a parabolic line, and it is fitted to equation (4. 35). Therefore, the parameters of the domain wall component are obtained as :

$$K_{dw} = 600 , \quad \omega_{dw} = 3.62\text{MHz} \quad \text{and} \quad \beta = 5.34\text{MHz} . \quad (4. 37)$$

Using set of equations (4. 32) with the parameters obtained in (4. 36) and (4. 37), the complex permeability spectra can be calculated, which are shown as the solid lines in Fig. 4-7. Each calculated spectrum of spin rotation and domain wall motion is also shown in this figure. Good agreement between the experimental permeability dispersion and the calculated curve is attained. It is found that the complex permeability in high frequency region above 100MHz can be described only with the spin rotational component.

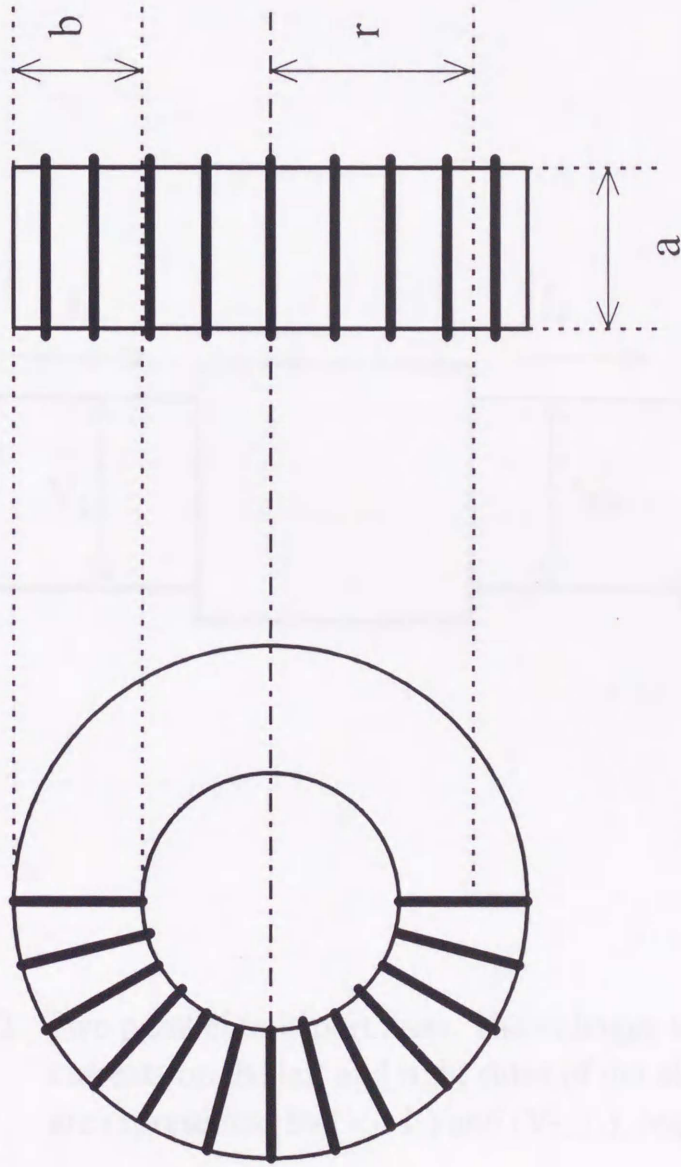


Figure 4-1 : Toroidal core of the magnet. a , b and r are the thickness, the width and the radius of the toroidal core, respectively.

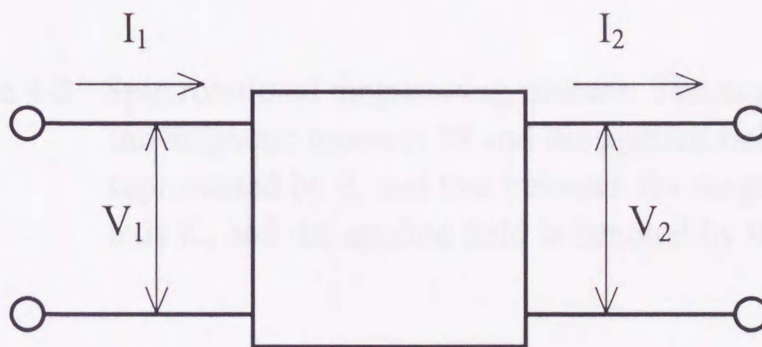


Figure 4-2 : Two parallel transport lines. The voltages and the currents on the left and right sides of the element are represented by (V_1, I_1) and (V_2, I_2) , respectively.

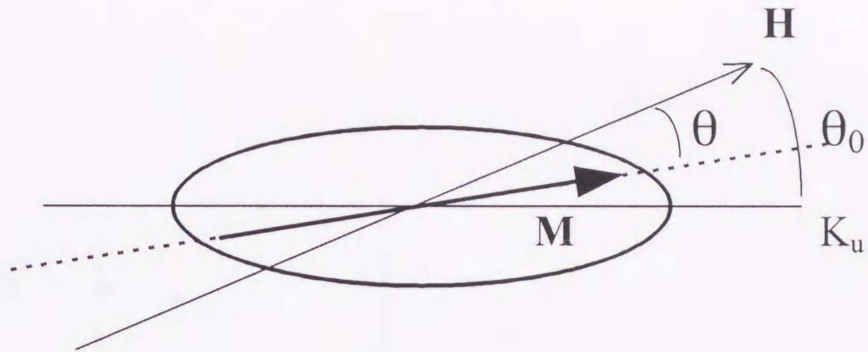


Figure 4-3 : Spin rotational magnetizing process. The angle between the magnetic moment \mathbf{M} and the applied field \mathbf{H} is represented by θ , and that between the magnetic easy axis K_u and the applied field is denoted by θ_0 .

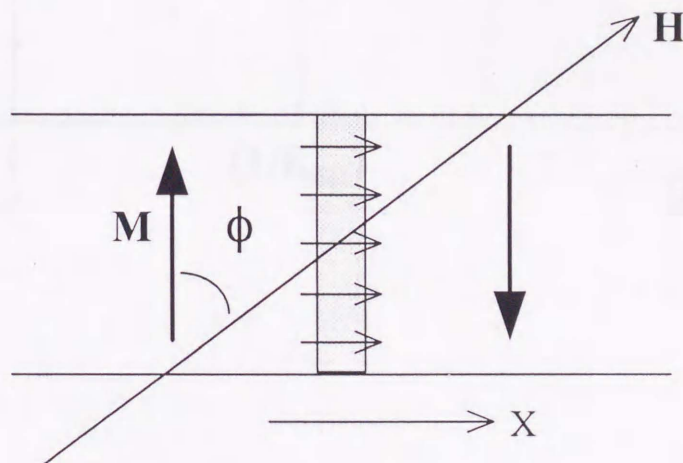


Figure 4-4 : Domain wall motion under the applied field. The angle between the magnetic moment \mathbf{M} and the applied field \mathbf{H} is represented by ϕ .

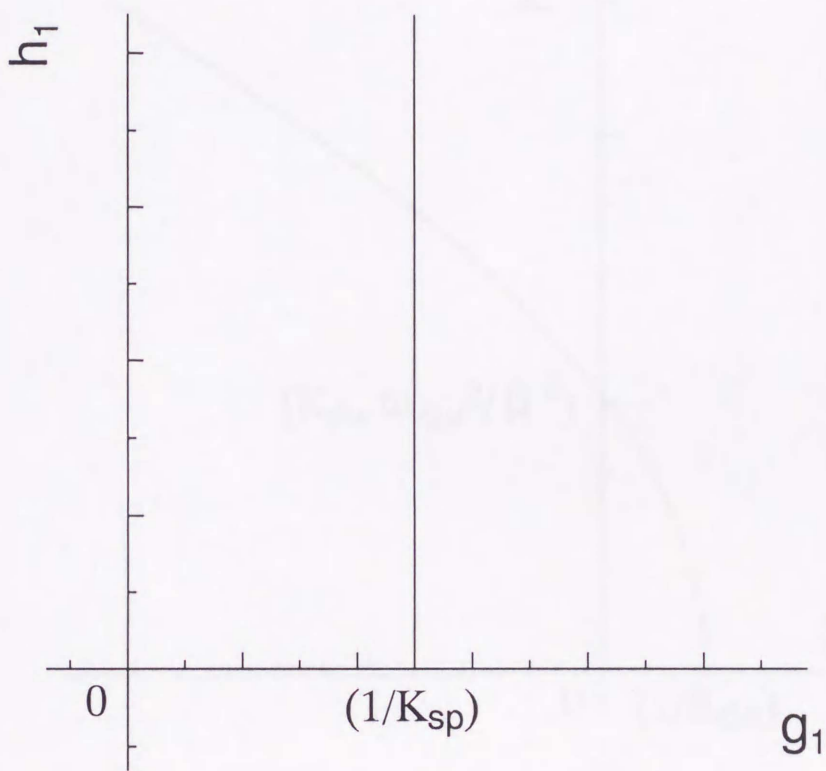


Figure 4-5 : The g-h plot of the spin rotational permeability.
The intercept of the straight line provides the K_{sp} value.

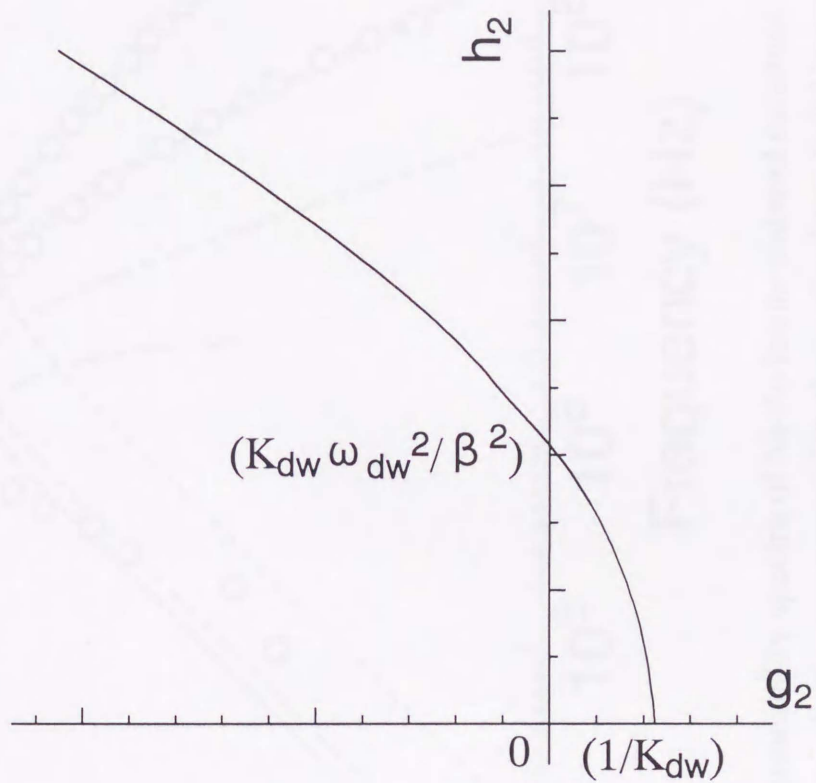


Figure 4-6 : The g-h plot of the domain wall contribution.
 The values of K_{dw} , ω_{dw} and β are obtained from the intercepts of the parabolic curve.

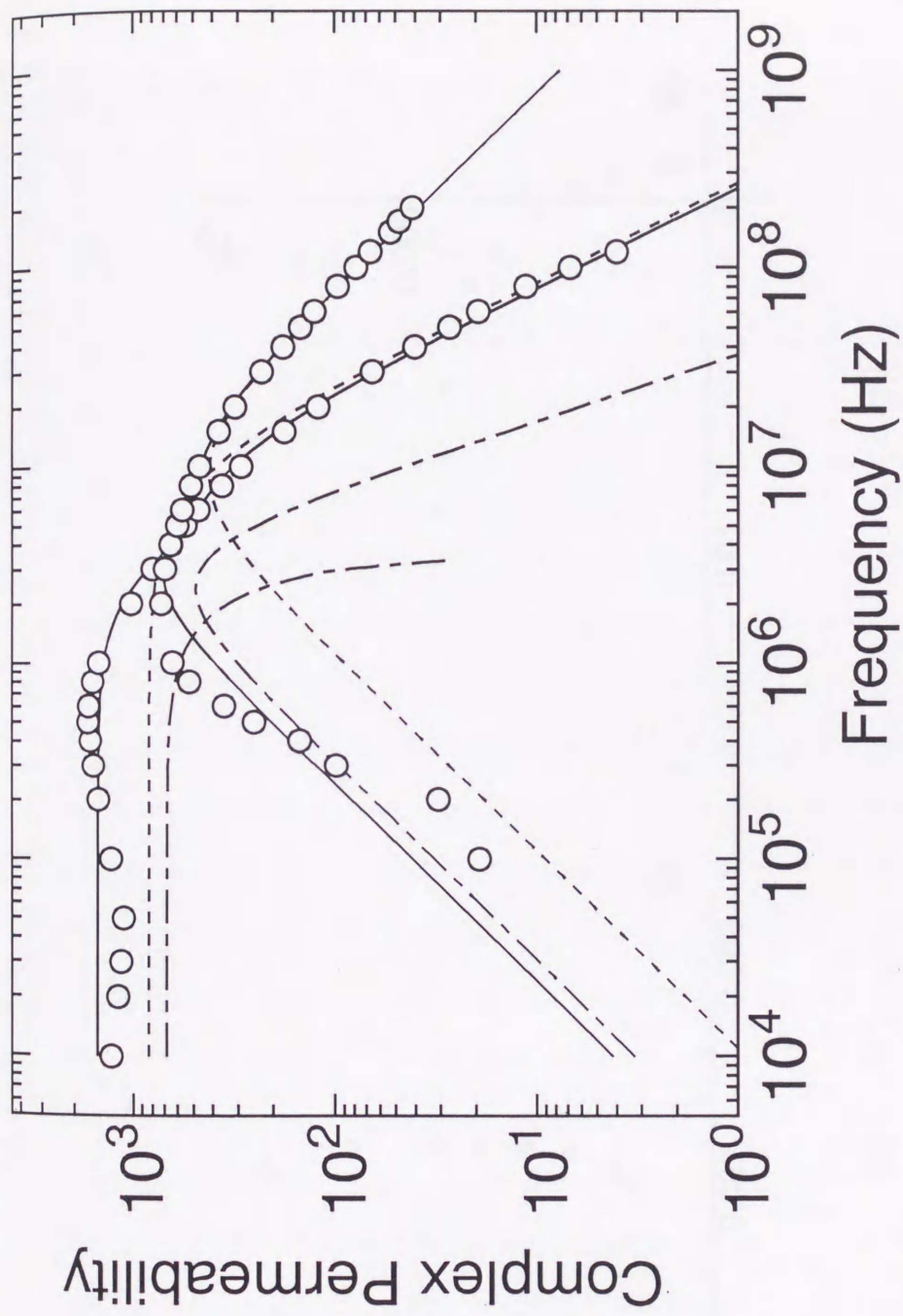


Figure 4-7 : The complex permeability spectra of Ni-Zn ferrite sintered ceramics. The open circles indicate experimentally obtained values. Solid lines show the total calculated permeability which is obtained by combining the spin rotational component (broken lines) and the domain wall contribution (dash-dotted lines).

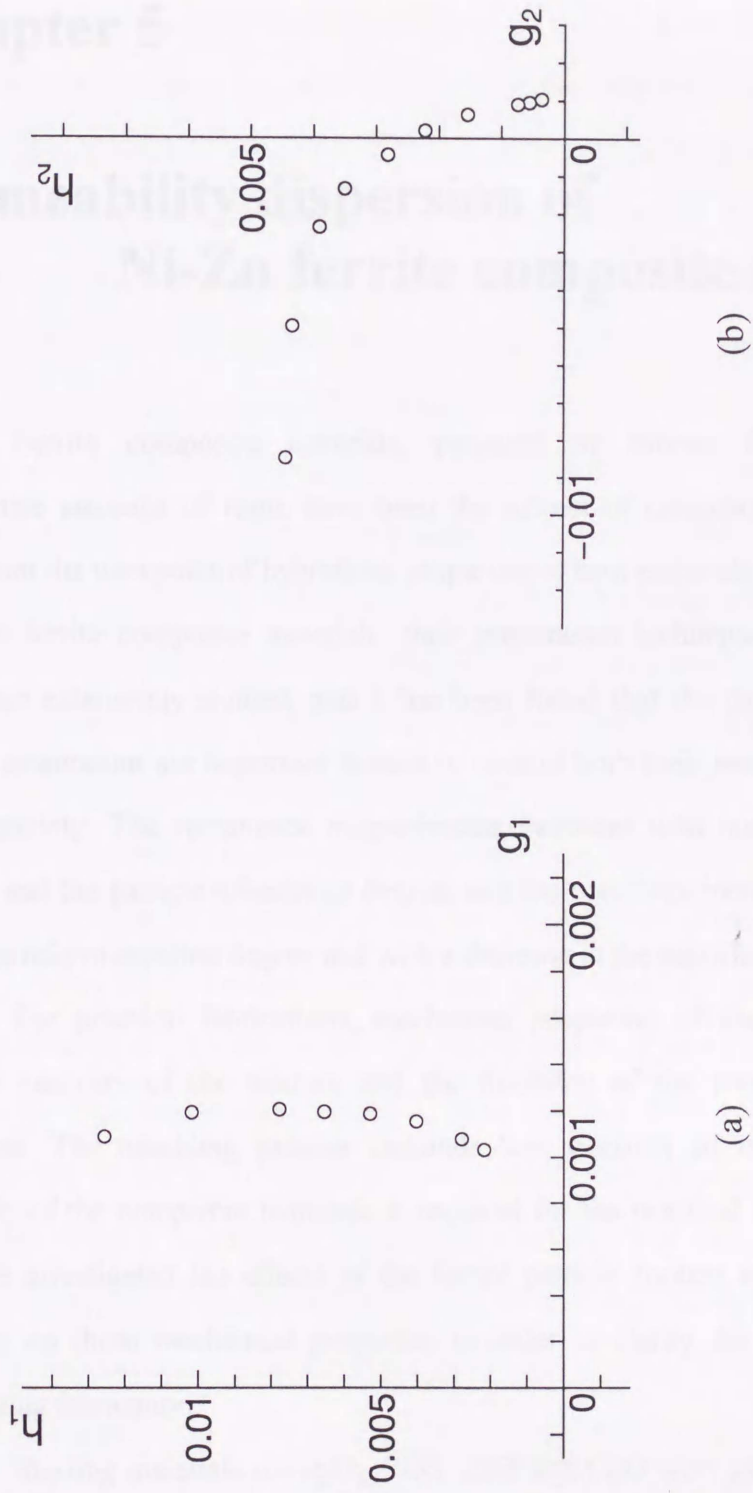


Figure 4-8 : The inverse values of the permeability plotted in the g-h plane.
 (a) the spin rotational component and (b) the domain wall contribution.

Chapter 5

Permeability dispersion of Ni-Zn ferrite composite materials

Ferrite composite materials, prepared by mixing ferrite particles with appropriate amounts of resin, have been the subject of considerable interest in recent years from the viewpoint of hybridized properties of host materials and ferrite. Especially for hard ferrite composite materials, their preparation technique and characterization have been extensively studied, and it has been found that the particle content and the particle orientation are important factors to control both their remanence magnetization and coercivity. The remanence magnetization increases with increases in the particle content and the particle orientation degree, and the coercivity increases with an increase in the particle orientation degree and with a decrease in the particle content.

For practical fabrications, mechanical properties of the composite materials, such as viscosity of the mixture and the flexibility of the composite materials, are important. The moulding process demands low viscosity of the mixture, and high flexibility of the composite materials is required for the practical application. Therefore, we have investigated the effects of the ferrite particle content and the ferrite particle diameter on these mechanical properties in order to clarify the limitation of the roll compacting fabrication.

Starting materials α -Fe₂O₃, NiO, ZnO and CuO were ground together by wet attrition milling, and mixtures were calcined in air at 900°C for 2 hours. The pre-sintered

powders were re-ground by wet attrition milling and mechanical granulation (the particle diameter is from 2 to 5mm). Granulated particles were sintered in air at 1100 °C for 3 hours and slowly cooled to room temperature. It was identified from the powder X-ray diffraction that the particles have a single phase of spinel ferrite and the inductively coupled plasma analysis led to the composition of $\text{Ni}_{0.24}\text{Zn}_{0.65}\text{Cu}_{0.07}\text{Fe}_{2.04}\text{O}_4$. The sintered ceramics were subjected to the vibration milling for various period, and fine particles (the average particle diameter is less than 7.4 μm) and coarse particles (the average particle diameter is greater than 85 μm) of ferrite were obtained. The ferrite powders and EVA (Ethylene-Vinyl-Acetate co-polymer) resin were mixed with the ferrite content of 30, 50 and 70vol%, kneaded at 120 °C, and compacted by rolling (the thickness of the rolled sheet of approximately 2.0mm). The rolled compacts were heated to 130 °C and the viscosity was measured from the relationship between the loading and the flow velocity (Shimadzu Flow Tester CFT-500). Hardness of the rolled compacts was also measured by the penetrometer (Kobunshi-Keiki, Hardness Tester Type-D), and the flexibility was evaluated by the practical handling.

The experimental results are summarized in Table 5-1. The viscosity abruptly increases at the ferrite content of about 70vol%, which is almost equal to the critical volume concentration. Fine particles of ferrite may tend to strongly aggregate and form some structures in the mixture, so that the viscosity of the mixture with fine ferrite particles becomes higher than that with coarse particles. While coarse particles provide low viscosity of the mixture, it has poor flexibility in the final composite materials. Therefore, there is a trade-off between the productivity and the flexibility of the composite materials. In addition, the composite with high ferrite content (the volume loading larger than approximately 70%) cannot be prepared by roll compacting and they are obtained only by the press compacting. The roll compacting process is suitable only for the production of the composite materials with low ferrite content.

5.1 Complex permeability spectra

Ni-Zn ferrite powders were prepared by thermal decomposition of co-precipitated oxalate precursors at 850 °C in air, the preparation and characterization of which have been already described in chapter 3. The ferrite powders were re-ground by wet attrition milling and mechanical granulation (the average particle diameter is from 0.2 to 1.5mm). Granulated particles were sintered in air at 1100 °C for 3 hours and slowly cooled to room temperature. It was identified from the powder X-ray diffraction that the particles have a single phase of spinel ferrite with the lattice constant of 0.840nm, and the inductively coupled plasma analysis led to the chemical composition of $\text{Ni}_{0.26}\text{Zn}_{0.67}\text{Cu}_{0.07}\text{Fe}_{2.0}\text{O}_4$. In addition, the magnetic measurement gives the Curie temperature of $T_C=380\text{K}$. The ferrite composite materials were made by mixing the ferrite particles with appropriate amounts of EVA resin and pressing the mixture into a ring form. The inner and outer diameters were 17 and 38.5mm, respectively. Several samples with thickness from 5 to 10mm were prepared. Since both the ferrite particle diameter and the ferrite content can be important factors in the complex permeability in ferrite composite materials, two series of samples were prepared to examine the effects of the ferrite particle diameter and the ferrite content on the complex permeability. These were : (1) almost the same ferrite content and different particle diameters, and (2) almost the same particle diameters and different ferrite content. The complex permeabilities of the samples were measured by two different techniques. In the frequency range from 100kHz to 10MHz, the complex permeability was obtained by measuring the inductance and the resistance of coil-wound toroidal sample, using a LF impedance analyzer (Hewlett Packard 4192A). In the frequency range from 1MHz to 1GHz, the complex permeability was obtained by measuring the input impedance of the sample by coaxial line technique with an RF-network analyzer (Hewlett Packard 8510B).

Figure 5-1(a) shows the variation of the real part of the permeability at 100kHz and 100MHz with the average diameter of the ferrite particles, where the ferrite content

was kept almost constant (the density of approximately 3.7g/cm^2). Figure 5-1(b) indicates the variation of the real permeability at 100kHz and 100MHz with the density of the ferrite composite materials, where the average particle diameter of the ferrite was kept constant at 1.5mm. These two figures imply that the permeability depends only on the density of the ferrite composite materials, i.e. the ferrite particle content. Therefore, we consider only the effects of the ferrite content below.

The frequency dispersion curves of the complex permeability in the ferrite composite materials and the sintered ferrite are shown in Fig. 5-2 ((a) real part and (b) imaginary part). The numerical analysis about the complex permeability of the sintered ferrite has already been described in chapter 3, the results of which are as follows. The parameters for the spin rotational contribution are,

$$K_{sp} = 840 \quad \text{and} \quad \omega_{sp} = 9.17\text{MHz} , \quad (5. 1)$$

and the parameters of the domain wall component are,

$$K_{dw} = 600 , \quad \omega_{dw} = 3.62\text{MHz} \quad \text{and} \quad \beta = 5.34\text{MHz} . \quad (5. 2)$$

The dispersion curves of the complex permeability in the ferrite composite materials are also shown in Fig. 5-2. Samples E, F, G and H have the ferrite particle content of 72.0, 68.0, 57.0 and 49.0vol%, respectively. Samples B, C and D, with high ferrite contents of 98.8, 97.6 and 95.4vol%, were prepared by cracking the sintered ferrite core and by bonding them together again. In the low frequency region, both the real and imaginary parts of the complex permeability decrease with a decrease in the ferrite content. On the other hand, in high frequency region (for example, about 100MHz), the real part of the permeability in the ferrite composite materials is larger than that of the sintered ferrite. As the ferrite content decreases, both the shoulder frequency of the real part and the peak frequency of the imaginary part shift toward higher values. The cracking of the sintered ferrite core (samples B, C and D) also leads to the same type of changes in the frequency dispersion of the complex permeability : both the real and imaginary parts of the low-frequency permeability are significantly

reduced, and the peak frequency of the imaginary part shifts toward higher frequency. In addition, it is important that the cracked core samples have intermediate complex permeability spectra between those of the sintered ferrite and the composite materials.

The spin resonance formulation, shown in (4. 32a), was applied to the complex permeability spectra in the ferrite composite materials, and the parameters in the spin rotation contribution were obtained by numerically fitting the experimental data in 100MHz region in Fig. 5-2 to equation (4. 32a). Table 5-2 shows the parameters of the samples examined. It is found that the K_{sp} value decreases and the resonance frequency ω_{sp} shifts toward higher frequency as the ferrite content is reduced.

5. 2 Magnetic circuit model

It is considered that the ferrite composite materials are composed of spherical polycrystalline ferrite particles surrounded by a non-magnetic resin layer. Although the ferrite particle diameter and the thickness of the non-magnetic resin layer have some distribution, only their average values are taken into account. The average particle size of the polycrystalline ferrite and the average thickness of the non-magnetic resin layer are denoted by D and $(\delta/2)$, respectively. The schematic configuration is shown in Fig. 5-3. There are two magnetic resistivities : intra-particle resistivity (grain boundary) and inter-particle resistivity (non-magnetic resin layer). Since the magnetic resistivity of the resin layer is much greater than that of the grain boundary within the ferrite particle, we can describe the magnetic circuit, that is the Ampere's integral, in the ferrite composite materials using only the magnetic resistivity of the resin layer as :

$$(D+\delta)/\mu = D/\mu_B + \delta , \quad (5. 3)$$

where μ and μ_B are the effective permeability of the ferrite composite materials and the permeability of the polycrystalline ferrite particle, respectively. It is unlikely that the values of D and δ change with the frequency. Furthermore, the permeability of the polycrystalline ferrite particle can be substituted by the permeability of the sintered ferrite.

Therefore, for the spin rotational permeability (4. 32a), we obtain the following equations, in which K_{sp} and ϖ_{sp} are functions of only the ratio (δ/D) :

$$\chi_{sp}(\omega) = K_{sp} / [1 + j(\omega/\varpi_{sp})] , \quad (5. 4a)$$

$$K_{sp} = K_{sp}^B [1 + (\delta/D)] / [1 + K_{sp}^B(\delta/D)] , \quad (5. 4b)$$

$$\varpi_{sp} = \varpi_{sp}^B [1 + K_{sp}^B(\delta/D)] , \quad (5. 4c)$$

where K_{sp}^B and ϖ_{sp}^B are the spin rotational parameters for the polycrystalline sintered ferrite. The ratio (δ/D) is related to the density of the ferrite composite materials, and it increases with a decrease in the density. The density of the composite materials ρ is given by

$$(D+\delta)^3 \rho = D^3 \rho_f + [(D+\delta)^3 - D^3] \rho_m \quad (5. 5)$$

where ρ_f and ρ_m are the densities of the ferrite and resin, respectively. Thus, the value of (δ/D) can be estimated from the density of the composite materials using the equation

$$[1 + (\delta/D)^3] = (\rho_f - \rho_m) / (\rho - \rho_m) . \quad (5. 6)$$

We call the ratio (δ/D) ' gap parameter '. Therefore, the complex permeability of the composite materials depends only on the ferrite content in this formulation. Since the ferrite content is related solely to the density of the ferrite composite materials, as we shall see, this feature supports the experimental results.

Figure 5-4 shows the complex permeability spectra calculated using equations (5. 4a), (5. 4b) and (5. 4c) for the ferrite composite materials in various values of (δ/D) . Both the real and imaginary parts of the complex permeability in the low frequency region decrease when the value of (δ/D) increases. Simultaneously, both the shoulder frequency of the real permeability and the peak frequency of the imaginary part shift toward higher frequency. In the 100MHz region, the imaginary part decreases with an increase in the value of (δ/D) , and the real permeability at $(\delta/D)=0.01$ is larger than that at different values of (δ/D) . These variations are also found in the experimental results of the ferrite composite materials, shown in Fig. 5-2. Figure 5-5 shows the variation of the dispersion parameters of the spin rotation contribution K_{sp} and ϖ_{sp} with the gap

parameter (δ/D). The open and solid circles denote K_{sp} and ω_{sp} , respectively. The K_{sp} value decreases and the resonance frequency ω_{sp} shifts toward higher frequency, when the value of (δ/D) increases. The solid lines indicate the curves calculated from equations (5. 4b) and (5. 4c) using the sintered ferrite parameters K_{sp}^B and ω_{sp}^B . A significant correlation between experimental and theoretical values is obtained. Therefore, this allows us to evaluate quantitatively the complex permeability of the ferrite composite materials in radio-frequency region using our calculation model.

Next, we consider the contribution of the domain wall motion to the complex permeability. Operating the magnetic circuit model calculation for equation (4. 32b), we obtain the following equations :

$$\chi_{dw}(\omega) = K_{dw}\omega_{dw}^2 / (\omega_{dw}^2 - \omega^2 + j\beta\omega) \quad (5. 7a)$$

$$K_{dw} = K_{dw}^B [1 + (\delta/D)] / [1 + K_{dw}^B(\delta/D)], \quad (5. 7b)$$

$$\omega_{dw} = \omega_{dw}^B [1 + K_{dw}^B(\delta/D)]^{1/2}, \quad (5. 7c)$$

where K_{dw}^B and ω_{dw}^B are the domain wall parameters for the polycrystalline sintered ferrite.

Figure 5-6 shows the domain wall contribution calculated using equations (5. 7a), (5. 7b) and (5. 7c) for the ferrite composite materials in various values of (δ/D). Both the real and imaginary parts of the domain wall permeability in the low frequency region decrease when the value of (δ/D) increases. Simultaneously, both the shoulder frequency of the real permeability and the peak frequency of the imaginary part shift toward higher frequency. These features are similar to those in the spin rotational permeability. However, since the damping coefficient for the domain wall motion β does not change with the value of (δ/D) in this formulation, the increase in the value of (δ/D) leads to the enhancement of the resonance character in high frequency region, namely, the real permeability has a small peak around the shoulder frequency, and the peak width of the imaginary part becomes narrower. The enhancement is not observed in the experimental spectra. In the real system, it is thought that the damping coefficient β

changes with the value of (δ/D) , and that the variation of β must be determined experimentally.

Figure 5-7 shows the variation of the dispersion parameters of the domain wall motion component K_{dw} and ω_{dw} with the gap parameter (δ/D) . The open and solid circles denote the experimental values of K_{dw} and ω_{dw} , respectively. The K_{dw} value decreases and the resonance frequency ω_{dw} shifts toward higher frequency, when the value of (δ/D) increases. The solid lines indicate the curves calculated from equations (5. 7b) and (5. 7c) using the sintered ferrite parameters K_{dw}^B and ω_{dw}^B . A good correlation between experimental and theoretical values is obtained. However, quantitative agreement is poorer than that in the spin rotational parameters. It is attributed to the fact that the domain wall configuration is sensitive to the demagnetizing field and that it changes with the magnetic connection. Some modifications in our model calculation are required for the quantitative evaluation in the domain wall permeability.

5.3 Extended Snoek's law

We examine the variation of the complex permeability in radio-frequency region with the ferrite content. Figure 5-8 shows the variation of the complex permeability at 50, 100, 150 and 200MHz in the ferrite composite materials with the gap parameter. The imaginary part of the complex permeability decreases when the ferrite content is reduced, however, the real permeability has a maximum at a finite value of $(\delta/D)_C$. The maximum value of the real permeability μ'_{max} decreases and the critical value $(\delta/D)_C$ increases, as the frequency is raised. For example, at 100MHz, the critical value $(\delta/D)_C$ is about 0.01 and the maximum value of μ'_{max} is approximately 40.

Using the magnetic circuit model calculation, we can expect the frequency dependence of the critical value $(\delta/D)_C$ and that of the maximum value μ'_{max} . Differentiating the real part of equation (5. 4a) with respect to the gap parameter (δ/D) and taking it to be zero at $(\delta/D)_C$, the following equation is obtained :

$$(\delta/D)_c = (1/K_{sp}^B)^2 [(\omega/\omega_{sp}^B)^2 - K_{sp}^B + (\omega/\omega_{sp}^B) \{ (K_{sp}^B)^2 + (\omega/\omega_{sp}^B)^2 \}^{1/2}] . \quad (5.8)$$

In the frequency region $(\omega/\omega_{sp}^B) \ll K_{sp}^B$, it is simplified as follows :

$$(\delta/D)_c = (1/K_{sp}^B) [(\omega/\omega_{sp}^B) - 1] . \quad (5.9)$$

Substituting the critical value $(\delta/D)_c$ into the equation (5.4a), we obtain the maximum value of μ'_{max} as,

$$\mu'_{max}(\omega) = (1/2) (K_{sp}^B \omega_{sp}^B / \omega) . \quad (5.10)$$

From these equations, it is found that the critical value $(\delta/D)_c$ increases linearly with the frequency, and that the maximum value $\mu'_{max}(\omega)$ is inversely proportional to the frequency. In addition, the maximum value $\mu'_{max}(\omega)$ is determined by the product of the static spin susceptibility K_{sp}^B and the spin resonance frequency ω_{sp}^B . This relationship corresponds to the Snoek's limit, which has been described in equation (4.21). Therefore, we consider equation (5.10) to be the Snoek's limit extended to the ferrite composite materials.

It is meaningful to compare the complex permeability evaluated by the magnetic circuit model with that estimated by the semi-empirical logarithmic law. Figure 5-9 shows the variation of the absolute value of the complex permeability with the volume loading of the ferrite particle in the composite materials. The solid line denotes the permeability change obtained by the magnetic circuit model calculation and the dashed line is obtained by the logarithmic law. Open and closed circles indicate the experimental values at 100kHz and 100MHz, respectively. The logarithmic law leads to an over-estimation of the permeability, while the magnetic circuit model calculation provides the permeability values nearly equal to the experimental values. In the ferrite composite materials, a magnetic inert (non-magnetic) component is introduced that causes not only the magnetic dilution but also a cut-off of the magnetic circuit in the magnetic materials. Consequently, the permeability is reduced remarkably as the ferrite content (volume loading) is reduced. This feature is similar to the permittivity enhancement in

metal-insulator composite materials [3, 4].

We consider that the configuration of the magnetic connection changes continuously from sintered ferrite to ferrite composite materials through the cracked ferrite. The schematic configuration changes are shown in Fig. 5-10 : (a) sintered ferrite, (b) cracked ferrite, (c) composite materials with high ferrite loading and (d) composite materials with low ferrite loading. The magnetic gaps in the sintered ferrite are negligible, so that the magnetic moment is easily aligned along an external field. In the cracked ferrite, the magnetic gaps are introduced and the magnetic poles are generated at the grain boundary between the ferrite and the magnetic inert component in the presence of an applied field. The magnetic poles create a demagnetizing field anti-parallel to the applied field. In the composite materials with high ferrite loading, some ferrite particles aggregate to form a magnetic cluster and the magnetic poles on the surface of the cluster contribute a demagnetizing field. Further, low ferrite loading composite materials have magnetic particles separated individually, and the magnetic poles on each ferrite particle generate a demagnetizing field. The demagnetizing field reduces the induced magnetization compared with that calculated from the volume loading. Therefore, the permeability in low frequency region decreases with the configuration change from the sintered ferrite to the ferrite composite materials.

It should be noted that the spin resonance frequency ω_{sp} is represented by the equation :

$$\omega_{sp} = \gamma H_a \quad (5.11)$$

where H_a is the effective anisotropy field and γ is the gyro-magnetic ratio. The effective anisotropy field is written by the summation of the magnetocrystalline anisotropy field and the shape anisotropy field. The former is mainly determined by the composition and the crystal structure of the magnetic component, and the latter depends strongly on the particle shape and the particle configuration. For the sintered ferrite, the contribution of the magnetocrystalline anisotropy field is larger than that of the shape anisotropy field,

since the magnetic gaps are negligible. In the cracked ferrite, the magnetic gaps break down the magnetic connection and the sintered ferrite is separated into finite magnetic parts with a magnetic inert component. Therefore, the shape anisotropy field is introduced, which is equivalent to a demagnetizing field H_d induced by the external magnetic field. Consequently, the spin resonance frequency is given by

$$\omega_{sp} = \gamma (H_a + H_d) . \quad (5. 12)$$

The spin resonance frequency shifts toward higher values due to the contribution of the demagnetizing field. For the ferrite composite materials, consisting of isotropic-shaped particles, there are some aggregates in the case of high volume loading composite and the particles are dispersed individually in the case of low ferrite loading. Since the cluster of the magnetic particles behaves as a magnetic unit, the number of magnetic poles per unit volume is less than that for the isolated particles. Thus, the demagnetizing field increases with a decrease in the ferrite loading, and the spin resonance frequency becomes higher. As a result, the real part of the complex permeability can take a larger value than that of the sintered ferrite in the radio-frequency region. That is, the magnetic circuit model includes the demagnetizing effect in the ferrite composite materials, and the demagnetizing effect is reflected in the extended Snoek's limit (5. 10).

5. 4 Temperature variation of permeability spectra

In order to measure the complex permeability at the temperature range from 100 to 400K, we have prepared the ferrite composite materials using PPS (poly-phenylene sulfide) resin, by mixing the ferrite particles (the particle size being less than 100 μ m) with appropriate amounts of PPS resin and pressing the mixture into a ring form at 300 $^{\circ}$ C, followed by slow cooling.

Figure 5-11 shows the complex permeability spectra of Ni-Zn sintered ferrite at the temperature range from 100 to 400K. It is found that, with an increase in temperature, the real permeability increases and its shoulder frequency shifts toward

lower values. The imaginary part of the complex permeability also increases and its peak frequency shifts toward lower values when the temperature is raised. The variation of the complex permeability spectra with temperature is drastic in the sintered ferrite : the real permeability at low frequency region is approximately 100 and 1400 at 100 and 360K, respectively. The temperature variation of the complex permeability spectra for the ferrite composite material with the ferrite loading of 70vol% is shown in Fig. 5-12. The real permeability increases only slightly with an increase in temperature and the peak frequency of the imaginary part slightly shifts toward lower frequency. These indicate that the temperature dependence of the complex permeability spectra becomes smaller in the ferrite composite materials.

Temperature variation of the real permeability in various frequencies is shown in Fig. 5-13 for the sintered ferrite and the composite material with the ferrite loading of 70vol%. For the sintered ferrite, large peaks of the real permeability in low frequency region (from 100kHz to 1MHz) can be observed just below the Curie temperature of 380K. These peaks are attributed to the difference of the temperature dependence between the saturation magnetization and the magnetic anisotropy in the sintered ferrite. For polycrystalline ferrite, intrinsic spin rotational susceptibility and domain wall susceptibility are written as :

$$\chi_{sp} = 2\pi M_s^2 / K_u \quad (5.13a)$$

$$\chi_{dw} = 3\pi M_s^2 D / 4\gamma \quad (5.13b)$$

with M_s the saturation magnetization, K_u the total magnetic anisotropy energy, D the grain diameter and γ the domain wall energy. Since the magnetic anisotropy field H_a is described as $H_a = 2K_u / M_s$, the spin rotational susceptibility can be represented by

$$\chi_{sp} = 4\pi M_s / H_a \quad (5.14)$$

The decrease in H_a is larger than that of M_s near the Curie temperature, hence the spin rotational susceptibility increases with an increase in temperature just below the Curie temperature and has a maximum around the Curie temperature. In addition, the domain

wall susceptibility has no anomaly near the Curie temperature. In other word, χ_{dw} decreases monotonically with an increase in temperature.

In the ferrite composite materials, the demagnetizing field H_d is added to the anisotropy field and χ_{sp} can be re-written as

$$\chi_{sp} = 4\pi M_s / (H_a + H_d) . \quad (5. 15)$$

Since the magnetic anisotropy field may not be so large ($H_a \ll H_d$) for Ni-Zn ferrite, the spin rotational susceptibility of the composite materials is considered to be determined mainly by the demagnetizing field. Thus, the spin rotational susceptibility is given by

$$\chi_{sp} = 4\pi M_s / H_d . \quad (5. 16)$$

The demagnetizing field H_d is proportional to the magnetization of the embedded ferrite particles. Consequently, the spin rotational susceptibility becomes almost independent of the temperature. Figure 5-14 indicates the temperature variation of the static spin susceptibility K_{sp} , which is determined by numerical fitting of the measured permeability spectra with equation (5. 4a). It clearly indicates these features.

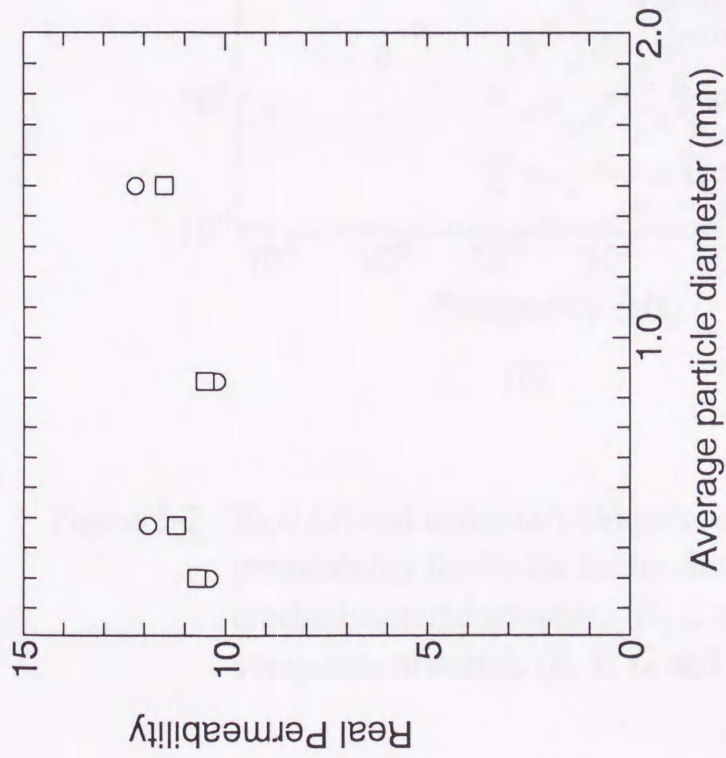
Figure 5-15 shows the variation of the spin resonance frequency ω_{sp} , which is also obtained by the numerical fitting mentioned above, with temperature for the sintered ferrite and the ferrite composite material. For the sintered ferrite, the spin resonance frequency drastically shifts toward lower values with an increase in the temperature. However, the temperature variation of the spin resonance frequency ω_{sp} is comparatively small in the ferrite composite material. The spin resonance frequency in the sintered ferrite is given by equation (5. 11), where the anisotropy field H_a decreases with an increase in temperature, and therefore, the spin resonance frequency shifts toward lower frequency as the temperature is raised. On the other hand, the spin resonance frequency in the ferrite composite materials is represented by equation (5. 12). Considering the experimental facts that the anisotropy field is much smaller than the demagnetizing field and that the demagnetizing field is proportional to the magnetization of the embedded ferrite particles, we infer that the temperature dependence of the spin

resonance frequency is determined by that of the magnetization of the embedded ferrite particles. Since the variation of the magnetization with temperature is small compared to that of the magnetic anisotropy field, the temperature variation of the spin resonance frequency in the ferrite composite materials becomes small.

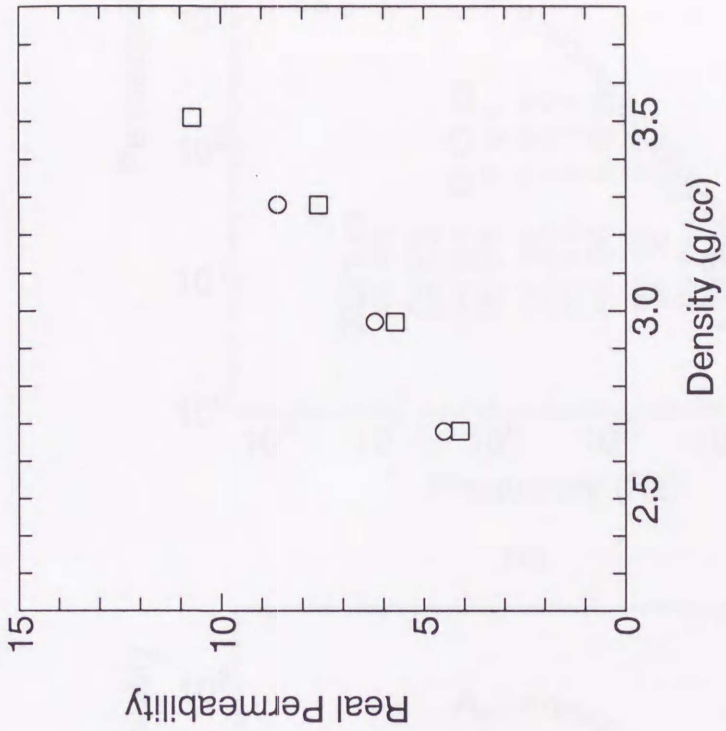
It should be noted that, from equations (5. 12) and (5. 16), we obtain the following relation.

$$\chi_{sp} \omega_{sp} = 4\pi\gamma M_S . \quad (5. 17)$$

This formula represents the Snoek's law. Therefore, Snoek's relation is conserved in the temperature variation of the complex permeability spectra as well as the ferrite content variation in the ferrite composite materials.

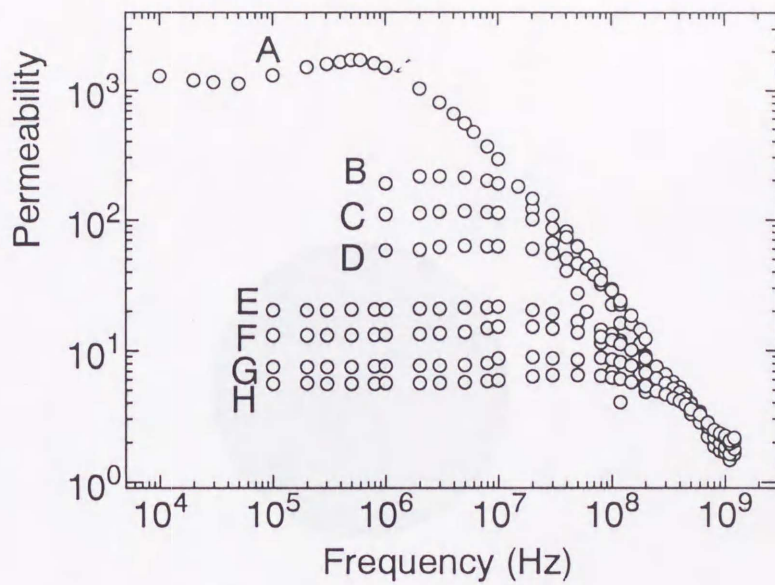


(a)

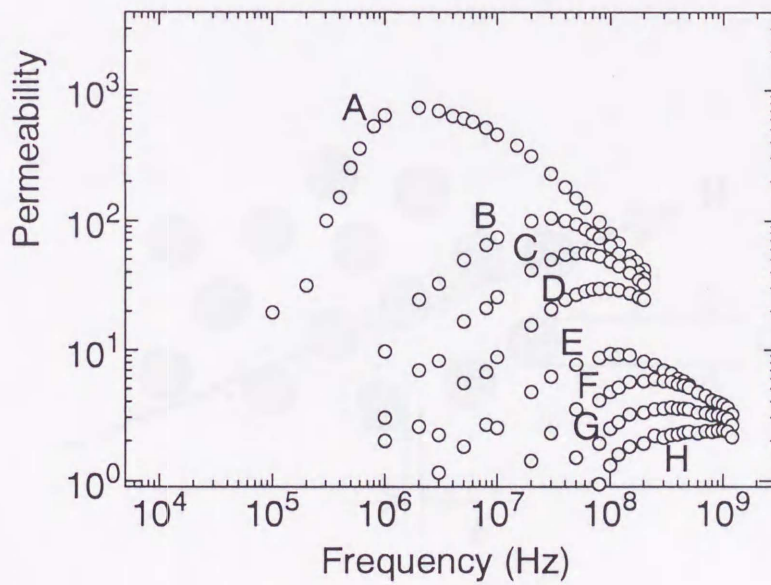


(b)

Figure 5-1 : Variation of the real part of complex permeability with the average particle diameter (a), and the variation of the real permeability with the density of the composite materials (b) (○ 100kHz and □ 100MHz).

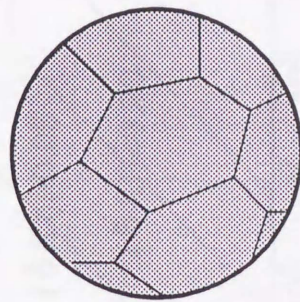


(a)

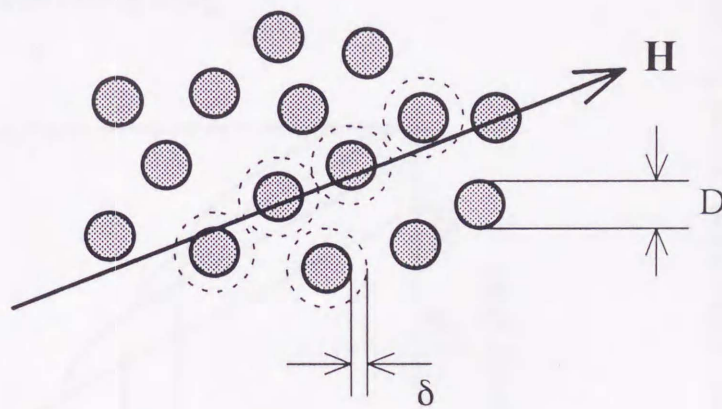


(b)

Figure 5-2 : Real (a) and imaginary (b) parts of the complex permeability for Ni-Zn ferrite sintered ceramics (A), cracked sintered ceramics (B, C and D) and ferrite composite materials (E, F, G and H).

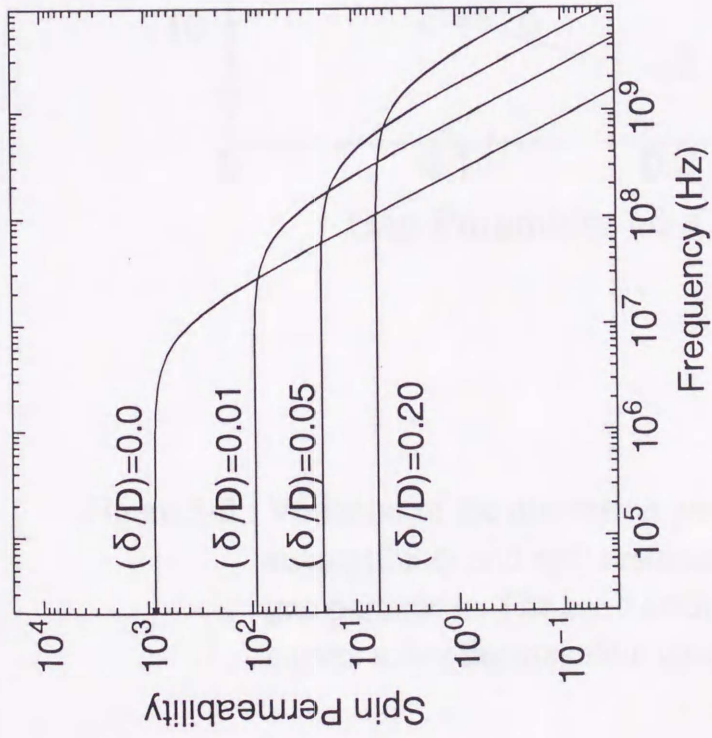


(a)

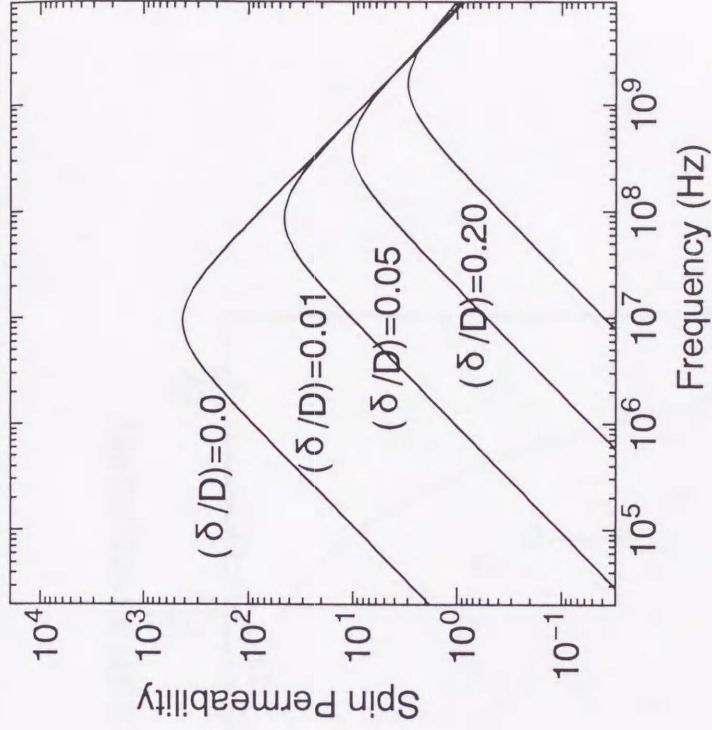


(b)

Figure 5-3 : The schematic configuration of the ferrite composite materials. (a) Intra-particle structure and (b) inter-particle arrangement.



(a)



(b)

Figure 5-4 : Frequency dispersion curves for the spin rotational permeability calculated using the magnetic circuit model at various gap parameter values ((a) real and (b) imaginary parts).

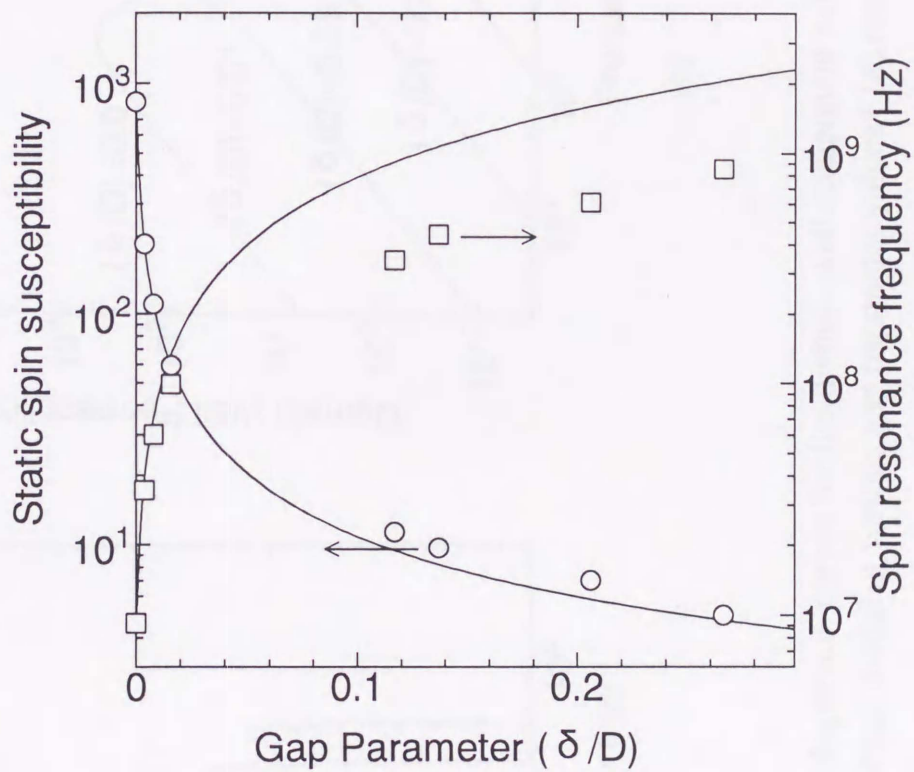


Figure 5-5 : Variation of the dispersion parameters (static spin susceptibility and spin resonance frequency) with the gap parameter. The solid lines denote the calculated curves using the magnetic circuit model.

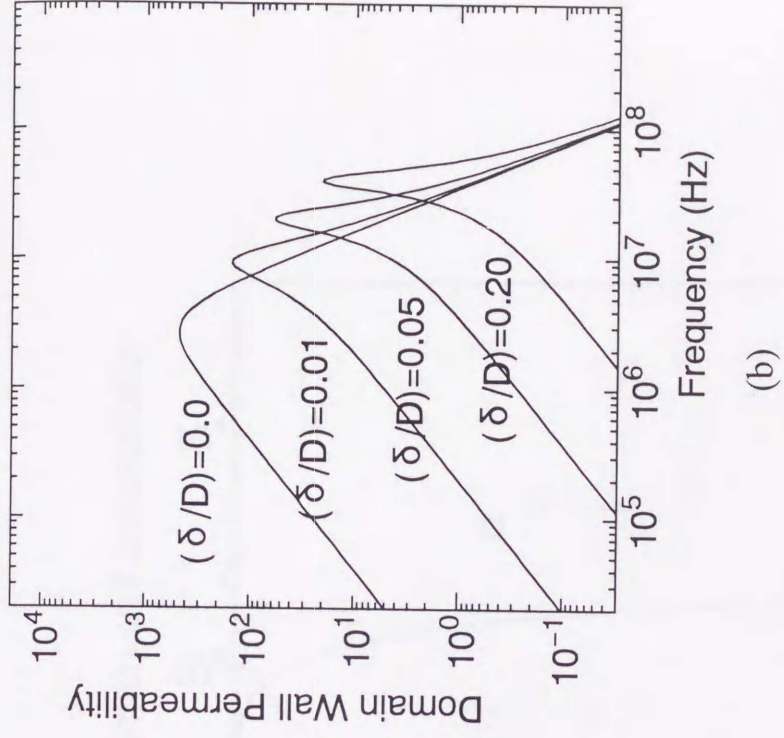
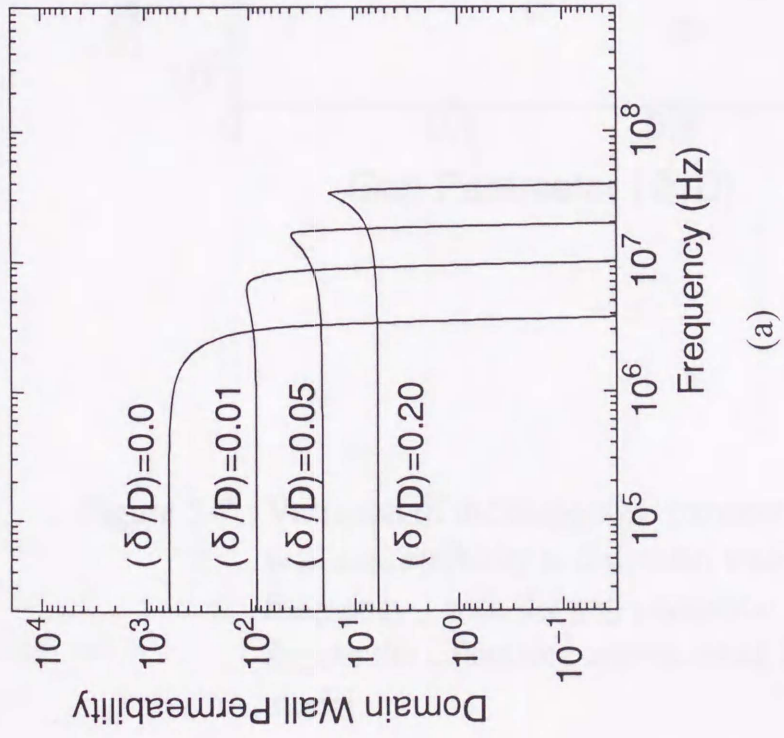


Figure 5-6 : Frequency dispersion curves for the domain wall component calculated using the magnetic circuit model at various gap parameter values ((a) real and (b) imaginary parts).

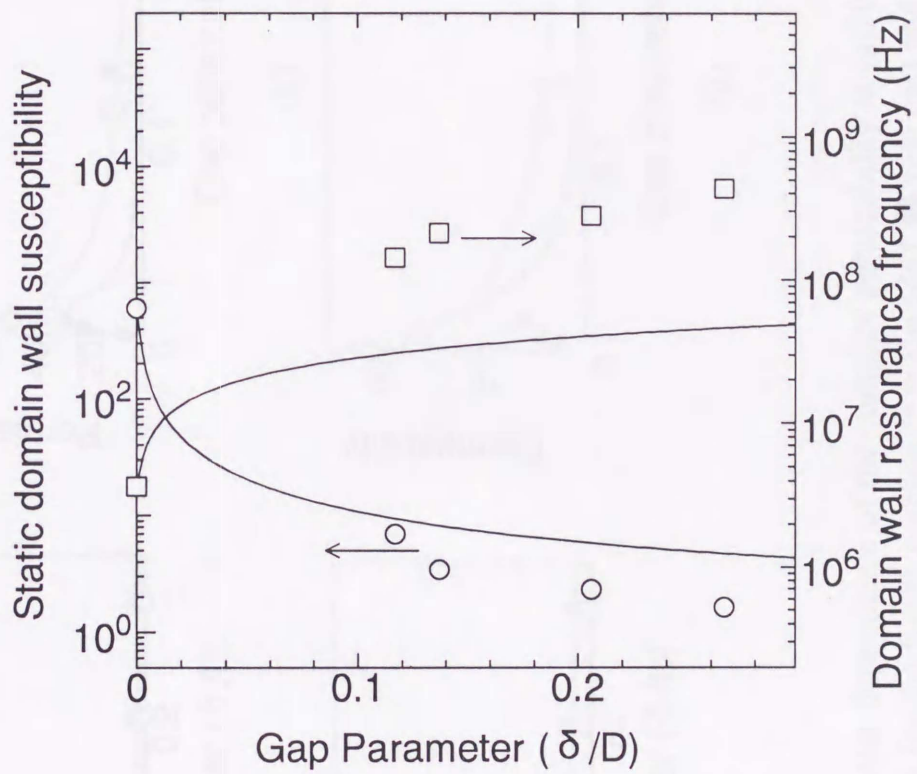


Figure 5-7 : Variation of the dispersion parameters (static domain wall susceptibility and domain wall resonance frequency) with the gap parameter. The solid lines denote the calculated curves using the magnetic circuit model.

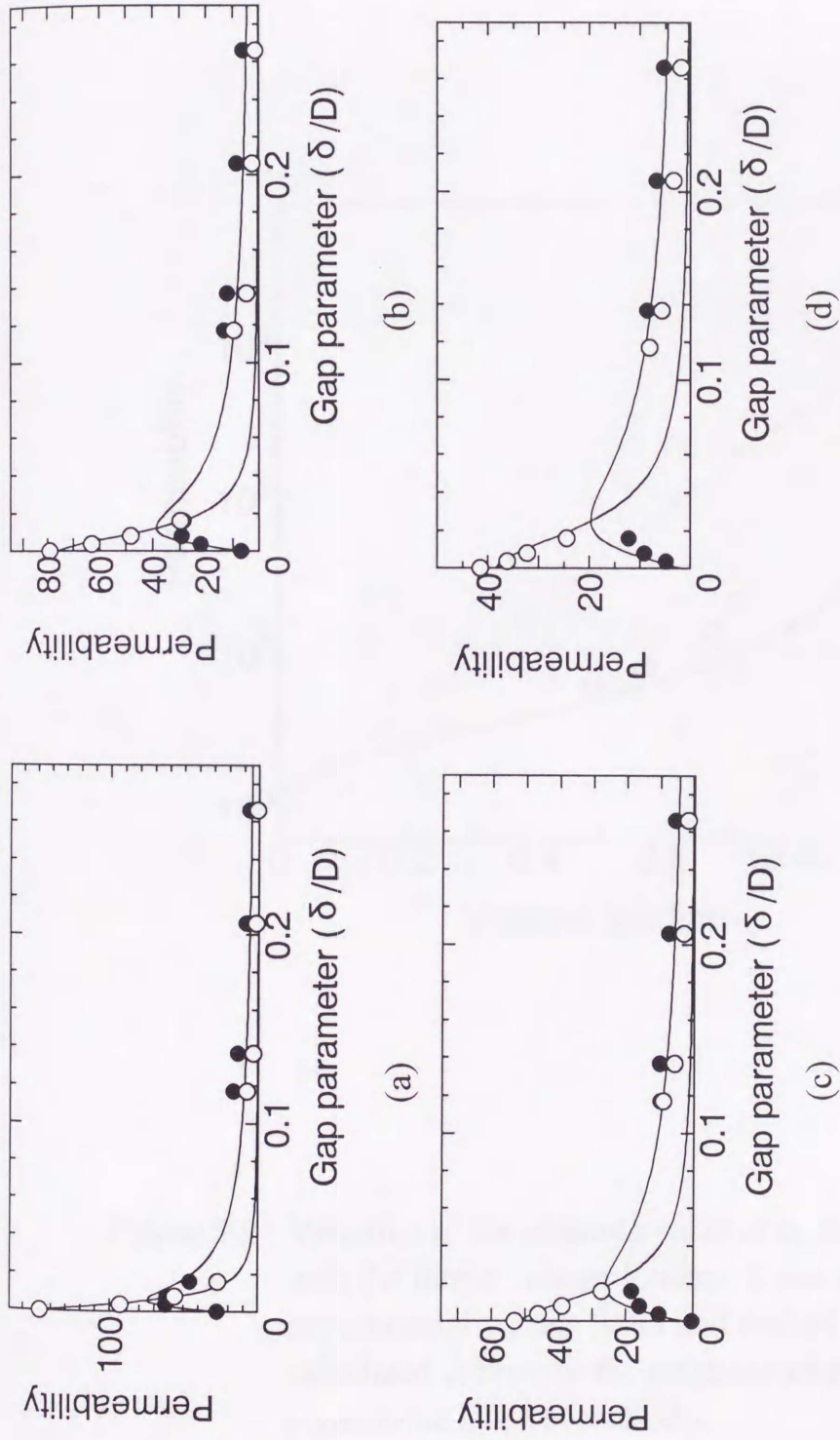


Figure 5-8 : Gap parameter dependence of the complex permeability at (a)50, (b)100, (c)150 and (d)200MHz for the ferrite composite materials (● real part and ○ imaginary part). The solid lines denote the calculated curves using the magnetic circuit model.

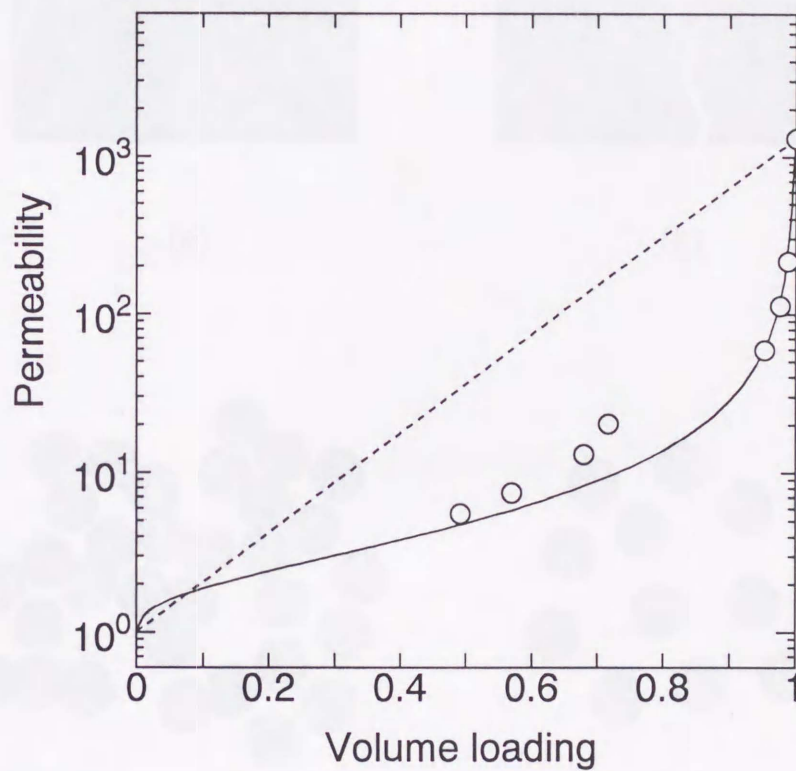
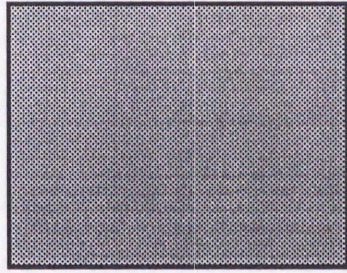
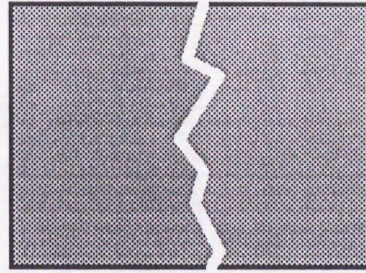


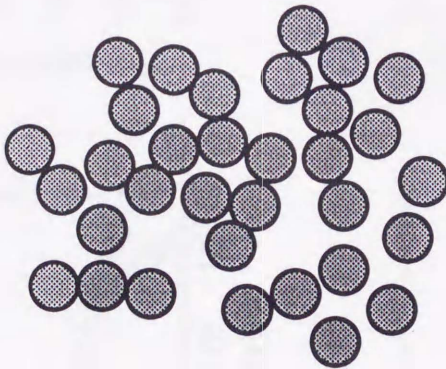
Figure 5-9 : Variation of the absolute value of complex permeability with the ferrite volume loading. Open circles denote experimental values. Solid and dashed lines indicate the calculated curves for the magnetic circuit model and the logarithmic law, respectively.



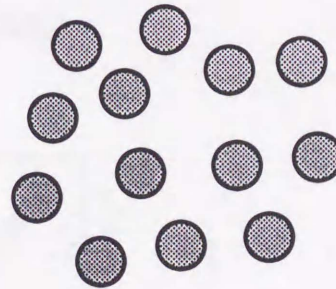
(a)



(b)

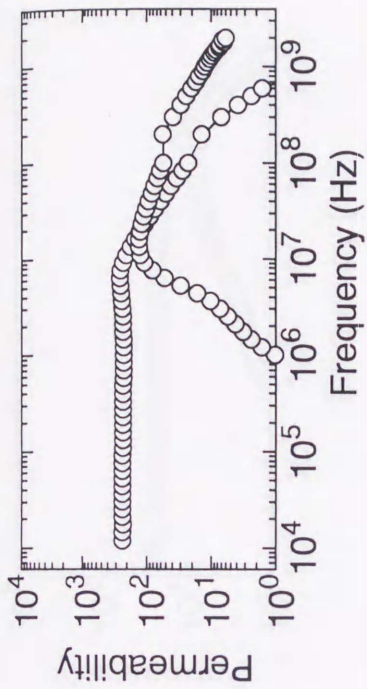


(c)

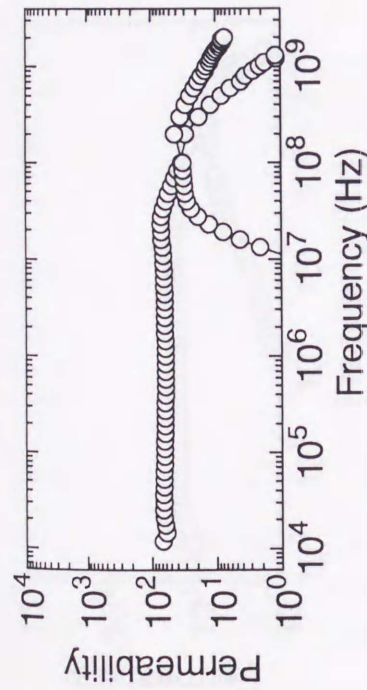


(d)

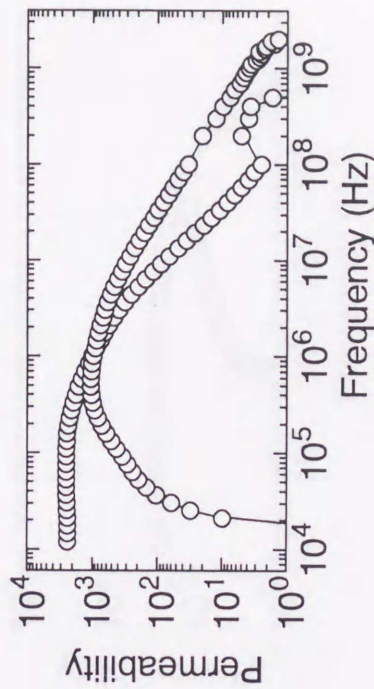
Figure 5-10 : Schematic configurations of magnetic connection.
(a) sintered ferrite ceramics, (b) cracked ferrite ceramics, (c) composite material with high ferrite loading and (d) that with low ferrite loading.



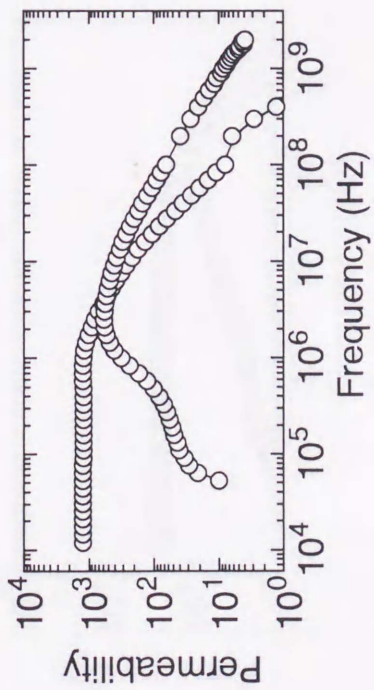
(a)



(b)

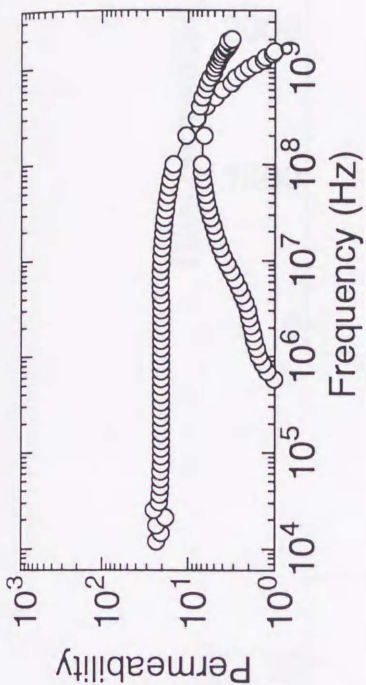


(c)

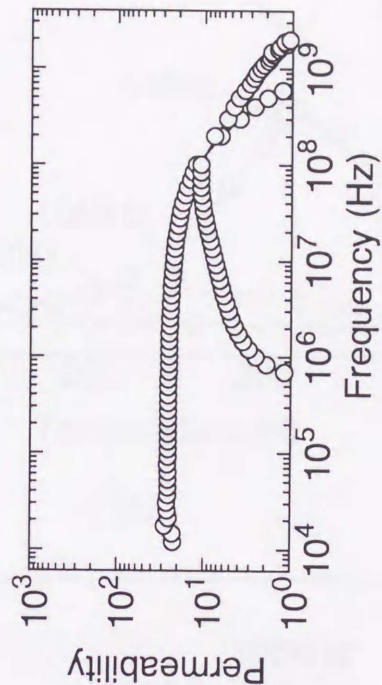


(d)

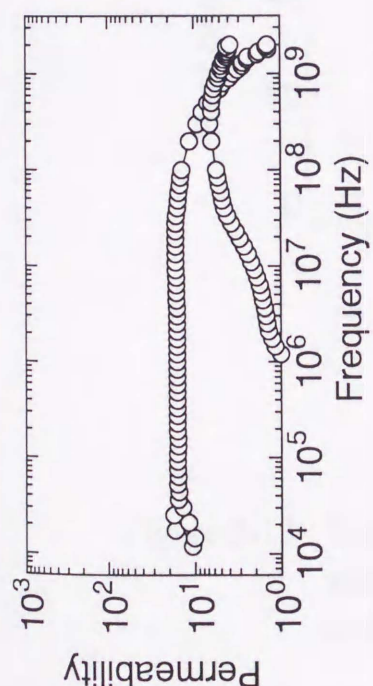
Figure 5-11 : Complex permeability spectra of the sintered ferrite at (a) 100, (b) 200, (c) 300 and (d) 360K.



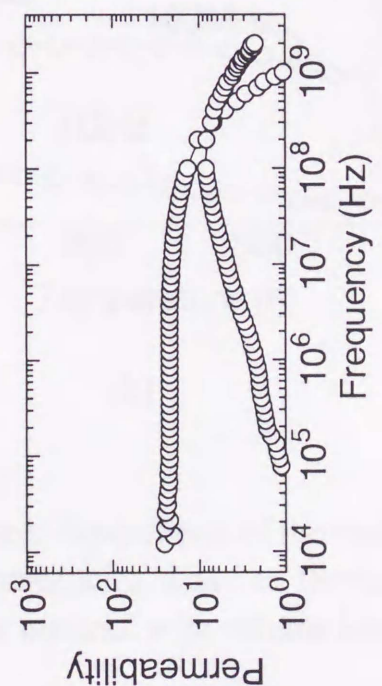
(b)



(d)

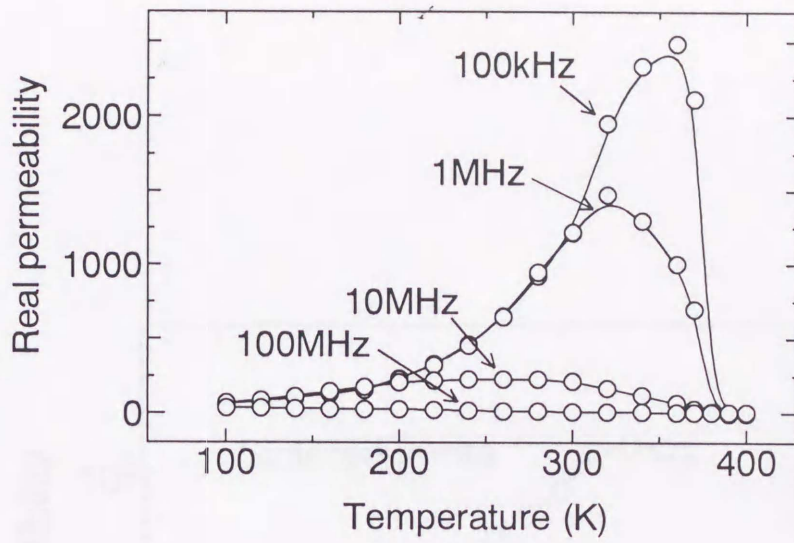


(a)

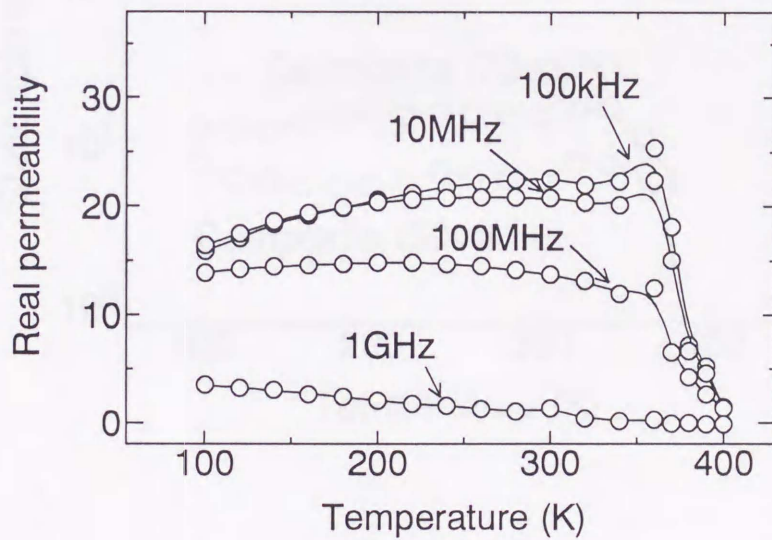


(c)

Figure 5-12 : Complex permeability spectra of the ferrite composite material with ferrite volume loading of 70% at (a) 100, (b) 200, (c) 300 and (d) 360K.



(a)



(b)

Figure 5-13 : Temperature dependence of the real permeability in various frequencies. Sintered ferrite (a) and ferrite composite material with volume loading of 70% (b).

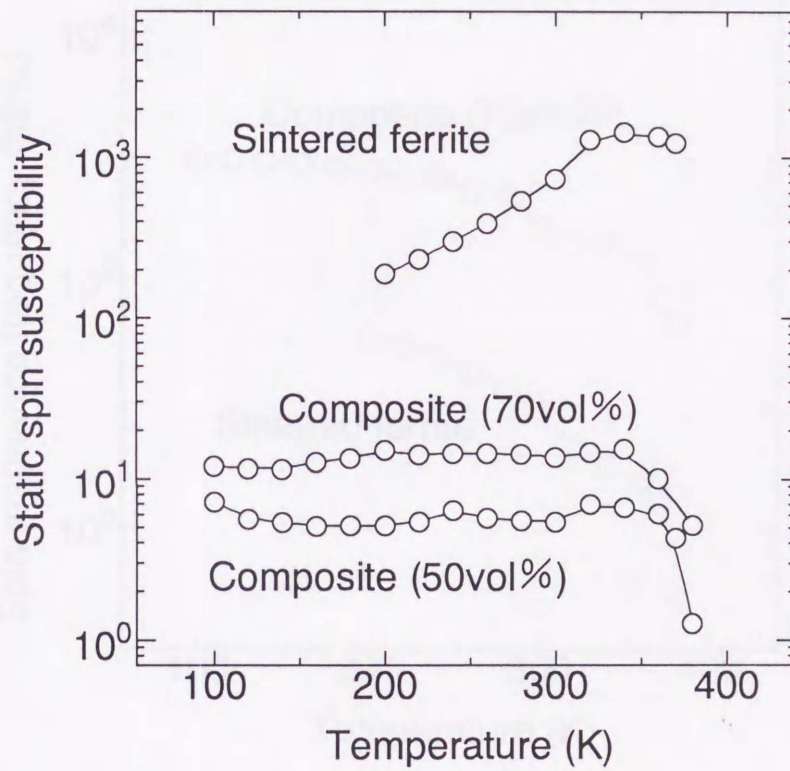


Figure 5-14 : Temperature variation of the static spin susceptibility for sintered ferrite and ferrite composite materials with volume loading of 50 and 70%.

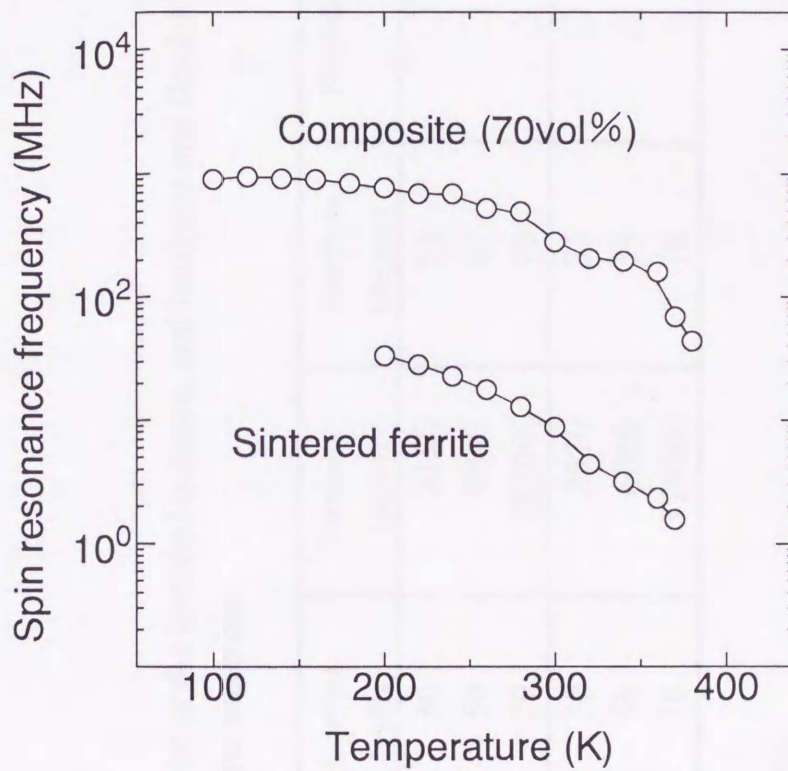


Figure 5-15 : Temperature variation of the spin resonance frequency for sintered ferrite and ferrite composite material with volume loading of 70%.

Table 5-1 : Viscosity of the kneaded mixture, and hardness and flexibility of the composite materials.

Particle diameter (μm)	Content (vol%)	Viscosity (poise)	Hardness* (degree)	Flexibility**
<7.4	30	3180	52	○
<7.4	50	9820	61	○
<7.4	70	283000	70	△
>85	30	2570	52	○
>85	50	6060	59	△
>85	70	129000	78	×

* "D" degree,

** ○ : Good, △ : Intermediate, × : Poor.

Chapter 6

Complex permeability in low-temperature sintered Ni-Zn-Cu ferrite

Recently, the surface mounting devices have been rapidly developed using a multilayer chip inductor[1]. The concept of the chip inductor is based on the enhancement of the quality factor with decrease in the size. In general, the potential of the inductor is characterized by the inductance (L), the resistance (R), and the ratio of L/R corresponding to the quality factor (Q). Considering the toroidal core of the magnet (a, b and r are the thickness, the width and the radius of the toroidal core, respectively) in Fig. 6-1, we can write the inductance, the resistance and the quality factor as,

$$L_B = ab\mu N^2 / 2\pi r, \quad (6.1a)$$

$$R_B = \rho(a+b)N / (\pi r/N)^2, \quad (6.1b)$$

$$Q_B = ab\mu N (\pi r/N)^2 / 2\pi r \rho(a+b) \quad (6.1c)$$

with N being the turn number of the coil, μ the permeability of the magnet and ρ the resistivity of the coil. For simplicity, the contribution from the imaginary part of the permeability has been neglected. The chip inductor is of layered-type, and the thickness a is replaced by δ ($\delta \ll b, r$).

$$L_C = \delta b \mu N^2 / 2\pi r, \quad (6.2a)$$

$$R_C = \rho(\delta+b)N / (\pi r/N)^2, \quad (6.2b)$$

$$Q_C = \delta b \mu N (\pi r/N)^2 / 2\pi r \rho(\delta+b) . \quad (6.2c)$$

The chip inductor is quite different from the small-size bulk inductor, and the difference

is obvious when the size dependence of L , R and Q is considered. The size of the bulk inductor varies in three-dimensional way. Assuming that the scaling factor is K , we find from the set of equations (6.1), that L_B increases linearly with K , R_B is inversely proportional to K and Q_B is proportional to the square of K . These are shown in Fig. 6-2(a). On the other hand, the chip inductor behaves two-dimensionally, so that L_C , R_C and Q_C are independent of K (see Fig. 6-2(b)). The quality factor in the bulk inductor remarkably decreases with decrease in the size, but that of the chip inductor does not vary with the size. Therefore, the chip inductor device is suitable for the size reduction in the electronic parts.

This chip inductor is produced by coating ferrite and electrical pastes alternately and by co-firing. Since Ag is usually used as the electrode material, high temperature co-firing causes unexpected lowering of the inductance due to the interfacial reaction (diffusion) between the ferrite and the Ag electrode. The interfacial reaction can be suppressed by co-firing at a temperature lower than the melting point of Ag (960°C). Therefore, low temperature sintering of ferrite is strongly demanded.

Here, the low temperature sintering of Ni-Zn-Cu ferrite has been studied and the relations between preparation conditions (calcination temperature, particle size of starting materials) and some properties of the sintered ferrite (sintering density, permeability) have been investigated. In addition, the permeability variation with the preparation conditions is discussed from the view point of the spin and domain wall contributions.

Different size of Fe_2O_3 , NiO and ZnO particles are used for the preparation of Ni-Zn-Cu ferrite sintered ceramics; calcination and sintering temperature are changed to find the optimum condition for low temperature ferrite sintering. The set of the starting materials to prepare Ni-Zn-Cu ferrite sintered ceramics are listed in Table 6-1. $\alpha\text{-Fe}_2\text{O}_3$ coarse particles (the average diameter of $0.15\mu\text{m}$) were synthesized by the oxidation of Fe_3O_4 particles at 800°C . The Fe_3O_4 particles were precipitated by aerial oxidation of

alkaline $\text{Fe}(\text{OH})_2$ suspension at 80°C . $\gamma\text{-Fe}_2\text{O}_3$ fine particles (the average diameter of $0.03\mu\text{m}$) were prepared by thermal decomposition of ferrous oxalate at 400°C in air. The ferrous oxalate particles were precipitated by mixing of ferrous sulfate and oxalic acid aqueous solutions at 50°C . Industrial grade particles of Ni oxide (Sumitomo Metal&Mine), Zn oxide (Seido Chemical) and Cu oxide (Nikko Fine Chemical) were used as the coarse particles (their average diameters were 0.5, 0.18 and $0.4\mu\text{m}$, respectively). Fine particles of Ni oxide and Zn oxide were also synthesized by thermal decomposition of Ni - and Zn-oxalate at 400°C in air, the average diameter of which were 0.04 and $0.02\mu\text{m}$, respectively.

Ni-Zn-Cu ferrite ceramics were synthesized by usual ceramic technique (double sintering method). Starting powders Fe_2O_3 , NiO, ZnO and CuO were mixed together with wet attrition milling. Their molar ratio was adjusted to the composition of $\text{Ni}_{0.26}\text{Zn}_{0.52}\text{Cu}_{0.25}\text{Fe}_{1.97}\text{O}_4$. The mixtures were calcined in air at several temperatures ranging from 750 to 850°C for four hours, and re-ground by wet ball milling. The obtained ferrite powders were mixed with appropriate amount of poly-vinyl-alcohol as a binder, subjected to the press compacting (plate with the diameter of 50mm and the thickness of about 5mm) and sintered in air at temperature range from 850 to 920°C for four hours.

The density of the sintered plate was calculated by measuring the dimensions and the weights. In order to measure the permeability, the sintered ferrites were cut into rings, the outer and inner diameters of which were 38 and 17mm, respectively. Their permeabilities in the frequency region from 1MHz to 1GHz were obtained by measuring the input impedance of the samples using the coaxial line technique with the RF network analyzer (Hewlett Packard HP-8753C). The scanning electron microscopic observation (with HITACHI S-800) was also carried out in order to investigate the microstructure of the sintered ferrite.

6.1 Sintering ability and permeability

First, the calcination temperature was fixed at 800 °C in order to examine the effects of the starting materials. The variation of the sintering density and the permeability at 10MHz with the sintering temperature are shown in Fig.6-3(a) and (b) for each set of the starting materials. From these figures, both the sintering density and the permeability increase with an increase of the sintering temperature for each set. It is found that using the fine particles as the starting materials leads to a greater sintering density and a greater permeability at the same sintering temperature. Especially, use of fine iron oxide particles is most effective to obtain the sintered ferrite with high sintering density and high permeability. Small starting oxide particles are transformed into smaller ferrite particles during the calcination process. These smaller ferrite particles have larger surface area and larger free energy. Since the surface free energy is considered to be a driving force in the sintering process, the smaller ferrite particles tend to be well sintered. Therefore, the use of fine oxide particles as the starting materials is effective in preparing high density sintered ferrite through low temperature sintering .

Next, the starting materials and the sintering temperature were fixed and then the effect of the calcination temperature was examined. Figure 6-4(a) and (b) show the variation of the sintering density and the permeability at 10MHz versus the calcination temperature. According to Fig.6-4(a), the sintering density remains almost constant at the calcination temperature below 800 °C , and it decreases when the calcination temperature exceeds 800 °C. The particle size of the calcined ferrite increases when the calcination temperature is raised. Accordingly, large thermal energy is required to sinter the particles, low temperature sintering being considered to be difficult. On the other hand, the permeability takes a maximum value at about 800 °C of the calcination temperature. These results indicate that there exists an optimum calcination temperature to obtain high permeability ferrite ceramics.

From these results, both the utilization of the fine iron oxide particles as the

starting materials and the appropriate temperature calcination produce the sintered ferrite with high density and high permeability. Figure 6-5 shows the frequency dispersion of the complex permeability for the sintered ferrite which was synthesized by use of γ -Fe₂O₃, calcination at 800°C and sintering at 900°C. It has the sintering density of about 4.6g/cc and the real part of the permeability is about 200 at 10MHz and approximately 30 at 100MHz.

6.2 Permeability variation

The preparation conditions have an effect on the permeability in the sintered ferrite. In order to clarify the factor affecting the permeability, the relationship between the sintering density and the permeability is examined as in the case of the ferrite composite materials (in chapter 5). The permeability variation with the sintering density is shown in Fig. 6-6. The open and solid circles denote the real part of the permeability at 10 and 100MHz, respectively. In general, the permeability is related to two different magnetizing mechanisms : the spin rotational magnetizing and the domain wall motion. It is known that the complex permeability of sintered ferrite in 100MHz region is almost determined by the spin rotation magnetizing mechanism[2] and that the spin rotational component of the permeability depends only on the ferrite volume loading, i.e. the sintering density. Therefore, the permeability in 100MHz region can be controlled by the sintering density. It increases with a increase of the sintering density and saturates at about 4.5g/cc. Roughly speaking, the permeability at 10MHz also has the same trend and increases with the sintering density. However, the permeability values at 10MHz are spread over a wide range owing to the difference in the conditions. Indeed, there are highly sintered ferrite ceramics with low permeability. While, in 100MHz region, the permeability can be described only by the spin rotational component, the contribution of the domain wall motion is not negligible in 10MHz region and the domain wall contribution cannot be represented only by the sintering density.

For detailed discussions, the permeability spectra of the sintered specimen have been decomposed into the spin rotation component ($\chi_{sp}(\omega)$) and the domain wall component ($\chi_{dw}(\omega)$) using the inverse cole-cole plot technique (see chapter 4).

$$\mu(\omega) = 1 + \chi_{sp}(\omega) + \chi_{dw}(\omega) \quad (6. 3)$$

and

$$\chi_{sp}(\omega) = K_{sp} / [1 + j(\omega/\omega_{sp})] \quad (6. 4a)$$

$$\chi_{dw}(\omega) = K_{dw}\omega_{dw}^2 / [\omega_{dw}^2 - \omega^2 + j\beta\omega] . \quad (6. 4b)$$

Figure 6-7(a) shows the variation of the static spin susceptibility (K_{sp}) with the sintering density. From this figure, we can see that the spin contribution is practically determined by the sintering density. This behavior is similar to that in the ferrite composite materials. For the ferrite composite materials (in chapter 5), we can make a simple relation between the density and the gap parameter (δ/D). However, in the low-temperature sintered ceramics, we have failed quantitative evaluation of the complex permeability using such a simple relation. It is attributed to the facts that the sintered structure is not well characterized only by the average values of δ and D , and that the distribution of δ and D has an significant role.

The variation of the domain wall contribution (K_{dw}) versus the sintering density is shown in Fig. 6-7(b). The domain wall contribution cannot be described only by the sintering density and it is spread over a wide range owing to the difference of other factors. Globus suggested that the domain wall motion was affected by the grain size and enhanced with the increase of the grain size[3]. It is attributed to the domain configuration change with the grain size. Informations about the ferrite grain size have been obtained from the microstructural observation of the specimen. Figure 6-8 shows the SEM photographs for the fracture surface of two different ferrites which have almost the same sintering density (about 4.35g/cc) and almost the same spin contribution (about 105) but have different grain size. The static susceptibility of the domain wall motion of sample (a) and (b) are 30 and 70, respectively. It is seen that the grain size of

the sample (a) is larger than that of the sample (b) ; the average grain size which is estimated from the geometric analysis is $0.7\mu\text{m}$ for the sample (a) and $1.5\mu\text{m}$ for the sample (b). This indicates that the ferrite grain size has a great influence on the domain wall contribution. The result shows that it is necessary to increase the sintering density and the ferrite grain size for large domain wall susceptibility. Although low temperature calcination produces small ferrite particles which have an easy sintering ability even at relative low temperatures, resulting in the ferrite ceramics with high sintering density, the grain growth of the ferrite particles is not sufficient. This is a reason why there exists the optimum calcination temperature for high permeability ferrite ceramics.

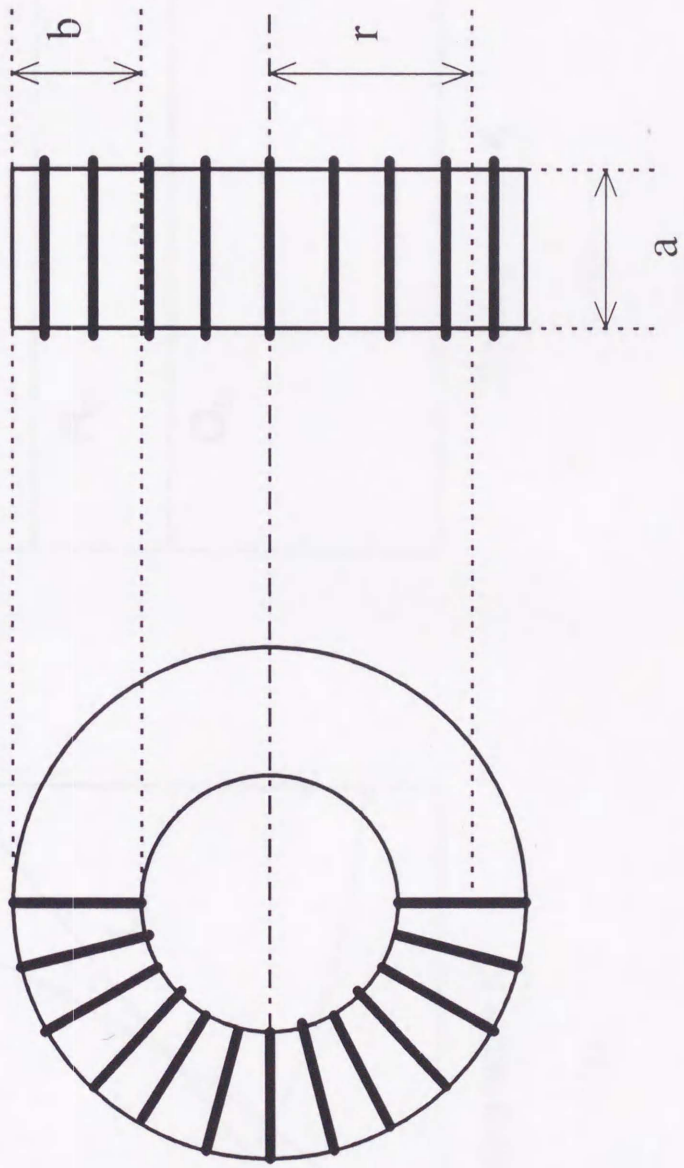
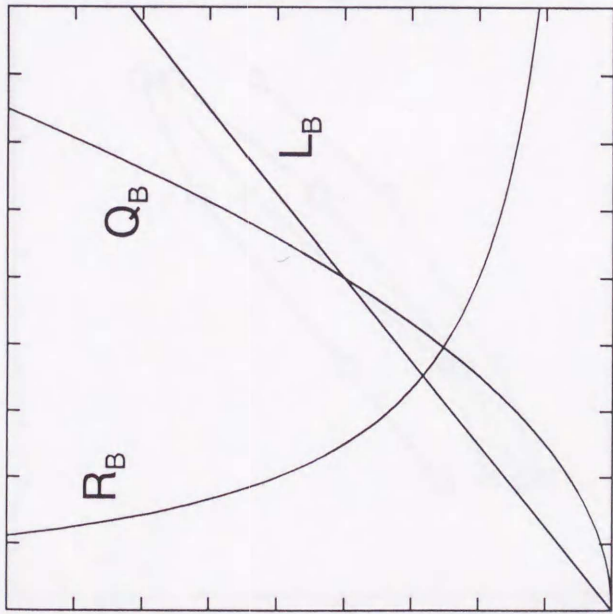
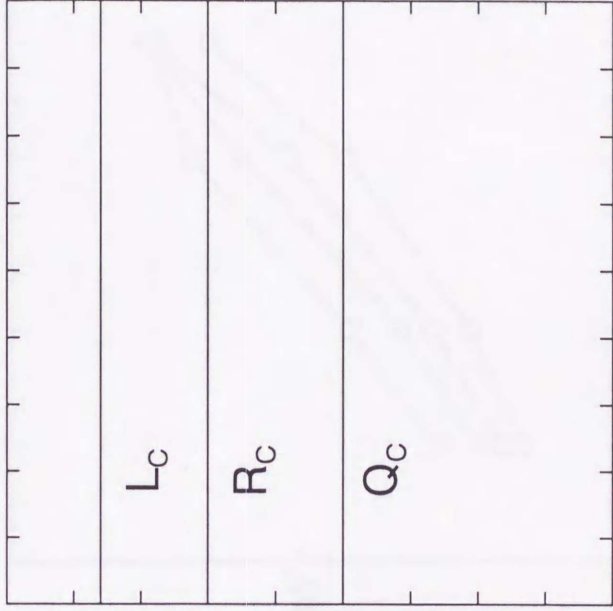


Figure 6-1 : Toroidal core of the magnet. a , b and r are the thickness, the width and the radius of the toroidal core, respectively.



Scaling factor K

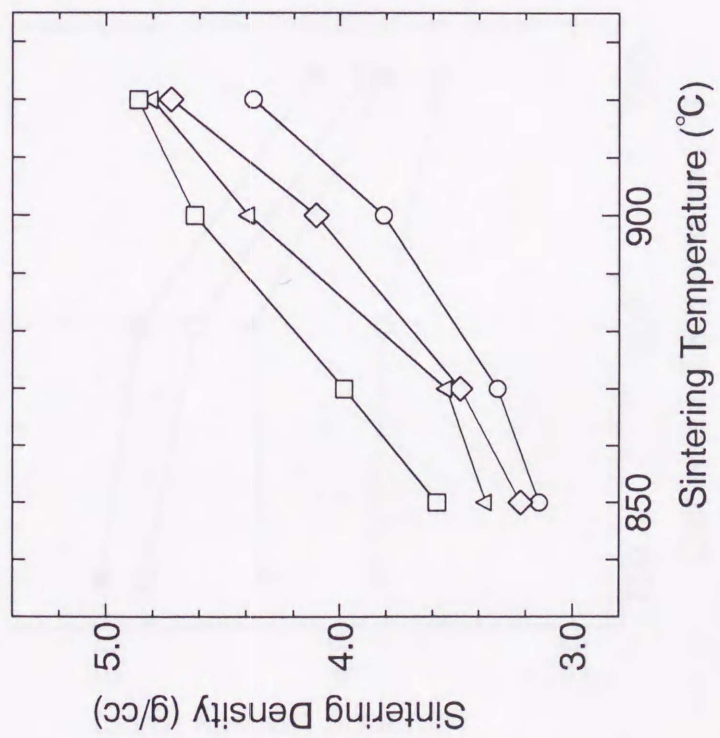
(a)



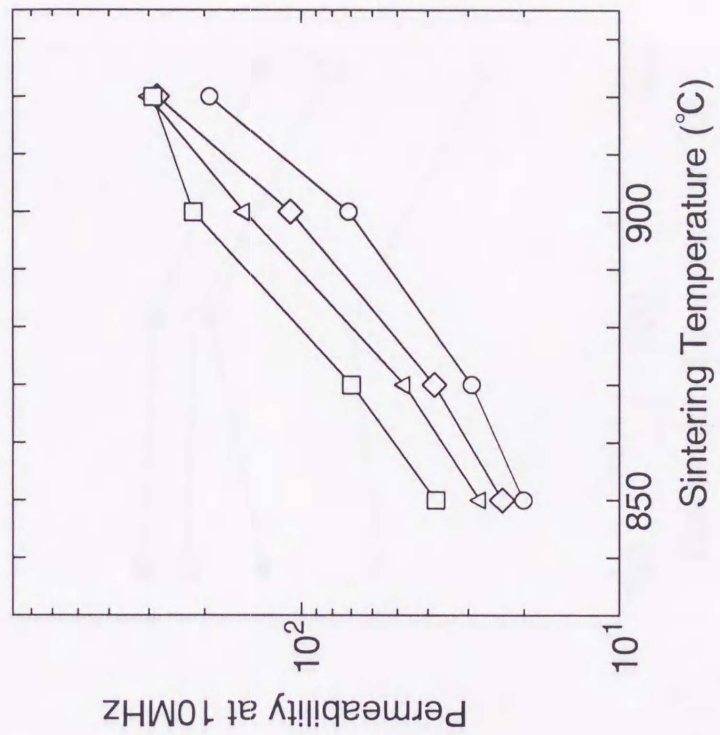
Scaling factor K

(b)

Figure 6-2 : Size dependence of inductance (L), resistivity (R) and quality factor (Q).
 (a) Bulk inductor and (b) Chip inductor.

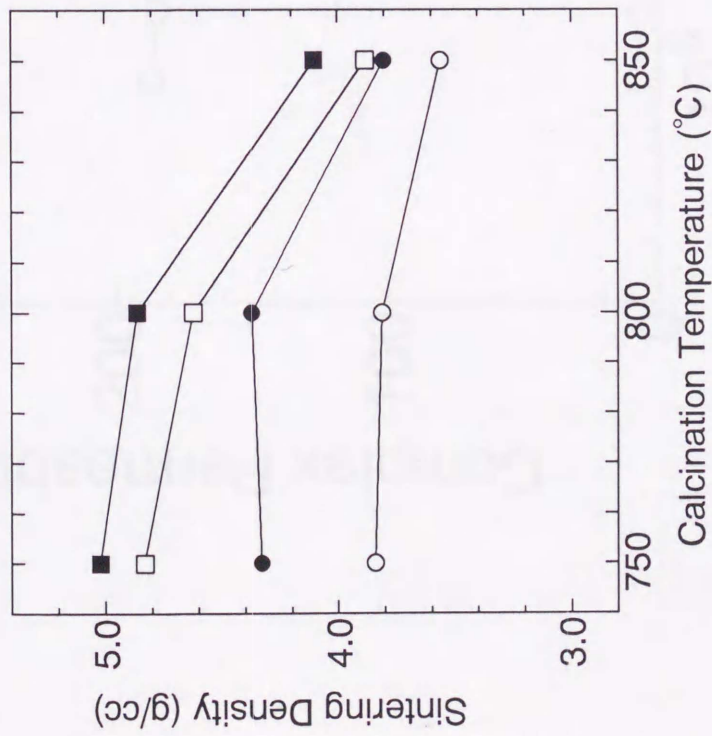


(a)

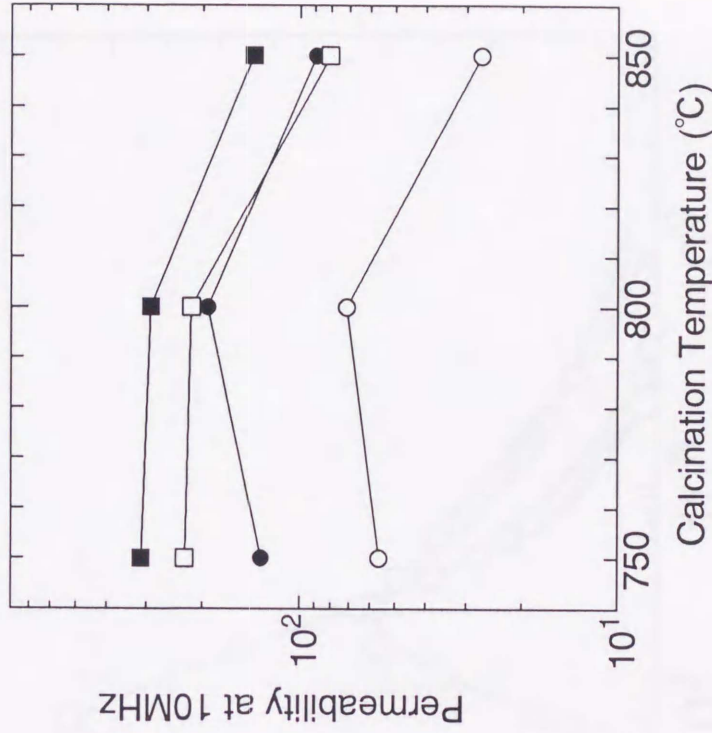


(b)

Figure 6-3 : Variation of the sintering density (a) and the permeability at 10MHz (b) with the sintering temperature, using starting powders of A(○), B(◇), C(△) and D(□).



(a)



(b)

Figure 6-4 : The sintering density (a) and the permeability at 10MHz (b) versus the calcination temperature. Starting powders A and the sintering temperature at 900°C (○) or 920°C (●). Starting powders D and the sintering temperature at 900°C (□) or 920°C (■).

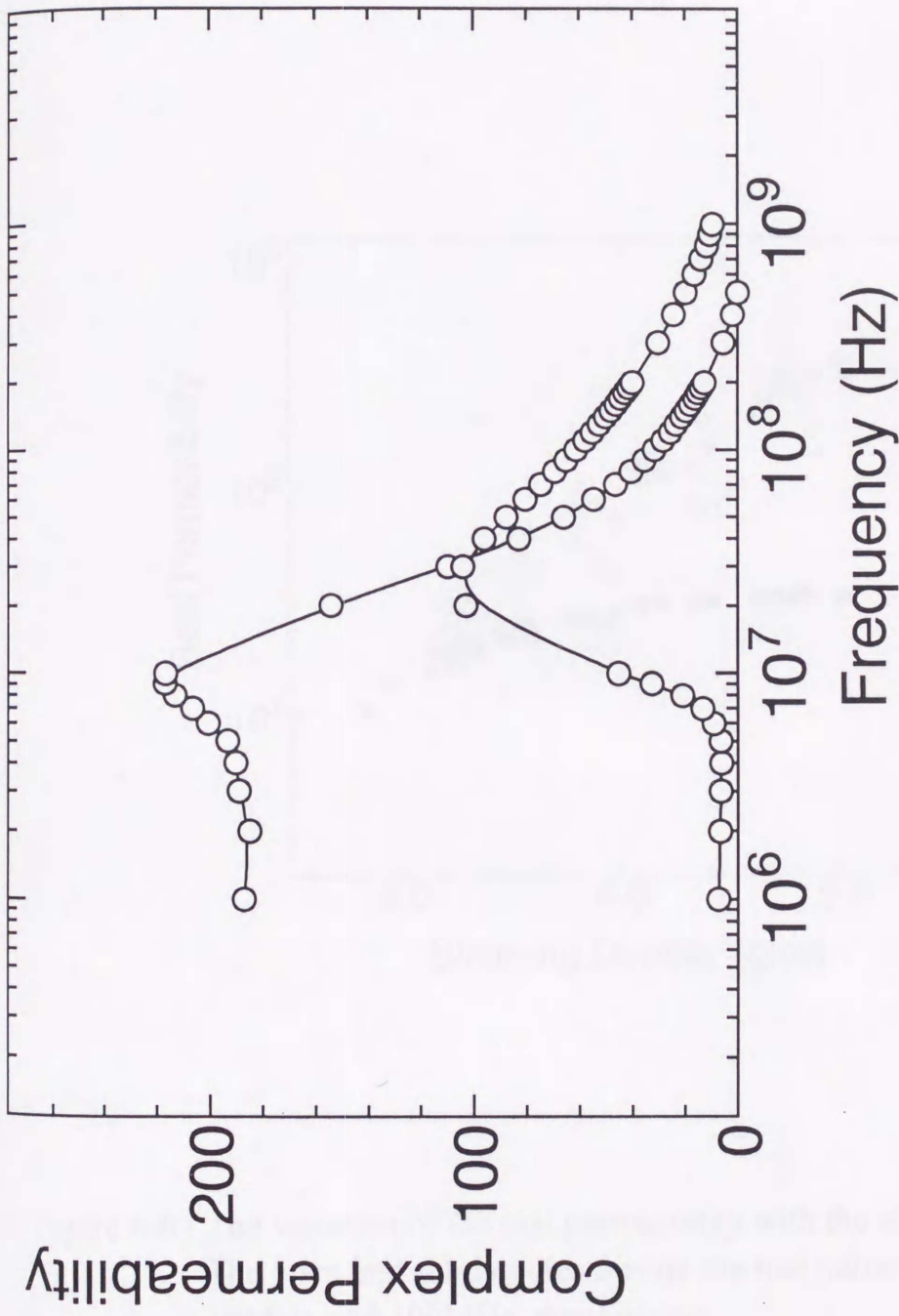


Figure 6-5 : Frequency dispersion of the complex permeability for the sintered ferrite, which was prepared by the optimum conditions.

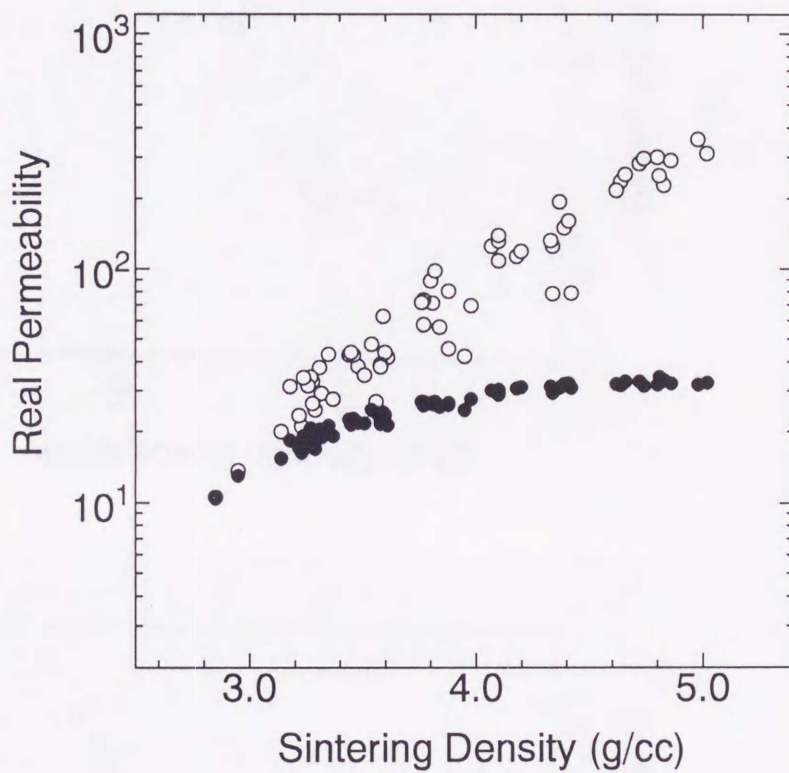
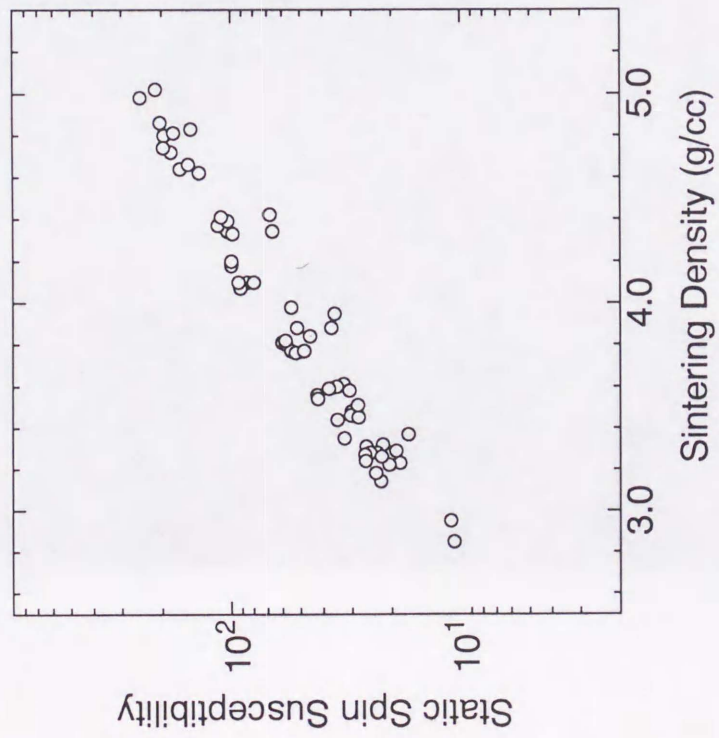
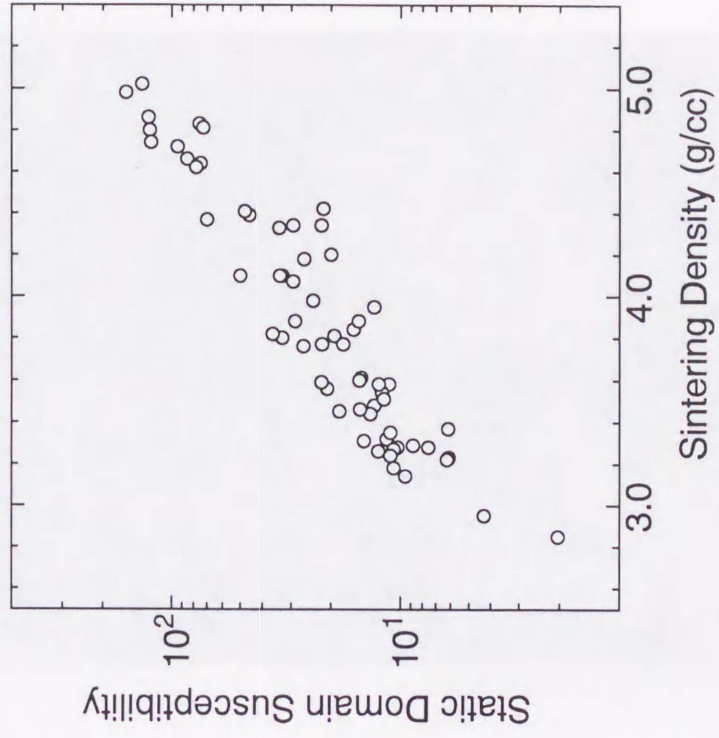


Figure 6-6 : The variation of the real permeability with the sintering density. The open and solid circles denote the real permeability values at 10MHz and 100MHz, respectively.



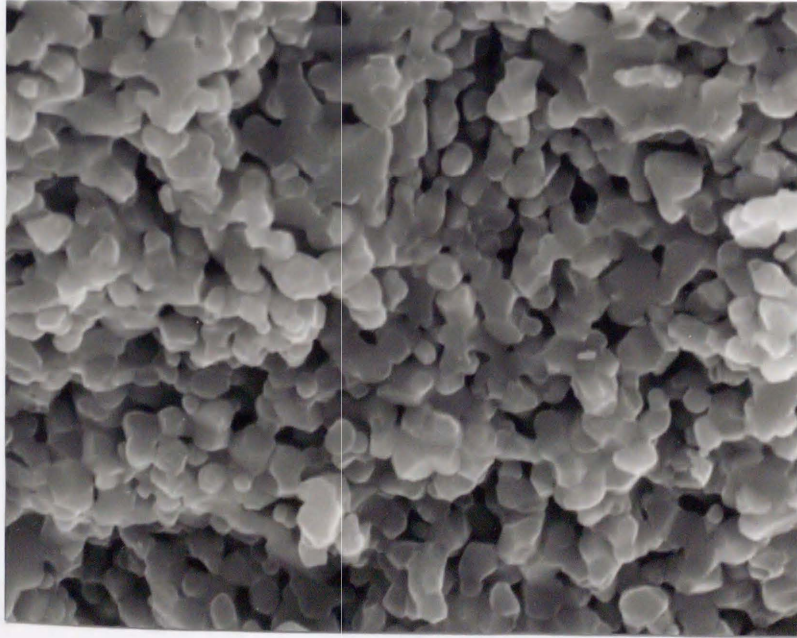
(a)



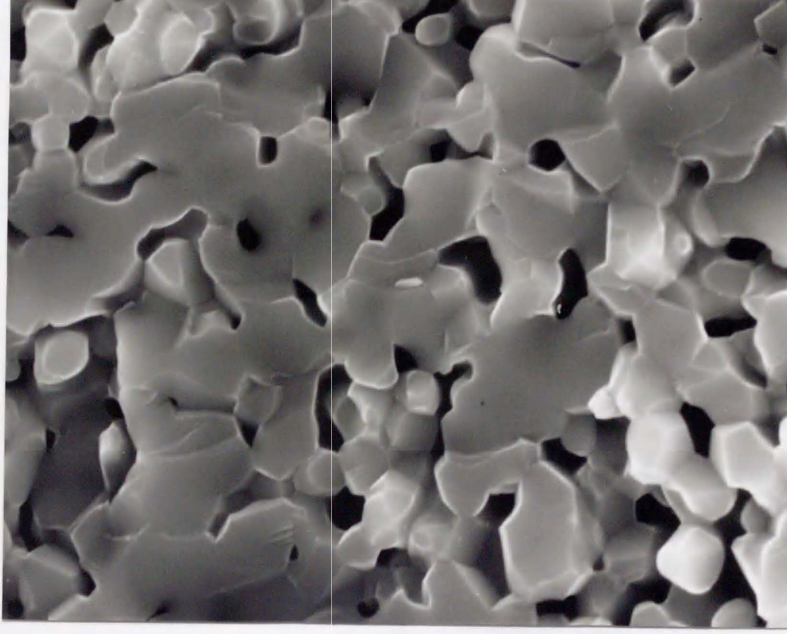
(b)

Figure 6-7 : The variation of the static permeability with the sintering density.

(a) Spin rotational component and (b) Domain wall motion contribution.



(a)



(b)

Figure 6-8 : SEM photographs for the fractured surface of the sintered ferrite.

(a) Sintering density = 4.35g/cc, $\mu(10\text{MHz})=125$ and $\mu(100\text{MHz})=30$,

(b) Sintering density = 4.35g/cc, $\mu(10\text{MHz})=190$ and $\mu(100\text{MHz})=30$.

Table 6-1 : Average particle size (μm) of the starting powders for the preparation of Ni-Zn-Cu ferrite ceramics.

Starting materials	Fe_2O_3	NiO	ZnO	CuO
A	0.15	0.50	0.18	0.40
B	0.15	0.04	0.18	0.40
C	0.15	0.50	0.02	0.40
D	0.03	0.50	0.18	0.40

Chapter 7

Electromagnetic properties and power loss in Mn-Zn ferrite ceramics

Mn-Zn ferrite sintered ceramics have been used widely in high frequency devices such as transformers, magnetic heads, etc. Recently, the driving frequency of switching power supplies has been raised up to the 1MHz range due to the miniaturization of electronic devices. In this frequency range, the power loss increases drastically, mainly due to the eddy current loss[1,2]. This eddy current loss of Mn-Zn ferrite is usually reduced by an increase in the electrical resistance. It is well known that the addition of CaO and SiO₂ is effective in attaining high electrical resistivity[3]. The additives, concentrated at the ferrite grain boundary, lead to the formation of an insulating layer, which results in an enhancement of the electrical resistivity at the grain boundary. Another method of reducing the eddy current loss is the fining of the ferrite grain[4-6]. However, this method causes an increase of the hysteresis loss simultaneously. Thus, there is a trade-off between the lowering of the eddy current loss and that of the hysteresis loss.

In accordance with the above studies, the electromagnetic properties of Mn-Zn ferrite are sensitive to the micro-structure of the sintered ceramics. Here, Mn-Zn ferrite sintered ceramics were prepared by the usual ceramic method, and the relations between the micro-structure and electromagnetic properties have been clarified using the non-magnetic and insulating grain boundary model. The differences originated from the raw

materials have also been mentioned briefly.

Mn-Zn ferrite sintered ceramics were prepared by the usual ceramic method. The starting particles of $\alpha\text{-Fe}_2\text{O}_3$, MnCO_3 and ZnO were mixed together through wet attrition milling, with the cation ratio adjusted to $\text{Mn}_{0.73}\text{Zn}_{0.20}\text{Fe}_{2.07}\text{O}_4$. The mixed powders were then calcined in air at 860°C for six hours and slowly cooled to room temperature. They were re-ground to the particle size less than $80\mu\text{m}$ through wet ball milling. In the milling process, CaO and SiO_2 were introduced as the constitution components of the insulating layer, the total amounts of which were adjusted to 200 and 100ppm, respectively. The obtained powders were then mixed with appropriate amount of poly-vinyl-alcohol (as a binder), and subjected to press compacting (disc with the diameter of 50mm and the thickness of about 5mm). The compacted discs were sintered in static air at 1275°C and 1325°C for six hours and slowly cooled to room temperature in N_2 atmosphere.

Two different methods were used in synthesizing iron oxide ($\alpha\text{-Fe}_2\text{O}_3$) particles. (1) In powder A, $\text{FeCl}_3\text{nH}_2\text{O}$ ($\text{n}=5 \sim 6$) salts were calcined in air at 800°C and then ground through dry vibration milling. (2) In powder B, alkaline $\text{Fe}(\text{OH})_2$ aqueous suspension, prepared from $\text{FeSO}_4\cdot 7\text{H}_2\text{O}$ and NaOH aqueous solutions, was aerial-oxidized to precipitate Fe_3O_4 particles. It was then calcined in air at 800°C and ground through dry vibration milling. The average particle size and the quantities of the impurities are listed in Table 7-1. The average particle size of powder A is slightly smaller than that of powder B. Powder A has a large amount of Cl impurity and powder B has a large amount of Na and SO_4 , which are attributed to the Fe source materials and to the preparation methods as well.

The sintering density was evaluated by measuring the weight and the volume of the sintered discs. The micro-structural observation on the fracture surface of the sintered ferrite ceramics was carried out using the scanning electron microscopy (HITACHI, S-800). The magnetization was determined through the use of the vibrating

sample magnetometer (TOEI KOGYO, VSM-3) for the fragment of the sintered ferrite. The sintered discs were cut into a ring form with the outer diameter of 38mm and the inner diameter of 17mm. They were then subjected to the complex permeability measurement. The magnetic permeability ($\mu = \mu' - j\mu''$) was measured through two different techniques : in the frequency range of 100kHz to 10MHz, a coil was wound around the toroidal sample and the inductance was measured with the impedance analyzer (Hewlett-Packard, HP-4192A). In the frequency range of 1MHz to 1GHz, the input impedance was measured using the coaxial line technique with network analyzer (Hewlett-Packard, HP-8753C). The sintered disc was inserted into parallel plate electrodes, and the AC resistivity was also measured through the use of the impedance analyzer. Furthermore, the core loss of the sintered specimen was measured with the B-H/Z analyzer (Hewlett Packard, HP-E5060A) in the frequency range of 100kHz to 1MHz at the applied magnetic flux density of 50mT.

7.1 Microstructure and electromagnetic properties

The sintering density, the magnetization and the permeability are listed in Table 7-2. From this table, it was found that the sintering density, the magnetization and the permeability all increase when the sintering temperature is raised. It was also found that using the powder B as the raw material leads to a greater sintering density, greater magnetization and greater permeability at the same sintering temperature. These results indicate the advantage of using powder B as the raw material, in that a high sintering density, high magnetization and high permeability can be attained at a relatively low sintering temperature. SEM photographs for the fracture surface of the sintered ferrite are shown in Fig.7-1. The average size of the ferrite grain, geometrically estimated from the SEM photographs of the fracture surface, is also shown in Table 7-2. The grain size also increases with increase of the sintering temperature. The sintered ceramics with large grain size can easily be obtained by using powder B as the raw material than by

using powder A.

AC resistivity was also examined. Figure 7-2 shows the AC resistivity of Mn-Zn ferrite sintered ceramics plotted in the complex plane. The trace of the complex resistivity is represented by a semi-circle, which is known as the Cole-cole circle[7]. It indicates that the AC resistivity ($R(\omega)$) can be described as an equivalent circuit with the grain resistivity (R_G), the grain boundary resistivity (R_{GB}) and the inter-grain capacitance (C_{GB}), as shown in Fig 7-3. The AC resistivity is then written by the following equation,

$$R(\omega) = R_G + (R_{GB}^{-1} - j\omega C_{GB})^{-1}. \quad (7.1)$$

Then,

$$\text{Re} [R(\omega)] = R_G + R_{GB}/[1+(\omega C_{GB}R_{GB})^2] \quad (7.2a)$$

$$\text{Im} [R(\omega)] = \omega C_{GB}R_{GB}/[1+(\omega C_{GB}R_{GB})^2]. \quad (7.2b)$$

According to this equivalent circuit calculation, the intercept of low frequency limit is equal to the summation of the grain resistivity and the grain boundary resistivity, and that of high-frequency limit provides only the grain resistivity. Therefore, these resistivities can be obtained from the Cole-cole circle. The obtained values of the resistivities are listed in Table 7-3. The grain resistivity is three-order of magnitude smaller than the grain boundary resistivity. High-conductive grain is produced by the presence of Fe^{2+} , which leads to the hopping conduction in the octahedral Fe sites. Since it is suspected that the determination of the grain resistivity contains large numerical errors, only grain boundary resistivity, due to the formation of CaO-SiO₂ insulating layer, is taken into consideration. From the results, the grain boundary resistivity decreases with increase of the sintering temperature. In addition, the sintered ceramics using powder A as the raw material have higher grain boundary resistivity than those using powder B.

Here, the relations between the micro-structural properties and the electromagnetic properties in Mn-Zn ferrite sintered ceramics have been clarified using the non-magnetic and insulating grain boundary model, which is proposed in chapter 5.

We assume that, in the polycrystalline Mn-Zn ferrite ceramics, magnetic and conductive ferrite grains are surrounded by non-magnetic and insulating inter-grain layer, and that the inter-grain layer contains both the impurities such as CaO and SiO₂ concentrated at the ferrite grain boundary and the inter-granular pores playing as air gap. Since, in general, the ferrite grain size and the grain boundary layer thickness have certain distributions, their average values (D and δ) are utilized. According to this model, the sintering density of the ferrite ceramics is given by the following equation,

$$\rho = \rho_f V + \rho_g (1 - V) \text{ and } V = D^3 / (D + \delta)^3 \quad (7.3)$$

where ρ_f and $\rho_g (< \rho_f)$ are the density of the ferrite grain and that of the grain boundary layer, respectively, and V is the volume fraction of the ferrite phase. From this equation, it is found that the ferrite volume loading increases with the sintering density. This equation can be re-written as,

$$\rho = \rho_g + (\rho_f - \rho_g) / [1 + (\delta/D)]^3 \quad (7.4)$$

Therefore, increase of the sintering density leads to a decrease of (δ/D) . At the same thickness of the grain boundary layer, the sintered ceramics with larger ferrite grain provide smaller (δ/D) value and larger sintering density.

The magnetization, B (gauss), in the sintered ceramics is proportional to the specific magnetization, M_s (emu/g), of the magnetic ferrite phase and to the volume fraction of magnetic ferrite phase, V . Assuming the specific magnetization of the ferrite phase to be constant, the magnetization increases linearly with the volume loading of the ferrite. In other words, the magnetization increases linearly with the sintering density. Figure 7-4 shows the magnetization variation with the sintering density. It implies that the linearity between the sintering density and the magnetization is well satisfied, and that M_s has little dependence on the sintering conditions and the spinel ferrite formation is completed at temperature of about 1275°C.

The permeability μ of the polycrystalline ceramics can be described with the use of the magnetic circuit model,

$$\mu = \mu_{\text{int}} [1 + (\delta/D)] / [1 + \mu_{\text{int}}(\delta/D)] \quad (7. 5)$$

where μ_{int} corresponds to the intrinsic permeability of the ferrite grain. Increase of the sintering density leads to a decrease of (δ/D) and it results in an enhancement of the permeability. The permeability at 100kHz versus the sintering density of ferrite grain is plotted in Fig.7-5. The variation of the permeability can also be explained qualitatively using this model.

The variation of the grain boundary resistivity with the sintering density is shown in Fig.7-6. The grain boundary resistivity is reduced when the sintering density increases. This behavior can also be described as follows. The effective resistivity (R_{eff}) can be summarized through the equation

$$R_{\text{eff}}(D+\delta) = R_f D + R_g \delta \quad (7. 6)$$

where R_f denotes the specific resistivity of the ferrite grain and R_g the specific resistivity of the insulating layer. The thickness of the insulating layer is sufficiently thin to be neglected ($\delta \ll D$). Therefore, equation (7. 6) can be re-written as

$$R_{\text{eff}} = R_f + R_g(\delta/D) . \quad (7. 7)$$

We have measured the second term as the grain boundary resistivity. Therefore, the grain boundary resistivity decreases as the sintering density increases. This also coincides qualitatively with the experimental results as well as the magnetic properties such as magnetization and permeability.

From the above considerations, several features can be seen. Both magnetization and permeability increase with increase of the sintering density and with decrease of the (δ/D) value, since both of them are enhanced by the magnetic connection between the ferrite grains. Additionally, electrical resistivity decreases with increase of the sintering density and with decrease of the (δ/D) value, since the electrical conduction is enhanced by the electrical percolation and by the inter-grain connection. Lowering of (δ/D) is required for the sintered ferrite with high magnetization and high permeability. However, the lowering of (δ/D) causes a decrease in the electrical resistivity. For

practical purposes, the sintered ceramics with high magnetization, high permeability and high resistivity are required. Thus, there exists a trade-off between the increase of the magnetization and permeability and the increase of the electrical resistivity. The increase of the resistivity without reduction of the magnetization and permeability is a serious problem for practical high-frequency devices. One of the solution is to increase the specific resistivity of the grain boundary. Since this can reduce the insulating layer thickness, high resistivity can be attained simultaneously with high magnetization and high permeability. We are now studying other insulating elements from this point of view.

7.2 Power loss

The core loss measurement of each sintered specimen was carried out. Figure 7-7 shows typical variation of the core loss with frequency. The core loss abruptly increases with the frequency. The core loss mainly consists of the hysteresis loss and the eddy current loss, and it is well known that the hysteresis loss (L_{hys}) increases linearly with increase in the frequency, and that the eddy current loss (L_{edd}) is proportional to the square of the frequency. Considering their frequency dependence, the loss (L_{total}) is numerically decomposed into these two components ;

$$L_{\text{total}} = L_{\text{hys}} + L_{\text{edd}} = \alpha_{\text{hys}}\omega + \alpha_{\text{edd}}\omega^2. \quad (7.8)$$

The obtained parameters, α_{hys} and α_{edd} , for each sintered specimen are also listed in Table 7-3. As the sintering temperature is raised, the α_{hys} value decreases and the α_{edd} value increases : the hysteresis loss is reduced and the eddy current loss is enhanced.

At the same sintering temperature, the sintered ceramics using powder A as the raw material have larger α_{hys} value and lower α_{edd} value than those using powder B.

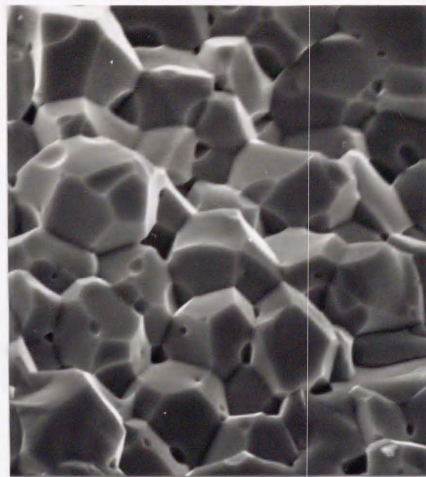
The behavior of the core loss, which is separated into the hysteresis and eddy current losses, is considered. The hysteresis loss is proportional to the area of the minor loop, and the minor loop area increases with the coercivity. Since the coercivity is an index for the magnetic hardness, it has the inverse dimension of the permeability. That is,

the hysteresis loss is inversely proportional to the permeability. Figure 7-8 shows the variation of the hysteresis loss coefficient, α_{hys} , with the permeability. The α_{hys} value increases with decrease of the permeability, and it qualitatively coincides with the above consideration. As for the eddy current loss, the eddy current loss coefficient, α_{edd} , increases with decrease of the grain boundary resistivity, which is shown in Fig. 7-9. From these analyses, the reduction of the hysteresis loss requires the enhancement of the permeability, and the lowering of the eddy current loss needs the enhancement of the grain boundary resistivity. Therefore, the trade-off relation between high permeability and high resistivity is reflected to the other trade-off relation between the lowering in hysteresis loss and the lowering in eddy current loss. The magnetic connection yields low coercivity and small hysteresis loss. But the connection between the ferrite grains increases the electrical conduction, resulting in large eddy current loss.

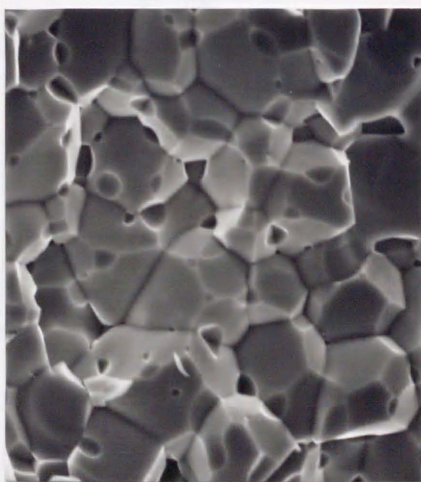
Finally, the differences in the electromagnetic properties of the sintered ceramics are attributed to the structural factors such as the sintering density and the average size of the ferrite grain. These structural variations can be originated from the sintering ability and the grain growth ability of raw materials. Additionally, there are advantages in using powder B as the raw material, since high sintering density, high magnetization and high permeability can be attained at lower sintering temperature.



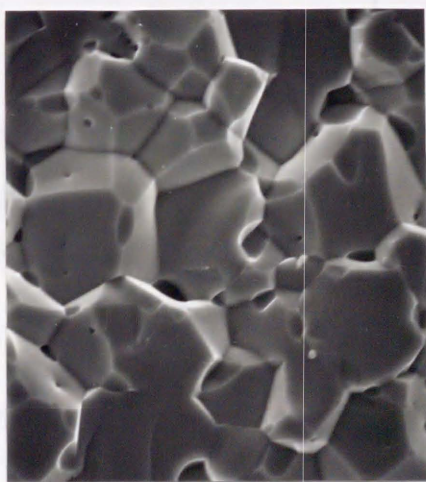
(a)



(b)



(c)



(d)

Figure 7-1 : SEM photographs of the fracture surface of the sintered ferrite.

- (a) sintered at 1275°C using powder A,
- (b) sintered at 1325°C using powder B,
- (c) sintered at 1275°C using powder A,
- (d) sintered at 1325°C using powder B.

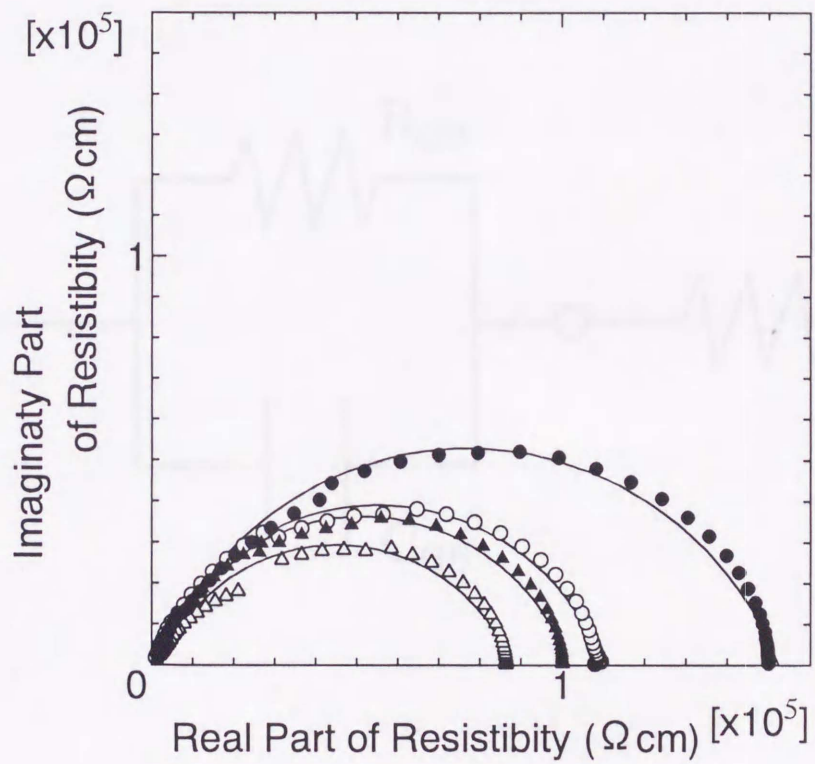


Figure 7-2 : Cole-cole plot for the complex resistivity in the ferrite ceramics.

- : sintered at 1275°C using powder A,
- : sintered at 1275°C using powder B,
- ▲ : sintered at 1325°C using powder A,
- △ : sintered at 1325°C using powder B.

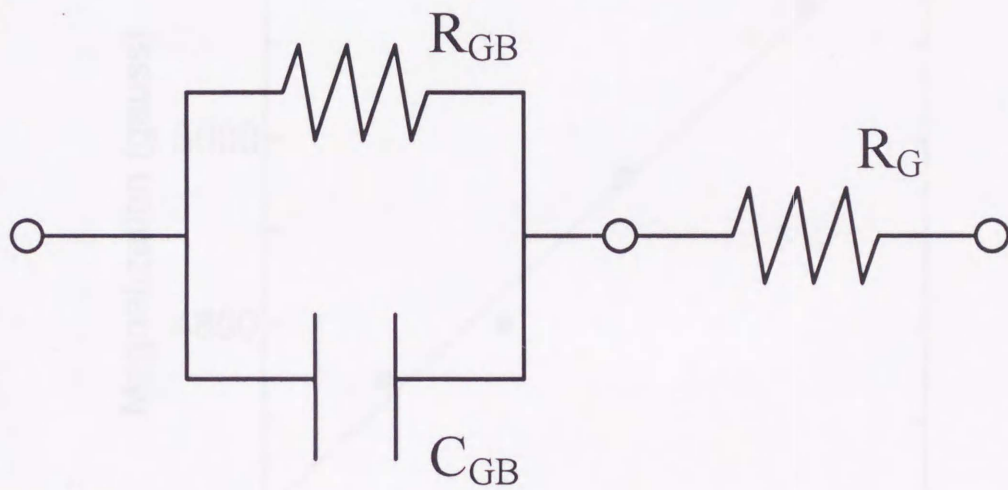


Figure 7-3 : Equivalent circuit for complex resistivity in the sintered ferrite ceramics.

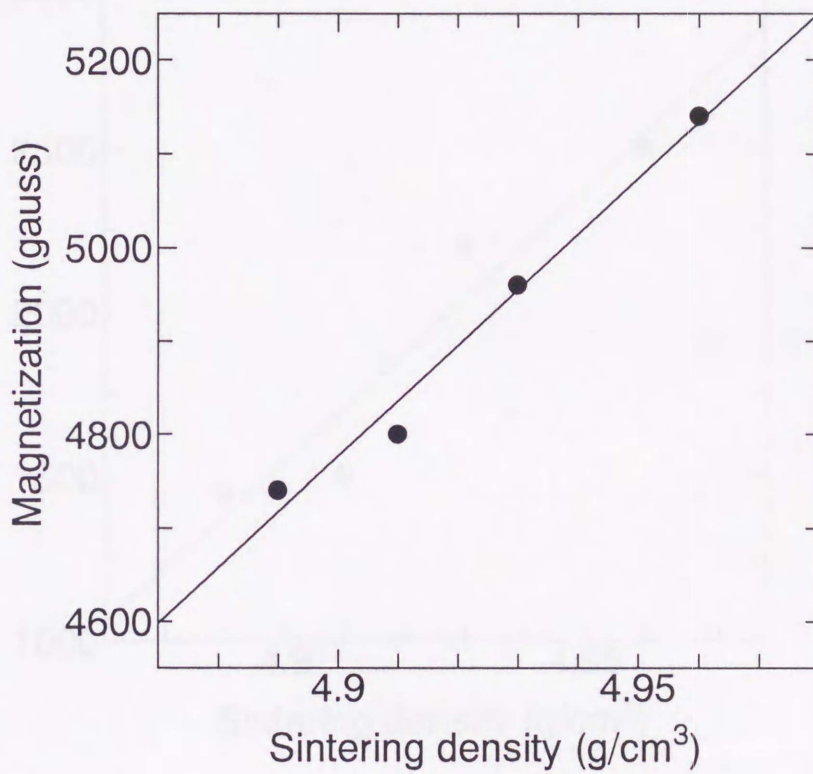


Figure 7-4 : Magnetization variation with the sintering density. The solid line is drawn as a guide for the eyes.

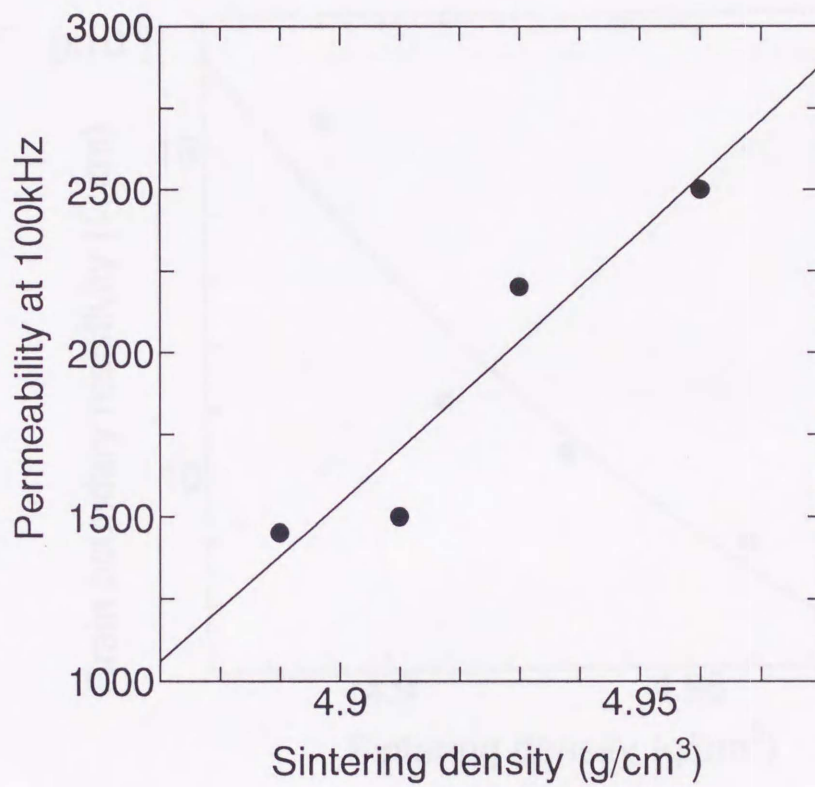


Figure 7-5 : Variation of the permeability at 100kHz with the sintering density. The solid line is drawn as a guide for the eyes.

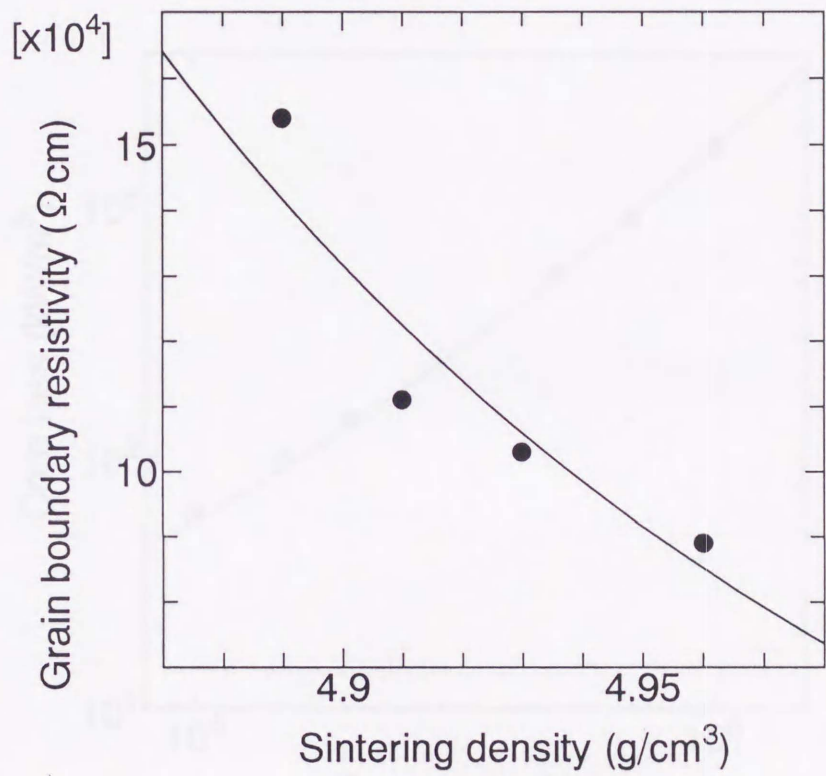


Figure 7-6 : Grain boundary resistivity versus sintering density. The solid line is drawn as a guide for the eyes.

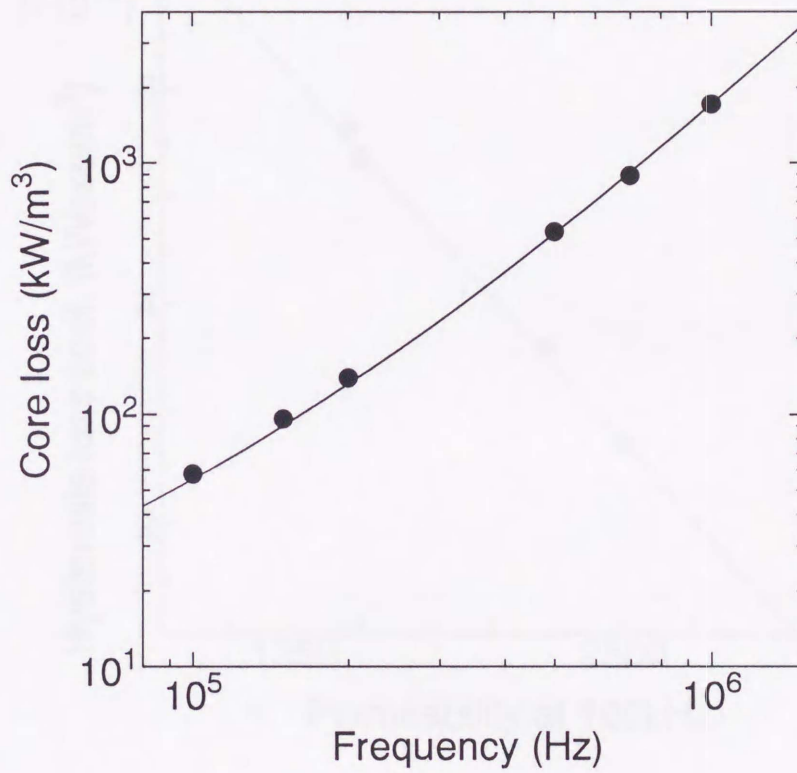


Figure 7-7 : Frequency dependence of the core loss at $B_m=50\text{mT}$ for the specimen sintered at 1325°C using powder B. The solid line is drawn as a guide for the eyes.

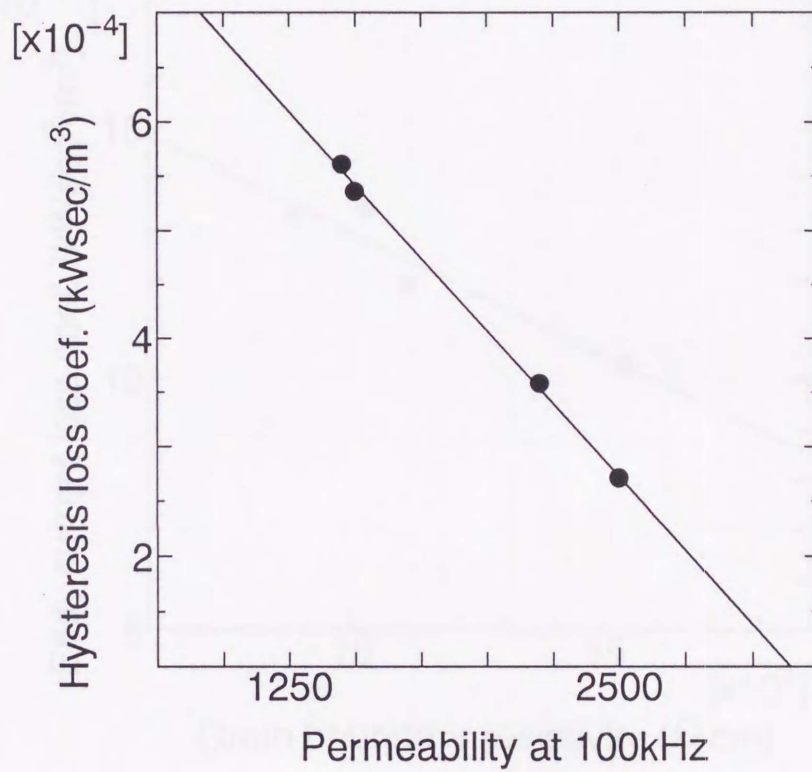


Figure 7-8 : The hysteresis loss coefficient, α_{hys} , versus the permeability at 100kHz. The solid line is drawn as a guide for the eyes.

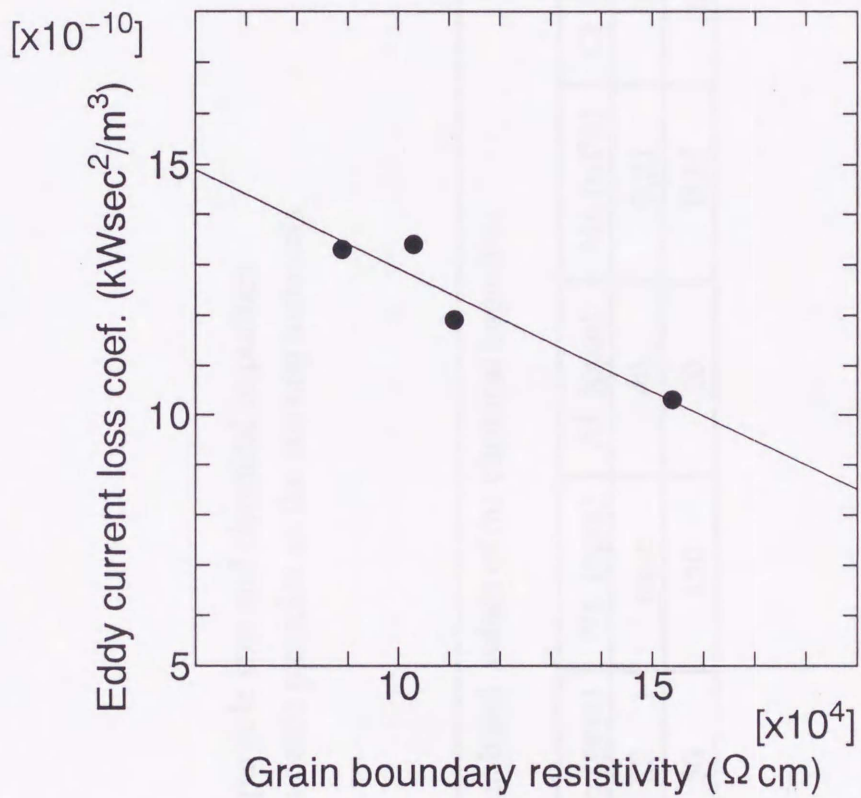


Figure 7-9 : The eddy current loss coefficient, α_{edd} , versus the grain boundary resistivity. The solid line is drawn as a guide for the eyes.

Table 7-1 : Average particle size and chemical impurities in iron oxide particles as the starting materials

	Average particle size (μm)	Analyzed values of the chemical impurities						
		Ca (ppm)	SiO ₂ (ppm)	Na (ppm)	Al (ppm)	Mn (wt%)	Cl (wt%)	SO ₄ (wt%)
Powder A	0.19	68	82	trace	40	0.21	0.11	0.09
Powder B	0.25	27	50	150	10	0.15	trace	0.34

Table 7-2 : Structural and magnetic properties in the ferrite sintered ceramics

Raw material	Sintering temperature (°C)	Sintering density (g/cm ³)	Average grain size (µm)	Magnetization (gauss)	Permeability at 100kHz
Powder A	1275	4.89	10	4740	1450
Powder A	1325	4.93	14	4960	2200
Powder B	1275	4.91	12	4800	1500
Powder B	1325	4.96	18	5140	2500

Table 7-3 : Grain and grain boundary resistivities and the hysteresis and eddy current loss coefficients in the ferrite sintered ceramics.

Raw materials	Sintering temperature (°C)	Grain resistivity (Ω cm)	Grain boundary resistivity (Ω cm)	$\alpha_{hvs} \times 10^{-4} (\text{kWsec}/\text{m}^3)$	$\alpha_{edd} \times 10^{-9} (\text{kWsec}^2/\text{m}^3)$
Powder A	1275	1680	1.54×10^5	5.61	1.03
Powder A	1325	1130	1.03×10^5	3.58	1.34
Powder B	1275	330	1.11×10^5	5.36	1.19
Powder B	1325	2280	0.89×10^5	2.71	1.33

Chapter 8

Concluding remarks

The main result in this thesis is the introduction of the magnetic circuit model for the complex permeability spectra in the ferrite composite materials. For the original sintered ferrite, we have applied the inverse cole-cole plot technique to separate the permeability spectra into two contributions : spin rotational susceptibility and domain wall motion susceptibility. The numerical calculation provides the dispersion parameters of these two susceptibilities. The dispersion parameters are transformed using the gap parameter, which is a simple index for the structure of the composite materials. Using new parameters, we can estimate the complex permeability spectra for the ferrite composite materials. In addition, we obtain the extended Snoek's law for the composite materials using this model calculation.

The magnetic circuit model provides the changes in the magnetic connection with the ferrite loading. The introduction of the magnetic inert component causes not only the magnetic dilution but also a cut-off of the magnetic circuit in the materials. Thus, the permeability becomes lower than that expected from the semi-empirical logarithmic law. The feature is attributed to the demagnetizing field generated by the magnetic poles on the interface of the ferrite particle. Simultaneously, the addition of the demagnetizing field on the magnetocrystalline anisotropy field leads to a shift of the resonance frequency toward higher frequency. The demagnetizing effect on Snoek's law is also included in the magnetic circuit model calculation.

Furthermore, this magnetic circuit model can qualitatively be applied to the

sintered ferrite ceramics, which have non-coherent structure. In addition, it is found that the electromagnetic properties of the grain boundary play an important role in the ferrite ceramics. This model calculation is thought to be a useful tool for the development in many high-frequency electromagnetic devices through the evaluation of the complex permeability in the materials.

References

Chapter 1

- [1] J.J. Snoek : Physica XIV **4**(1948) 207.
- [2] D. Polder and J. Smit : Rev. Mod. Phys. **25**(1953) 89.
- [3] G. Rado : Rev. Mod. Phys. **25**(1953) 81.
- [4] A.Globus : J. Phys. Suppl. **C1**(Proceedings of 3rd International Conference on Ferrite) (1977)1.
- [5] J.P. Bouchaud and G.P. Zerah : J. Appl. Phys. **67**(1989) 5512.
- [6] J.B. Birks : Proc. Phys. Soc. **LX3**(1947) 282.
- [7] C.A. Grimes and D.M. Grimes : Phys. Rev. B **43**(1991) 10780.
- [8] C.A. Grimes and D.M. Grimes : J. Appl. Phys. **69**(1991) 6186.
- [9] C.A. Grimes : IEEE Trans. Magn. **27**(1991) 4310.
- [10] W.T. Doyle and I.S. Jacobs : Phys. Rev. B **42**(1990) 9391.
- [11] W.T. Doyle and I.S. Jacobs : J. Appl. Phys. **71**(1992) 3296.
- [12] M.T. Johnson and E.C. Visser : IEEE Trans. Magn. **26**(1990) 1987.

Chapter 2

- [1] J. Smit and H.P.J. Wijn : Ferrites, Eindhoven (1959) 137.
- [2] J.B. Goodenough : Phys. Rev. **100**(1955) 564.
- [3] J.B. Goodenough : J. Phys. Chem. Solids **6**(1958) 287.
- [4] J. Kanamori : J. Phys. Chem. Solids **10**(1958) 87.
- [5] L. Neel : Ann. Physiq. **12**(1948) 137.
- [6] L. Neel : Proc. Phys. Soc. (London) **65A**(1952) 869.
- [7] Y. Yafet and C. Kittel : Phys. Rev. **87**(1952) 290.
- [8] D. Fiorani, S. Viticoli, J.L. Dormann, J.L. Tholence and A.P. Murani : Phys. Rev.

B30(1987) 2776.

- [9] J.L. Dormann and M. Nogues : J. Phys. Condens. Matter **2**(1990) 1223.
- [10] Z. Liu, G. Chen, W. Zhou and S. Lin : J. Magn. Magn. Mat. **137**(1994) 51.
- [11] K. Yoshida and M. Tachiki : Prog. Theor. Phys. **17**(1957) 331.
- [12] H.A. Jahn and E. Teller : Proc. Roy. Soc. (London) **A161**(1937) 220.
- [13] T. Nakamura and H. Sadamura : Phys. Stat. Solidi (投稿中).

Chapter 3

- [1] F.R. Sale : Metall. Mater. Technol. **9**(1977) 439.
- [2] D.J. Anderton and F.R. Sale : Powder. Metall. **22**(1979) 8.
- [3] J.M. Fletcher and C.J. Hardy : Chem. Ind. **87**(1968) 48.
- [4] C. Marcilly, P. Courty and B. Delmon : J. Amer. Ceram. Soc. **53**(1970) 56.
- [5] C.M. Flynn : Chem. Rev. **84**(1984) 31.
- [6] M. Kiyama and T. Takada : Bull. Chem. Soc. Japan **46**(1973) 1680.
- [7] T. Nakamura and H. Kurokawa : J. Mater. Sci. **30**(1995) 4710.

Chapter 4

- [1] L. Landau and E. Lifshitz : Phys. Z. Sowjetunion **8**(1935) 153.
- [2] E. Lifshitz : J. Phys. USSR **8**(1944) 337.
- [3] T.L. Gilbert : Phys. Rev. **100**(1955) 1243.
- [4] Y.Naito : Proceedings of 1st International Conference on Ferrite (1970)558.

Chapter 5

- [1] A.Globus : J. Phys. Suppl. **C1**(Proceedings of 3rd International Conference on Ferrite) (1977)1.
- [2] J.J. Snoek : Physica XIV **4**(1948) 207.
- [3] W.T. Doyle and I.S. Jacobs : Phys. Rev. B **42**(1990) 9391.

- [4] W.T. Doyle and I.S. Jacobs : J. Appl. Phys. **71**(1992) 3296.

Chapter 6

- [1] T.Nomura and M.Takaya : HYBRIDS **3**(1987) 15.
[2] Y.Naito : Proceedings of 1st International Conference on Ferrite (1970)558.
[3] A.Globus : J. Phys. Suppl. **C1**(Proceedings of 3rd International Conference on Ferrite) (1977)1.

Chapter 7

- [1] J. Smit and H.P.J. Wijn : Ferrites, Eindhoven (1959) 134.
[2] T. Sato and Y. Sakaki : IEEE Trans. Magn. **26**(1990) 2894.
[3] T. Akashi : Trans. Japan Inst. Metals **2**(1961) 171.
[4] T .Akashi, I. Sugano, T. Okuda and T. Tsuji : Proceedings of 1st International Conference on Ferrite (1970) 96.
[5] T. Sano, A. Morita and A. Matsukawa : Proceedings 5th International Conference on Ferrite (1989) 595.
[6] R. Lebourgeois, C. Deljurie and J.P. Ganne : Proceedings of 6th International Conference on Ferrite (1992) 1169.
[7] C.G. Koops : Phys. Rev. **83**(1951) 121.